

The Preserve: Lehigh Library Digital Collections

A Study of Phase Transitions in Globular Protein Solutions using Monte Carlo Simulation

Citation

Li, Xiaofei. *A Study of Phase Transitions in Globular Protein Solutions Using Monte Carlo Simulation*. 2009, https://preserve.lehigh.edu/lehigh-scholarship/graduate-publications-theses-dissertations/theses-dissertations/study-phase.

Find more at https://preserve.lehigh.edu/

This document is brought to you for free and open access by Lehigh Preserve. It has been accepted for inclusion by an authorized administrator of Lehigh Preserve. For more information, please contact preserve@lehigh.edu.

A Study of Phase Transitions in Globular Protein Solutions Using Monte Carlo Simulation

by

Xiaofei Li

Presented to the Graduate Research Committee

of Lehigh University

in Candidacy for the Degree of

Doctor of Philosophy

in

Physics

June 2009

Copyright © 2009 Xiaofei Li
All rights reserved

Approved and recommended for acceptance as a dissertation in partial fulfillment of the requirements for the degree of Doctor of Philosophy.

_____

Date

James D. Gunton

Dissertation Director

_____

Accepted Date

Committee Members

_____

James D. Gunton

_____

Jeffery M. Rickman

_____

Dimitrios Vavylonis

_____

Manoj K. Chaudhury

Acknowledgments

Most importantly I want to thank my advisor, Professor James D. Gunton for his guidance during my study at Lehigh University. His perpetual energy and enthusiasm in research has motivated all his advisees, including me. I would never be able to finish this work if it were not for his encouragement and inspiration. Besides research, he is always accessible and willing to help with other aspects of life. I am blessed to have him as my advisor and mentor.

I want to thank all my committee members, Professor Jeffery M. Rickman, Professor Dimitrios Vavylonis, Professor Manoj K. Chaudhury for all their helpful advice and suggestions. I also want to thank Professor Garold Borse for his continuous support although he resigned from my committee when he retired from Lehigh.

I want to thank all professors that have taught me during my stay at Lehigh. Not only have I learned a great amount of physics from you, I also enjoyed all your witty stories in class.

Steven Lettieri and Nathaniel Wentzel have been wonderful colleagues and friends during the past few years. I have benefited significantly from their helpful ideas. I could not imagine what work would have been without them. I also want to thank Daniel L. Pagan and Andrey Shiryayev for always responding to my questions via email, although I didn't have the chance of collaborating directly with them.

I am especially thankful to my parents for their continuous love and support. I hope with this thesis I won't disappoint my younger brother since he always looks up to me; I know he is going to become successful in whatever field he chooses. I also want to thank my boyfriend for his love and bearing with me for the past five years.

Finally I want to dedicate this thesis in memory of my grandmother for her perpetual love and caring for me. She would be so proud of me for everything I have accomplished today. She will be forever in my memory.

Contents

Abstract **1**

1 Introduction **3**

2 Simulation Methods **13**

2.1 Introduction to Importance Sampling 13

2.2 Monte Carlo Simulation in Various Ensembles 15

2.2.1 Isobaric-Isothermal Monte Carlo 15

2.2.2 Grand Canonical Monte Carlo 17

2.2.3 Gibbs Ensemble Monte Carlo 19

2.3 Quaternions and Their Use in Orientational Moves 20

3 Introduction to Hofmeister Series and Hydrophobic Surface Forces **24**

3.1 Hofmeister Series 24

3.2 Hydrophobic Surface Forces 27

3.2.1 Ion Adsorption at Liquid Interfaces 27

3.2.2 Effects of Ion Adsorption on Protein Aggregation 38

4 Ion-Dispersion Effect and the Phase Diagram of Aqueous Lysozyme Solution with NaSCN Electrolyte 41

4.1 Introduction 41

4.2 Model 44

4.3 Simulation Techniques 46

4.3.1 Fluid-Fluid Coexistence 46

4.3.2 Fluid-Solid Coexistence 47

4.4 Results 52

4.5 Conclusion 55

5 Ion-Specific Effects on Phase Transitions in Protein Electrolytes due to Hydrophobic Surface Forces 57

5.1 Introduction 57

5.2 Model and Methods 58

5.2.1 Model 58

5.2.2 Methods 60

5.3 Results 64

5.4 Conclusion 73

6 Phase Diagram of a Model of Nanoparticles in Electrolyte Solutions Includ-

ing Ion Dispersion Effects **75**

6.1 Introduction 75

6.2 Model and Simulation Techniques 78

6.2.1 Model 78

6.2.2 Simulation Techniques 80

6.3 Results 87

6.4 Conclusion 90

7 A Simple Model of Directional Interactions for Proteins **99**

7.1 Introduction 99

7.2 Two-Patch Model 103

7.2.1 Crystal Structures 105

7.3 Simulation techniques 108

7.3.1 Equation of State 108

7.3.2 Free Energy Calculations 108

7.4 Results 112

7.5 Conclusion 116

8 Conclusion **130**

Vita **151**

List of Tables

4.1 Best fit parameters for isotherms at $\frac{T}{T_0} = 3.5$. 49

4.2 Critical parameters for the fluid-fluid coexistence curve. 53

5.1 Parameters of interest at T_c. 73

6.1 Summary of the infinite system critical parameters for lysozyme solutions with 0.1M NaI electrolyte. 87

6.2 Coexistence parameters in the subcritical region from the multicanonical histogram reweighting method. 89

6.3 Coexistence densities in the subcritical region from the Gibbs Ensemble Monte Carlo (GEMC) method. 90

7.1 The density range and ground state energy for different crystal structures. "n.n." means only nearest-neighbor interactions exist between particles, while "n.n.n" means next-nearest-neighbor interactions exist as well. 118

7.2 Free energy of the solid phases, as obtained by thermodynamic integration from the Einstein crystal. 119

7.3 Coexistence points obtained using the thermodynamic integration method. The points marked with a † or a § are in the region where fcc-o and bcc-o coexistence exhibits a domelike shape, i.e. a reentrant behavior. † for the left branch, § for the right branch. 120

7.4 Some of the coexistence points obtained from the Gibbs-Duhem integration. See Table 7.3 for the meanings of the symbols in front. 121

List of Figures

1.1 (a) Upper: normal red blood cells maintain their shape as they pass through the capillaries and release oxygen to the peripheral tissues. Lower: Sickle Hemoglobin molecules form bundles when releasing oxygen and deform into an abnormal shape, thus block the flow of cells and interrupt the delivery of oxygen. (b) Schematic of polymers of deoxygenated sickle hemoglobin molecules. Each hemoglobin molecule is represented as a sphere. The spheres twist in an alpha helical bundle made of 14 sickle hemoglobin chains. 4

1.2 An example of crystallized proteins (Green pH7 Bovine γ_{BC} and red γ_{BC} minus Y). 6

1.3 (A) Typical phase diagram for proteins with a relatively long-ranged attractive interaction. (B) Typical phase diagram for proteins with a relatively short-ranged attractive interaction. The potentials are given in inset graphs, respectively. (Reproduced from Ref. [109]) 8

1.4 Contour plots of the free-energy landscape along the path from the metastable fluid to the critical crystal nucleus for a short-ranged Lennard-Jones potential. N_{rho} and N_{crys} are the total number of connected particles and that of solidlike particles in the nucleus. (A) The free-energy landscape well below the critical temperature (T/T_c=0.89). (B) As (A), but for T = T_c. (Reproduced from Ref. [109]) 10

1.5 Variation of the free-energy barrier for homogeneous crystal nucleation, as a function of T/T_c, in the vicinity of the critical temperature. The solid curve is a guide to the eye. (Reproduced from Ref. [109]) 11

2.1 Illustration of constant-NPT ensemble. The pistol in the middle is free to move. 16

2.2 Illustration of Gibbs ensemble. Preserved quantities include: temperature T, the total number of particles $N_1 + N_2$, the total volume $V_1 + V_2$. 19

3.1 Typical ordering of anions in Hofmeister series and some relevant properties. Adapted from: http://tinyurl.com/ed5gj. 25

3.2 Computed free energy profiles for ions binding to the liquid/vapor interface of water at 300 K using polarizable potential models (Reproduced from Ref. [22]). 30

3.3 Snapshots (left-top view, middle-side view) of the solution/air interfaces of 1.2 M aqueous sodium halides from the molecular dynamics simulations; density profiles (right, number densities) of water oxygen atoms and ions plotted vs distance from the center of the slabs in the direction normal to the interface, normalized by the bulk water density (Reproduced from Ref. [54]). 33

3.4 Three models for macromolecules with hydrophobic (purple/dark grey) and cationic surface groups (green/light grey). Left: a non-polar sphere with positively charged patches. Middle: the lysozyme in atomistic detail. Right: the lysozyme coarse grained to the amino acid level. (Reproduced from Ref. [69]) 34

3.5 Simulated potential of mean force, w(r), for fluoride and iodide with a non-polar, nanosized sphere (Reproduced from Ref. [69]). 35

3.6 Relative cumulative sums, N(r), of fluoride and iodide for charged and non-polar patches in lysozyme, simulated in atomistic detail at pH 4.5, 150 mM salt (Reproduced from Ref. [69]). 36

3.7 Potential of mean force w(R) between two lysozyme molecules in various solutions (0.1M) of sodium chloride and sodium iodide, respectively. R is the protein mass-center separation (Reproduced from Ref. [70]). 39

3.8 Cylindrical average of the anion concentration along the axis z connecting the two (fixed) mass centers of the rotating proteins at a 35 $\mathring{A}$ separation. The cylinder radius is 16 $\mathring{A}$ approximately the size of lysozyme and the salt concentration is 0.1 M. (Reproduced from Ref. [70]). 40

4.1 Total lysozyme potential with the 0.2 M NaSCN electrolyte. 46

4.2 Liquid and solid isotherms at $T/T_0 = 3.5$. '+' are the Monte Carlo simulation results and the dotted curves are the fits to the data. 48

4.3 Monte Carlo data of the mean squared displacements for the coupled solid (dots) compared with that of an Einstein lattice(solid line). To achieve deviations of less than 1% with the Einstein lattice, a λ_{max} of 30,000 was required. 51

4.4 $\beta P - \beta\mu$ plot at $\frac{T}{T_0} = 3.5$. Dashed line for liquid; solid line for solid. . 52

4.5 Phase diagram curve obtained from (a) Monte Carlo simulations (b)first-order perturbation theory. The metastability gaps $(T_L - T_c)/T_c$ are approximately 12% and 5%, respectively. 54

5.1 Total potentials for the (a) 0.3M NaCl (b) 0.2M NaI electrolyte systems. Solid line is the fitted polynomial and dots are data obtained from MC simulations. 61

5.2 FSS results for (a) $T_c(L)$ and (b) $\mu_c(L)$ as a function of $L^{-(\theta+1)/\nu}$ for the 0.3M NaCl electrolyte solution. ν is the critical exponent for the correlation length and θ is the universal correction to scaling exponent. For the 3D Ising universality class, $\nu = 0.629$ and $\beta = 0.326$. By extrapolating to infinite volume ($L \to \infty$), we can obtain an estimate of the true bulk behavior: $T_c(\infty) \simeq 0.755T_0$. For more details of FSS, see Ref. [65] 65

5.3 Phase diagram curve obtained from Monte Carlo simulations for the aqueous lysozyme solution with NaCl electrolyte at 0.3 M. The fluid-fluid separation curve is metstable. Open circles are the liquid-solid coexistence data and solid diamonds are the fluid-fluid coexistence data. The solid star is our estimate of the critical point for the infinite system as determined from finite size scaling. 66

5.4 Phase diagram curve obtained from Monte Carlo simulations for the aqueous lysozyme solution with NaI electrolyte at 0.2M. The fluid-fluid separation curve is stable. Solid circles are simulation data and star is our estimate of the critical point as determined by a rectilinear diameter fit. Note that the data for liquid line overlaps the data from the dense fluid phase. 67

5.5 Plot of the liquid and solid pair correlation functions corresponding to coexisting liquid and solid states for (a) 0.2M NaI at $T = 1.6T_0, P = 20.409\sigma^3/kT_0, \rho_{Liq}\sigma^3 = 1.069, \rho_{Sol}\sigma^3 = 1.104$ and (b) 0.3M NaCl at $T = 0.91T_0, P = 2.002\sigma^3/kT_0, \rho_{Liq}\sigma^3 = 0.754, \rho_{Sol}\sigma^3 = 0.798$. 68

6.1 The calculated form of the ordering operator distribution $P_L(\mathcal{M})$ for the L=8 system size, at the apparent critical parameters $T_c^* = -0.9433, \mu_c^* = -2.531$. Also shown for comparison is the universal fixed point ordering operator distribution $\tilde{P}_{\mathcal{M}}(x)$. The data have been expressed in terms of the scaling variable $x = a_{\mathcal{M}}^{-1} L^{\beta/\nu}(\mathcal{M} - \mathcal{M}_c)$, with the value of the nonuniversal scale factor $a_{\mathcal{M}}^{-1}$ chosen so that the distribution have unit variance. β and ν are the critical exponents for the coexistence curve and correlation length, respectively. 92

6.2 FSS results for (a) $T_c(L)$, (b) $\mu_c(L)$ and (c) $\rho_c^*(L)$ (See text for definitions) as a function of $L^{-(\theta+1)/\nu}$ and $L^{-(d+1)/\nu}$ respectively. 93

6.3 Probability distribution function of the density at the critical point T_c^*, μ_c^* for L=8,10,12,14. From outer plot to inner plot: L=8(pluses), L=10(crosses), L=12(asterisks), L=14(squares). 94

6.4 A series of calculated $P(\rho)$ obtained from multicanonical histogram reweighting corresponding to phase coexistence at temperatures displayed (L=8). 95

6.5 Phase diagrams of T vs ρ obtained from FSS/Gibbs/multicanonical histogram reweighting. Squares are the results obtained from the Gibbs ensemble and asterisks are the results of the multicanonical histogram reweighting method; filled circles are estimates of critical point from FSS. 96

6.6 Chemical potential μ vs. temperature T along the coexistence curve. By plotting μ vs $1/T$ we can obtain estimates of r (as shown in Table 6.1). 97

6.7 Phase diagrams of T vs ρ obtained from FSS/Gibbs/multicanonical histogram reweighting for systems with added salt type being NaI, NaCl, and non-polarizable salt, respectively. Squares are the results obtained from the Gibbs ensemble and asterisks are the results of the multicanonical histogram reweighting method; filled circles are estimates of critical points from FSS. 98

7.1 Unit cells of the (a) bcc-o and (b) fcc-o structures. In both cases the patches are aligned with the nearest neighbors. 122

7.2 Illustration of the patch definition. A patch α is described by a solid angle (half opening angle δ about an axis $\hat{e}_\alpha$ (unit patch vector)). The two particles in the figure attract each other through both the isotropic and anisotropic square well potentials, because their separation vector r_{ij} intersects some patch (not necessarily the same one) on both particles, and the particles are within range ($r_{ij} < k\sigma$). 123

7.3 Monte Carlo data of the mean squared displacements for the coupled solid (dots) compared with that of an Einstein crystal (solid line) at $T = 0.5$. We can see that $\lambda \to \lambda_{max}$, both $< r^2 - r_0^2 >$ and $< \sin(\Psi)^2 >$ converge to the theoretical value of the Einstein lattice. 124

7.4 (a) Liquid and fcc-d isotherms at $T = 0.9$. '$\circ$' and '+' are the Monte Carlo simulation results for liquid and fcc-d, respectively. The dotted curves are the fits to the data. The fitting formulas of isotherms are $\beta P_{Liq} = \sum_{i=1}^{m} c_i (\frac{\rho}{1-a\rho})^i$ for liquid and $\beta P_{Sol} = \sum_{i=0}^{4} c_i \rho^i$ for fcc-d. (b) $\beta\mu - \beta P$ plot at $T = 0.9$. Dotted line for liquid; solid line for fcc-d solid. 125

7.5 (a) bcc-o and fcc-o isotherms at $T = 0.1$. '$\square$' and '+' are the Monte Carlo simulation results for bcc-o and fcc-o, respectively. The dotted curves are the fits to the data. The fitting formulas of isotherms are $\beta P = \sum_{i=1}^{m} c_i (\frac{\rho-d}{1-a\rho})^i$ for both solids. (b) $\beta\mu - \beta P$ plot at $T = 0.1$. Dashed line for bcc-o; solid line for fcc-o. 126

7.6 (a) bcc-o and fcc-o isotherms at $T = 0.3$. '□' and '+' are the Monte Carlo simulation results for bcc-o and fcc-o, respectively. The dotted curves are the fits to the data. The fitting formulas of isotherms are $\beta P = \sum_{i=1}^{m} c_i (\frac{\rho - d}{1 - a\rho})^i$ for both solids. (b) $\beta\mu - \beta P$ plot at $T = 0.3$. Dashed line for bcc-o; solid line for fcc-o. Note that there are two pressures at which bcc-o coexists with fcc-o (reentrant behavior). 127

7.7 $T - \rho$ phase diagram of our model. Dots are Monte Carlo data. Asterisk-critical point, filled square-triple point, filled circle-the position where reentrant behavior occurs. The dashed lines are estimates following the trend of the MC data. The dotdashed line is an estimate of where the fcc-d-fcc-o transition occurs. 128

7.8 $P - T$ phase diagram of our model. Dots are Monte Carlo data. Filled square-triple point, filled circle-the position where reentrant behavior occurs. The dashed lines are estimates following the trend of the MC data. The dotdashed line is an estimate of where the fcc-d-fcc-o transition occurs. 129

Abstract

Crystallization/aggregation of globular proteins is an ongoing area of research. Phase diagrams serve as a tool to study the optimal conditions for such processes. They are of great importance, since we can either promote the nucleation process that leads to the formation of high quality protein crystals, or prevent unwanted aggregation that may cause diseases such as sickle cell anemia and Alzheimer's disease. In this study, we will calculate the phase coexistence curves for several interesting models.

Salts have commonly been used as a means to tune the interactions in electrolyte solutions. Not only salt concentration, but salt type plays a substantial role in precipitating proteins. This is known as the Hofmeister effect. We discuss two recently developed models and the resulting phase diagrams of the lysozyme solution for different types of added salt. These two models involve different approaches to explaining the Hofmeister effect. One focuses on the role of ion-dispersion forces; the other focuses on the role of hydrophobic surface forces. Due to the similarity between proteins and colloids, we also conduct a study of the fluid-fluid coexistence curves of an electrolyte solution of colloidal nanoparticle, Al_2O_3, by employing the method of Finite-size scaling.

Anisotropy almost always exists with real protein molecules. It can influence protein aggregation in many different ways, for example, it can lead to different nuclei shapes or crystal structures. We study a relatively simple patch model and generalize it in the

sense that the potential consists of two pieces: a two patch directional attraction piece plus a weaker isotropic attractive interaction. We show that the addition of this isotropic interaction leads to a complex phase diagram, with a metastable fluid-fluid coexistence curve and competing crystal structures (bcc and fcc) that can also be orientationally ordered or disordered. It is also possible that this model can lead to a fiber-bundle phase transition, as one might expect from the existence of the stronger patch-patch interaction (leading to chains) plus a weaker interchain interaction from the isotropic piece.

Chapter 1

Introduction

Proteins are an essential part of organisms and participate in every process within cells. Many proteins are enzymes that catalyze biochemical reactions and are vital to metabolism. Others have structural or mechanical functions, such as actin and myosin in muscle and the proteins in the cytoskeleton, which form a system of scaffolding that maintains cell shape. There are also proteins that play important roles in cell signaling, immune responses, cell adhesion, and the cell cycle, etc. All this suggests the crucial nature of normal protein functioning for living organisms, and particularly humans.

Needless to say, malfunctions of proteins will lead to diseases. Unwanted protein aggregation, for instance, is one possible malfunction and can cause serious problems. One such example is sickle cell anemia [111, 51, 16], which is caused by a point mutation in the β-globin chain of hemoglobin; the resultant sickle hemoglobin (HBS) proteins are prone to aggregating and forming long chain polymers (see Fig. 1.1). The polymers

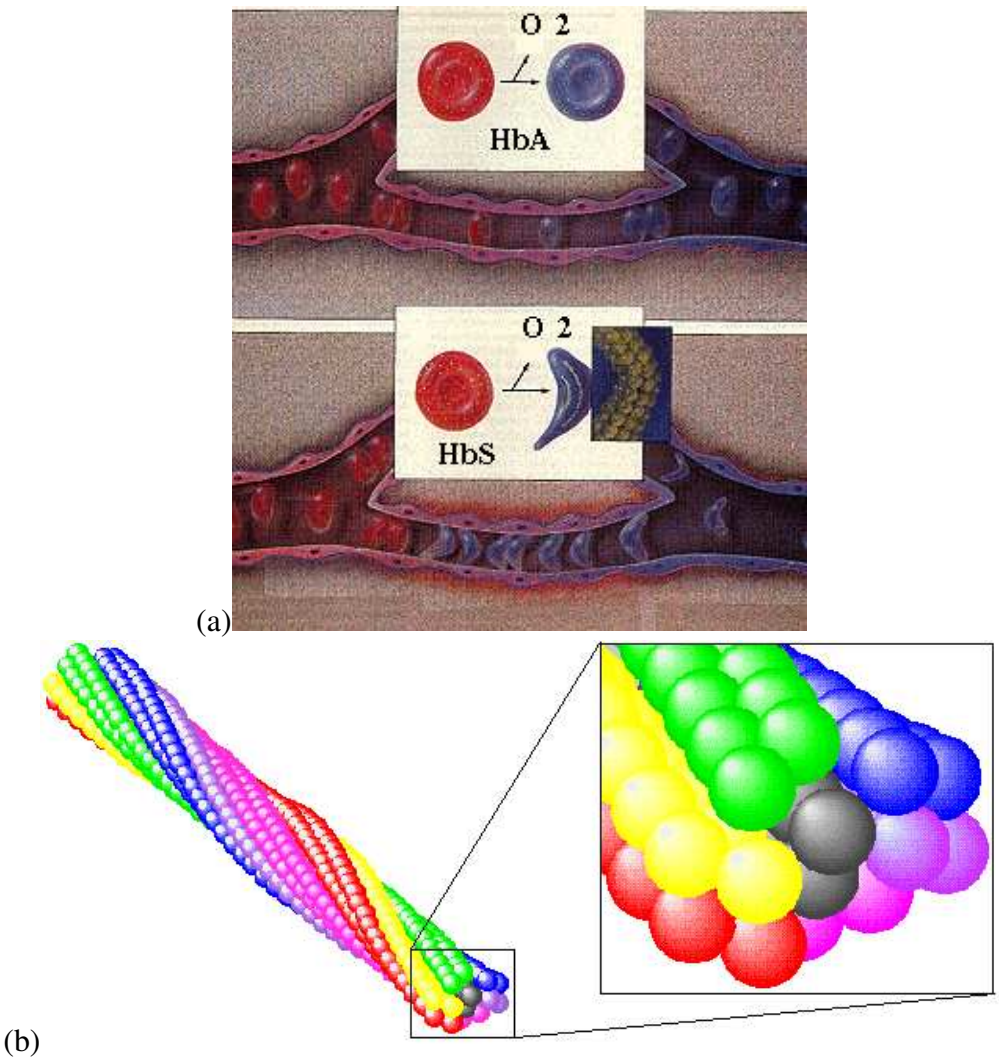


Figure 1.1: (a) Upper: normal red blood cells maintain their shape as they pass through the capillaries and release oxygen to the peripheral tissues. Lower: Sickle Hemoglobin molecules form bundles when releasing oxygen and deform into an abnormal shape, thus block the flow of cells and interrupt the delivery of oxygen. (b) Schematic of polymers of deoxygenated sickle hemoglobin molecules. Each hemoglobin molecule is represented as a sphere. The spheres twist in an alpha helical bundle made of 14 sickle hemoglobin chains.

distort the shape of the red blood cell and block the capillaries and deprive the body of oxygen. Other diseases caused by protein aggregation include cataracts [7, 105] and Alzheimer's disease [61, 40]. Thus, understanding the physical conditions that lead to such condensation is important in order to find possible means by which to slow down or prevent the process from occurring.

Protein crystallization, on the other hand, is of great significance. This is because ordered protein crystals can provide a way to determine the 3D structures of the protein through scattering techniques such as X-ray crystallography. Fig. 1.2 gives an example of protein crystals. The protein crystals provide a means to determine protein function since structure determines function. The crucial step in this process is making good crystals out of the protein solutions. Highly ordered crystals without defects, however, are extremely hard to grow. The growing of crystal typically consists of two stages - the nucleation stage and the growth stage. On one hand, the growth rate shouldn't be too fast in order to avoid aggregation, since this would sacrifice the quality of the crystal. On the other hand, one wants a reasonable nucleation rate for the stage prior to pure growth, so that the crystallization process occurs on a reasonable time scale. The physical conditions of the initial solution, as determined by experiments, sensitively affects the nucleation process. These conditions include temperature, pH, salt concentration, precipitant, and so on. To locate the optimal initial conditions, normally experimentalists have to go through "trial and error" - repeated crystallization attempts with many

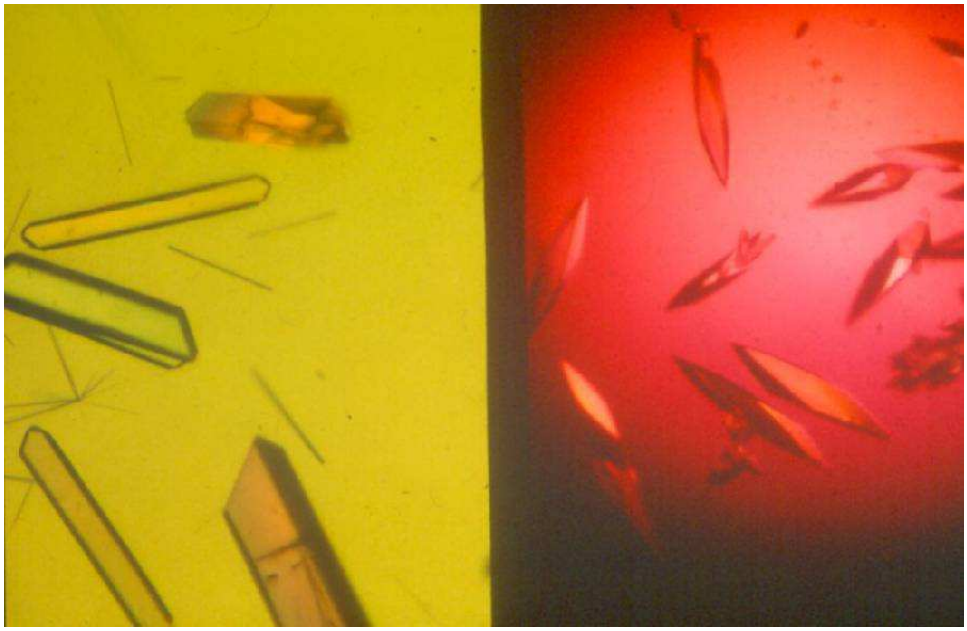


Figure 1.2: An example of crystallized proteins (Green pH7 Bovine γ_{BC} and red γ_{BC} minus Y).

different samples. But this strategy does not always work. Even when it is successful, the lessons learned cannot be easily generalized; the conditions which work with one protein are not necessarily optimal for a different protein.

Therefore, it would be useful if we can predict the appropriate temperature or salt concentrations necessary to grow good crystal. This has stimulated fundamental research on protein crystallization. An important tool in this work is the phase diagram. A complete phase diagram shows the state of a material as a function of all of the relevant variables of the system. For a protein solution, these variables include concentration of the protein, the temperature and the relevant salt concentration. The most common form

of the phase diagram for proteins is two-dimensional and usually displays the concentration of protein as a function of one parameter, with all other parameters held constant. A typical phase diagram for proteins is shown in Figure 1.3(A). The phase diagram can at least serve as a starting point for experimentalists, providing them with information on initial conditions of the solutions.

Studies have shown that not just the strength, but also the range, of the interactions between protein molecules is of crucial importance for crystal nucleation. It has been shown by George and Wilson [36] that protein solutions with a small and negative value of second osmotic virial coefficient B_2, tend to produce good crystals. B_2 describes the lowest order correction to the van't Hoff law for the osmotic pressure Π:

$$\frac{\Pi}{k_B T \rho} = 1 + B_2 \rho + O(\rho^2) \tag{1.1}$$

The relation between B_2 and interactions among molecules is as follows:

$$B_2 = 2\pi \int_0^\infty r^2 (1 - e^{-\beta V(r)}) dr \tag{1.2}$$

Here $\beta = 1/k_B T$ and V(r) is the interaction energy of a pair of molecules. George and Wilson found, by measuring B_2 for a number of proteins in different solvents, that solutions with small negative values of B_2 would largely enhance the crystallization process, while large negative B_2 favored aggregation of amorphous aggregates rather than crystallization. For large positive values of B_2, no crystallization occurred at all. They showed that optimal crystallization occurred within a narrow range of small negative

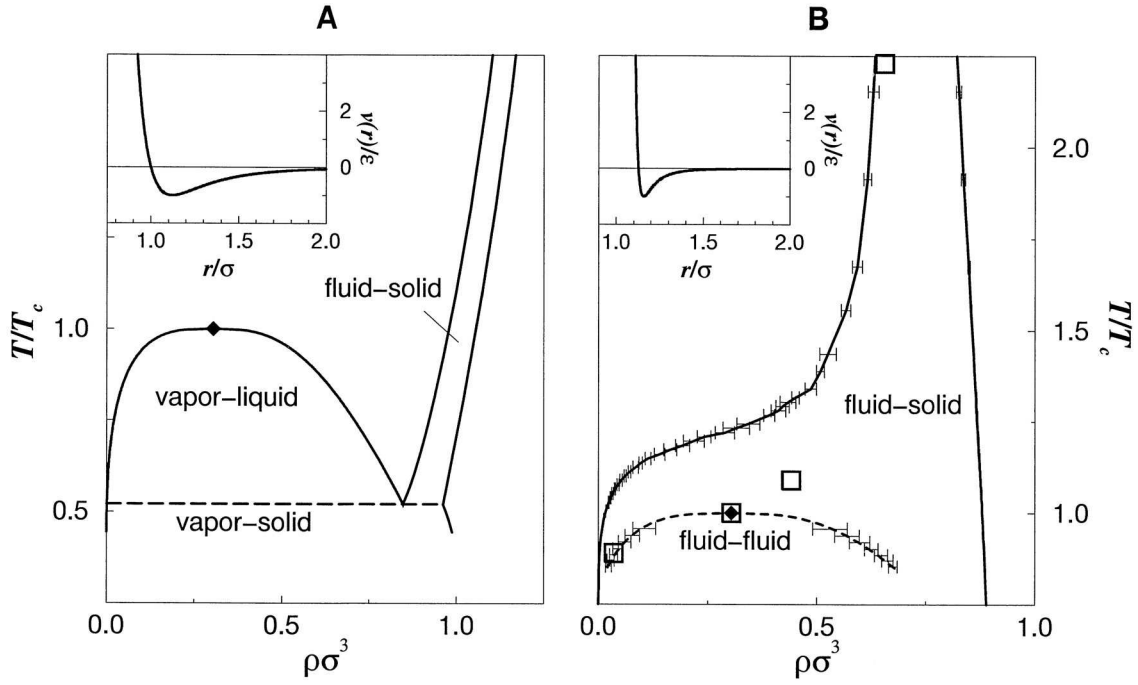


Figure 1.3: (A) Typical phase diagram for proteins with a relatively long-ranged attractive interaction. (B) Typical phase diagram for proteins with a relatively short-ranged attractive interaction. The potentials are given in inset graphs, respectively. (Reproduced from Ref. [109])

values of B_2, for about 20 globular proteins. Rosenbaum, Zamora and Zukoski [95, 96] then conducted a study to link the work of George and Wilson with earlier research on colloids. They found that the range of B_2 favoring crystallization corresponds to a **short range attractive interaction** in models of colloids.

A typical phase diagram of proteins with a relatively long range attractive interaction (in comparison with the diameter of the particle) is given in Fig. 1.3(A). As the interaction range is reduced, however, the stable liquid-gas critical point (marked with

a filled $\diamondsuit$) moves toward the triple point (dashed line) and eventually breaks away from the stable regime; it survives in the metastable regime below the fluid-solid coexistence curve as shown in Fig. 1.3(B). This often is the case for solutions of globular proteins. Frenkel and ten Wolde [109] demonstrated via computer simulation, that the nucleation rate can be enhanced enormously close to the metastable critical point. They argued that this is primarily because the pathway of the formation of the nucleus has been changed drastically. There is an intermediate step during which a liquidlike droplet is formed and as it grows, a crystalline nucleus forms inside the droplet. Fig. 1.4 from their paper clearly shows the change of the pathway. The nucleation barrier that separates two free energy wells can be strongly reduced in this way. Subsequent theoretical work of Talanquer and Oxtoby [107] , Shiryayev and Gunton [102] and Lutsko and Nicolis [73] using density functional theory supports this picture. Fig. 1.5 shows the plot of the free energy barrier for the phase points marked by squares in Fig. 1.3(B). This further verifies that the nucleation barrier close to T_c is much lower than at either higher or lower temperatures.

In this study we are going to study several models and determine the corresponding phase diagrams. In chapter 2 we summarize the Monte Carlo method used in this thesis. Chapters 3, 4 and 5 focus on the role of salt in precipitating proteins (Hofmeister effect) in solutions and the subsequent effects on phase transitions in such systems. In particular, we discuss one possible cause of the Hofmeister effect - hydrophobic surface

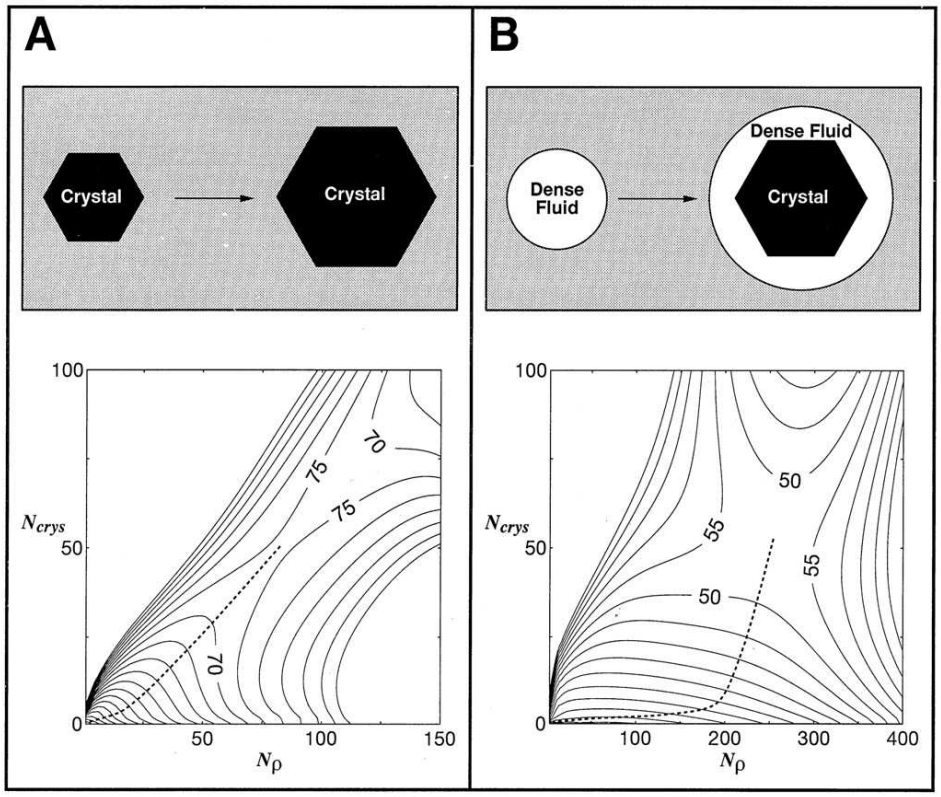


Figure 1.4: Contour plots of the free-energy landscape along the path from the metastable fluid to the critical crystal nucleus for a short-ranged Lennard-Jones potential. N_{rho} and N_{crys} are the total number of connected particles and that of solidlike particles in the nucleus. (A) The free-energy landscape well below the critical temperature (T/T_c=0.89). (B) As (A), but for T = T_c. (Reproduced from Ref. [109])

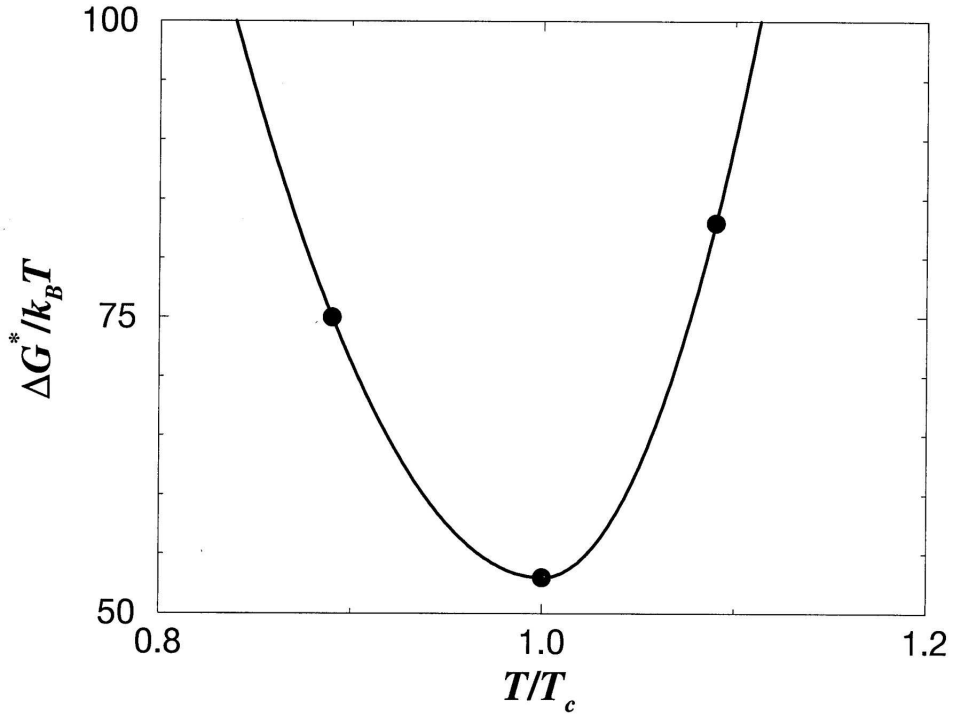


Figure 1.5: Variation of the free-energy barrier for homogeneous crystal nucleation, as a function of T/T_c, in the vicinity of the critical temperature. The solid curve is a guide to the eye. (Reproduced from Ref. [109])

forces in Chapter 3, followed by the discussion of two recently developed models and the resulting phase diagrams of the lysozyme solution with different types of added salt. These two models involve different approaches to the Hofmeister effect. One focuses on the role of hydrophobic surface forces; the other focuses on the role of ion-dispersion forces. In Chapter 6 we conduct a study of phase diagrams of an electrolyte solution of colloidal nanoparticle, Al_2O_3 due to the similarity between proteins and colloids. We dedicate Chapter 7 to an anisotropic model. Models with anisotropic interactions are more realistic descriptions of protein interactions and have recently been the subject of study. Our model is a relatively simple one, which nevertheless has an interesting phase diagram with competing crystal structures. We also hope that it will provide a basis to explain the formation of fibers and a nonequilibrium fiber-bundle transition [47]. This type of transition might be relevant to the cause of the sickle cell disease. Finally we present a brief conclusion and perspective in Chapter 8.

Chapter 2

Simulation Methods

2.1 Introduction to Importance Sampling

The Monte Carlo (MC) method is an effective way of calculating multidimensional integrals with complicated boundary conditions, which is exactly what we encounter in statistical physics. The simplest Monte Carlo technique, *random sampling*, however, is efficient only when the integrand is relatively smooth over the integrating interval. For a statistical average over configuration space, such as

$$\langle A \rangle = \frac{\int dr^N A(r^N) \exp[-\beta U(r^N)]}{\int dr^N \exp[-\beta U(r^N)]}, \tag{2.1}$$

most of the computing time is spent on points where the Boltzmann factor is negligible. One needs, however, to sample many points in the region where the factor is large and fewer points elsewhere. This is where the *importance sampling* comes into the picture,

since it is for this very job that importance sampling is designed; and we sample points on a known probability distribution which preserves the basic structure of the original one but is much simpler than it. An average as stated above, where a ratio of two integrals needs to be calculated, can be obtained by the specially devised *Metropolis method* [33]. First we rewrite the integral as below:

$$\langle A \rangle = \frac{\int dr^N A(r^N) \exp[-\beta U(r^N)]}{\int dr^N \exp[-\beta U(r^N)]} \tag{2.2}$$

$$= \int dr^N A(r^N) [\frac{\exp[-\beta U(r^N)]}{Z}] \tag{2.3}$$

$$= \int dr^N A(r^N) P_M(r^N) \tag{2.4}$$

where Z is the partition function, and $P_M = \frac{\exp[-\beta U(r^N)]}{Z}$ is the unknown absolute probability distribution.

The method is then described as follows [33]: Take the canonical ensemble as an example, its average of quantity A is given above. We first start out by randomly choosing an initial configuration and then perform a random walk in the configuration space and accept the new configuration with a certain probability determined by the relative probability between the new and old states. More specifically, first, give all the particles in the system a random position; then select a particle at random from this "old" configuration (o) and displace the particle by a random distance, and denote the new configuration as (n). Now we are going to accept this step with a probability $acc(o \to n) = \min[1, \rho_n/\rho_o]$, and simply using the Boltzmann distribution function as ρ would be a good approximation. Thus $acc(o \to n) = \min[1, \exp[-\beta(U_n - U_o)]]$.

Ultimately we expect the system to achieve a minimum in the free energy characteristic of the particular ensemble (e.g. Hemholtz free energy for canonical ensemble (constant NVT)). As implied above, a trial move with $U_n < U_o$ will always be accepted; and one with $U_n > U_o$ will also have a certain probability of acceptance - it implements the detailed balance condition, stating that the average number of accepted moves from o to any other state n is exactly canceled by the number of reverse moves. This is because we don't want to destroy equilibrium once it is reached. Actually, detailed balance is much stronger than necessary, and it is for convenience that we impose such a condition here.

One advantage of the Monte Carlo method is that it can be readily adapted to the calculation of averages in any ensemble. Next we are going to describe its implementation in several ensembles used later in this study.

2.2 Monte Carlo Simulation in Various Ensembles

2.2.1 Isobaric-Isothermal Monte Carlo

The isobaric-isothermal (constant-NPT) ensemble is widely used in Monte Carlo simulations, since it resembles the conditions under which most experiments are carried out. One can think of a constant-NPT ensemble as a system that is separated by a piston from an ideal gas reservoir (Fig. 2.2.1); the pistol is free to move. The subsystems

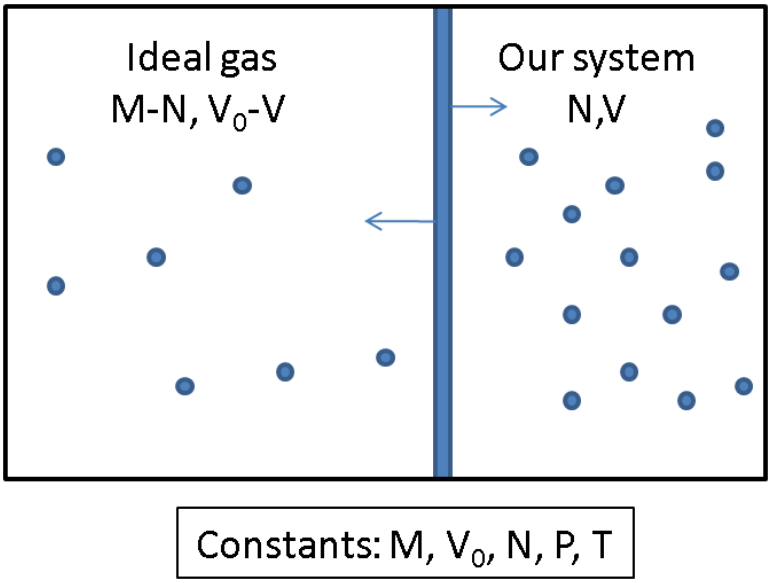


Figure 2.1: Illustration of constant-NPT ensemble. The pistol in the middle is free to move.

together have a total number of M particles and a total volume of V_0. The number of particles in our subsystem of interest is fixed at N, while it is allowed to exchange volume with the other $M - N$ ideal gas particles, i.e. V fluctuates around some average value. As $V_0 \to \infty$, the partition function of the total system can be written as:

$$Q(N, P, T) = \frac{\beta P}{\Lambda^{3M} N!} \int_0^\infty dV \exp[-\beta P V] V^N \int ds^N \exp[-\beta U(s^N; L)] \tag{2.5}$$

where Λ is the de Brogile wavelength, s is the scaled coordinate and $L = V^{1/3}, s = L^{-1} r$. It can be shown that the probability density to find the subsystem of interest in a particular configuration of the N atoms at a given volume V is given by [33]

$$\mathcal{N}(V; s^N) \propto V^N \exp\{-\beta[U(s^N, V) + PV - N\beta^{-1} \ln V]\} \tag{2.6}$$

In the constant-NPT ensemble, V is simply treated as an additional coordinate, and trial moves then include volume changes in addition to the regular particle displacements. In the Metropolis scheme such a random volume change from V to V' will be accepted with the probability

$$acc(o \rightarrow n) = \min[1, \exp(-\beta[U(V') - U(V) + P(V' - V) - N\beta^{-1} \ln(V'/V)])] \quad (2.7)$$

Rather than attempting random changes in the volume itself, sometimes it is easier to perform random changes in the box length L or in the logarithm of the volume. One can simply modify the partition function in a way such that L or $\ln V$ acts as the additional coordinate. The acceptance rule is then modified as

$$acc(o \rightarrow n) = \min[1, \exp(-\beta[U(V') - U(V) + P(V' - V) - (N+1)\beta^{-1} \ln(V'/V)])] \quad (2.8)$$

with $\ln V$ being the additional independent coordinate. The normal particle displacement is accepted according to

$$acc(o \rightarrow n) = \min[1, \exp(-\beta[U(V') - U(V)])] \quad (2.9)$$

2.2.2 Grand Canonical Monte Carlo

Grand-canonical ensemble (constant-μVT) is different from most other ensembles in that it does not conserve the number of particles. Instead, the chemical potential, together with volume and temperature, is fixed. We can view this ensemble as one immersed in an external reservoir of ideal gas particles; we allow the two to exchange

particles instead of volume. Thus, the subsystems have fixed volumes V and $V_0 - V$, respectively. And when an ideal gas particle is drawn from the external reservoir and placed in the system of interest, it goes from noninteracting to interacting with other particles within its subsystem (and vice versa). As a result, our system of interest can fluctuate in the number of particles N. The probability density to find a system with $M - N$ particles at reduced coordinates s^{M-N} in volume $V' \equiv V_0 - V$ and N particles at reduced coordinates s^N in volume V is [33]

$$\mathcal{N}(s^M; N) = \frac{V^N V'^{M-N}}{Q(M, V, V', T)\Lambda^{3M} N!(M-N)!} \exp[-\beta U(s^N)] \tag{2.10}$$

where Q is the total partition function of the system. In the limit of $M \to \infty, V' \to \infty, (M/V') \to \rho$, the corresponding probability density

$$\mathcal{N}_{\mu VT}(s^N; N) \propto \frac{\exp(\beta\mu N)V^N}{\Lambda^{3N} N!} \exp[-\beta U(s^N)] \tag{2.11}$$

The types of random moves for a grand-canonical ensemble include particle displacement, particle insertion and particle deletion. The acceptance rule of particle displacement is the same as in Equation 2.9; the insertion (creation) of a particle at a random position is accepted with a probability

$$acc(N \to N+1) = \min[1, \frac{V}{\Lambda^3(N+1)} \exp\{\beta[\mu - U(N+1) + U(N)]\}] \tag{2.12}$$

and the deletion (destruction) of a particle is accepted with a probability

$$acc(N \to N-1) = \min[1, \frac{\Lambda^3 N}{V} \exp\{-\beta[\mu + U(N-1) - U(N)]\}] \tag{2.13}$$

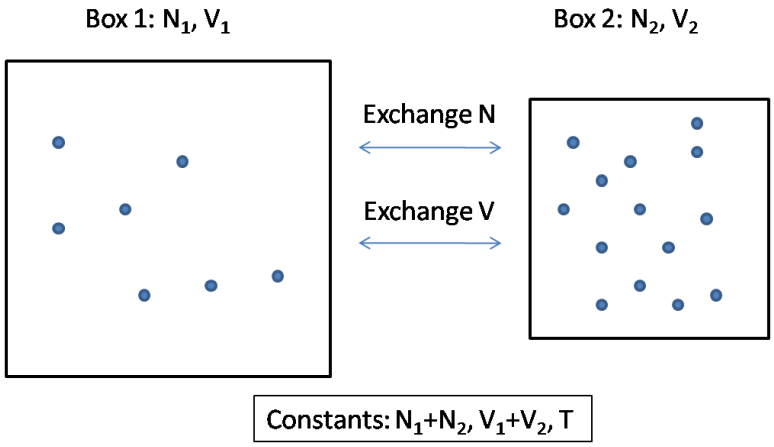


Figure 2.2: Illustration of Gibbs ensemble. Preserved quantities include: temperature T, the total number of particles $N_1 + N_2$, the total volume $V_1 + V_2$.

2.2.3 Gibbs Ensemble Monte Carlo

The Gibbs-ensemble Monte Carlo (GEMC) was designed by Panagiotopoulos [84] to study first-order phase transitions. GEMC employs two simulation boxes for the two coexisting phases. This method avoids the formation of an interface between the two coexisting phases, which can cause finite size problems with relatively small systems.

Two physically separate but thermodynamically connected simulation cells are used to mimic the two fluid phases (2.2.3). At a chosen simulation temperature T, standard particle displacements are performed within each simulation cell according to Equation 2.9; in addition, volume and particle exchanges are performed between the two cells, in order to meet the conditions for coexistence: $P_1 = P_2$ and $\mu_1 = \mu_2$. These exchanges are chosen such that the total volume V and number of particles N of the system are

conserved and the simulations obey detailed balance. The acceptance rule of a volume change of box 1 from V_1^o to $V_1^n = V_1^o + \Delta V$ (accompanied by the inverse change of $-\Delta V$ in box 2)

$$acc(o \to n) = \min\{1, \frac{(V_1^n)^{N_1}(V - V_1^n)^{N-N_1}}{(V_1^o)^{N_1}(V - V_1^o)^{N-N_1}} \exp\{-\beta[U(s_n^N) - U(s_o^N)]\}\} \quad (2.14)$$

Similarly to isobaric-isothermal ensemble, we can also perform random walks in $\ln[V_1/(V - V_1)]$, as long as the acceptance ratio is modified accordingly [33].

The acceptance rule for exchanging a particle between the two boxes (removing a particle from box 1 and inserting it in box 2) is:

$$acc(o \to n) = \min\{1, \frac{N_1(V - V_1)}{(N - N_1 + 1)V_1} \exp\{-\beta[U(s_n^N) - U(s_o^N)]\}\} \quad (2.15)$$

2.3 Quaternions and Their Use in Orientational Moves

If we are simulating anisotropic particles whose interactions depend on their orientations as well as their positions, we must also generate trial moves that change the orientation as well. There are many different ways in doing so, e.g. by rotating a particle about one of the three space-fixed axes chosen at random, by using Euler angles, or by using quaternions. We choose the last approach in our simulations (as in Chapter 7) because of its convenience to use, as well as that fact that it is computationally less expensive than the alternatives. Quaternions are an extension of complex numbers and defined as

$$q = q_0 + q_1 i + q_2 j + q_3 k, q_0, q_1, q_2, q_3 \in \mathbb{R} \quad (2.16)$$

and satisfy the rules $i^2 = j^2 = k^2 = ijk = -1$. The four coordinates map exactly onto a three-dimensional rotation matrix; one advantage of the quaternions is that their representation does not have the singularities that are characteristic of others like Euler angles. We list some of their characteristics as below:

1). The conjugate q^* of a quaternion q is defined as:

$$q^* = q_0 - q_1 i - q_2 j - q_3 k \tag{2.17}$$

2). Addition of two quaternions $q = (q_0, q_1, q_2, q_3)$ and $p = (p_0, p_1, p_2, p_3)$ are given as:

$$p + q = (p_0 + q_0) + (p_1 + q_1)i + (p_2 + q_2)j + (p_3 + q_3)k \tag{2.18}$$

$$\begin{aligned} pq = &(q_0 p_0 - q_1 p_1 - q_2 p_2 - q_3 p_3) + (q_0 p_1 + q_1 p_0 + q_2 p_3 - q_3 p_2)i \\ &+(q_0 p_2 - q_1 p_3 + q_2 p_0 + q_3 p_1)j + (q_0 p_3 + q_1 p_2 - q_2 p_1 + q_3 p_0)k \end{aligned} \tag{2.19}$$

3). The length/norm of a quaternion is:

$$n(q) = \sqrt{qq^*} = \sqrt{q^* q} = \sqrt{q_0^2 + q_1^2 + q_2^2 + q_3^2} \tag{2.20}$$

4). The inverse of the a quaternion q^{-1} is

$$q^{-1} = \frac{q^*}{qq^*} \tag{2.21}$$

Also, there is a one-to-one correspondence between quaternions and Euler angles,

$$
\begin{aligned}
q_0 &= \cos\frac{\theta}{2}\cos\frac{\phi+\psi}{2} \\
q_1 &= \sin\frac{\theta}{2}\cos\frac{\phi-\psi}{2} \\
q_2 &= \sin\frac{\theta}{2}\sin\frac{\phi-\psi}{2} \\
q_3 &= \cos\frac{\theta}{2}\sin\frac{\phi+\psi}{2}
\end{aligned}
\tag{2.22}
$$

In practice, when randomly rotating a vector $\overrightarrow{p}$, we create a rotation matrix M from a randomly generated quaternion and multiply $\overrightarrow{p}$ by this matrix, i.e. $\overrightarrow{p'} = M\overrightarrow{p}$ with

$$
M = \begin{pmatrix}
q_0^2+q_1^2-q_2^2-q_3^2 & 2q_1q_2-2q_0q_3 & 2q_0q_2+2q_1q_3 \\
2q_0q_3+2q_1q_2 & q_0^2-q_1^2+q_2^2-q_3^2 & 2q_1q_3+2q_0q_1 \\
2q_1q_3-2q_0q_2 & 2q_0q_1+2q_2q_3 & q_0^2-q_1^2-q_2^2+q_3^2
\end{pmatrix}
$$

It may seem rather odd to use quaternions to describe spatial orientations in an MC simulation, since we still need to generate a rotation matrix to multiply the vectors with. However, the advantage of the quaternions over other approaches, e.g. Euler angles, lies in the fact that the latter usually requires the evaluation of sines and cosines, which are computationally expensive operations. Furthermore, quaternions avoid the problem of gimbal lock common to Euler angles.

To generate a random orientation with quaternions, one just need to generate points uniformly distributed on the surface of a 4D-sphere of radius 1

```
double S1,S2;
do
{
    q[0] = 2*(rnd2.rnd() - 0.5);
```

```
    q[1] = 2*(rnd2.rnd() - 0.5);
}while( (S1=q[0]*q[0]+q[1]*q[1]) >= 1 );
do
{
    q[2] = 2*(rnd2.rnd() - 0.5);
    q[3] = 2*(rnd2.rnd() - 0.5);
}while( (S2=q[2]*q[2]+q[3]*q[3]) >= 1 );
S1 = sqrt((1-S1)/S2);
q[2] = q[2]*S1;
q[3] = q[3]*S1;
```

Since the patchy particles we study are spherical, we only need to rotate them with respect to the center, i.e. it suffices to simply add random quantities to the different components of a quaternion and then normalize it.

```
double qq[4];
GetRandomQuaternion(qq);
q[0] += 0.01*qq[0];
q[1] += 0.01*qq[1];
q[2] += 0.01*qq[2];
q[3] += 0.01*qq[3];
double q_abs = sqrt( q[0]*q[0] + q[1]*q[1] + q[2]*q[2] + q[3]*q[3] );
q[0] /= q_abs;
q[1] /= q_abs;
q[2] /= q_abs;
q[3] /= q_abs;
```

Chapter 3

Introduction to Hofmeister Series and Hydrophobic Surface Forces

3.1 Hofmeister Series

The Hofmeister series originates from the ranking of the relative effectiveness of various types of salt in precipitating protein solutions and dates back to 1888 [45]. Since then, numerous experimental studies have shown the importance of specific ion effects in a multitude of biological and physicochemical phenomena. Examples include the precipitation of proteins from solution, the surface tension of salt solutions, ions binding to micelles, colloid stability, transport across red blood cells and the cutting efficiency of DNA in buffered salt solutions (see, e.g. [41, 12] for references). The Hofmeister effects are generally more pronounced for anions than for cations. Fig. 3.1 shows the typical

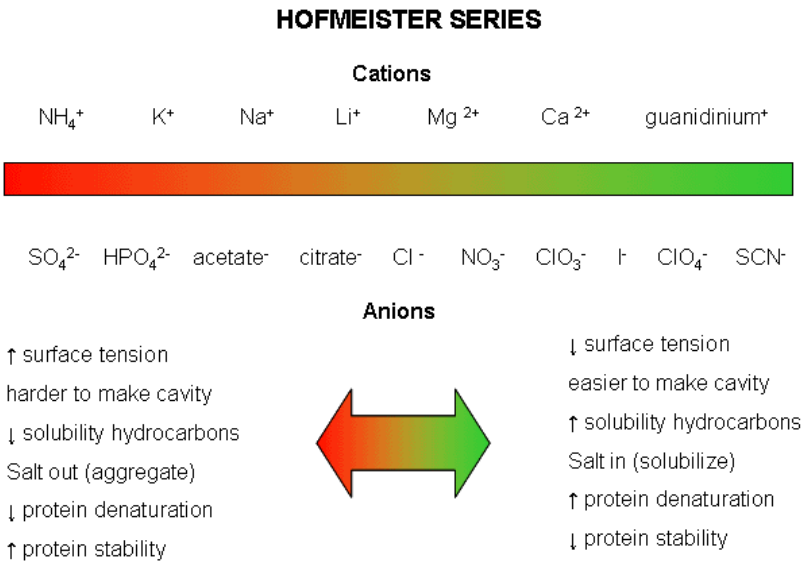


Figure 3.1: Typical ordering of anions in Hofmeister series and some relevant properties. Adapted from: http://tinyurl.com/ed5gj.

ordering of anions and some of its related properties.

Despite the fact that the Hofmeister series plays a significant role in a broad range of phenomena, the precise origin of action of the ions in the series has not yet been clarified and no generally accepted explanation exists at the molecular level; understanding this effect remains a major challenge for theorists. Originally, it was thought that ions modify the structure and properties of water and the ability of doing so varies from ion to ion. For example, one talks about “chaotropic” and “cosmotropic” ions, “hard and soft ions”, etc. Recent time-resolved and thermodynamic studies of water molecules in salt solutions, however, demonstrate that bulk water structure is not central to the Hofmeister

effect. Instead, the focus has been turned to developing models that depend upon direct ion-macromolecule interactions as well as interactions with water molecules in the first hydration shell of the macromolecule. The classical Derjaguin-Landau-Verwey-Overbeek (DLVO) theory of interparticle interactions in colloid science fails to explain this effect since it depends only on the salt concentration and not on the salt type. The DLVO theory treats colloid stability in terms of a balance between attractive van der Waals forces and repulsive double-layer forces between the solute particles [26, 115].

Recently, there have been two parallel developments that have provided considerable insights as to the causes of the Hofmeister effect. In the first approach, this effect has been attributed to nonelectrostatic, ion-dispersion forces [80, 60, 11, 67] that had previously been neglected in standard treatments such as the DLVO theory. The second approach emphasizes the importance of including the effective interactions between ions and interfaces, treating the surface of a macrosphere (protein or colloidal particle) to be the interface. These two complementary approaches have demonstrated the importance of including short-range interactions that account for both ion dispersion forces and short-range ion hydration effects. Indeed, a recent paper uses a parametrized potential of mean force that includes both ionic dispersion forces and short-range ion hydration to study ion specific effects for the double layer pressure between two uncharged interfaces[66].

I am going to briefly review the second approach, namely, the ion surface effects

in the following section. If the reader is interested in the first approach, please refer to Refs. [80, 60, 11, 67].

3.2 Hydrophobic Surface Forces

Understanding the mechanism of the solvation and adsorption of ions at aqueous interfaces is not only of fundamental interest but also of practical significance, since it exists in a broad range of physical, chemical and biological systems. Examples include chemical reactions at the interface, ion transport in atmospheric processes, and environmental problems such as the interaction of contaminated organic solvents in groundwater. In particular, the forces between ions and the surface of large protein molecules/spheres is a possible cause for the ion-specific effects in electrolyte solutions of protein.

3.2.1 Ion Adsorption at Liquid Interfaces

The distribution of ions and/or counterions at the interfaces plays an important role in the interaction and stability of large particles. The conventional view is that ions prefer to stay in the aqueous bulk, causing a depletion of ions from the aqueous interface. This view is in line with the experimentally observed increase in the surface tension by the addition of simple salts such as NaF and LiCl, through an interpretation based on the Gibbs adsorption isotherm [38, 1]:

$$\Gamma = -\frac{1}{RT}(\frac{d\gamma}{d\ln a}) \tag{3.1}$$

where Γ is the surface excess concentration of the solute (ion), R is the ideal gas constant, T is the temperature, and γ is the surface tension. In dilute solutions, a is proportional to the concentration. This theory can be qualitatively explained by the concept of the image charge: it can be shown that an aqueous ion with charge q induces a fictitious image charge $q' = q(\epsilon-1)/(\epsilon+1)$, where $\epsilon \approx 80$ is the dielectric constant of water. The image charge has the same sign and practically the same magnitude and repels the ions from the surface, thus reduces the concentrations of ions at the interface. This picture, however, is based on the assumption that no other forces than electrostatic interactions come into play. Although the electrostatic interactions are a key contributor to the total potential, they do not give the entire story, since direct interactions between ions and the nonpolar, hydrophobic part of the interface do exist. The air/water interface has been studied extensively in the past decade, and we will summarize briefly the progress in the subsequent section, and also describe in a bit of more detail one particular model employed by Dang [22].

Air/Water Interface

The air/water interface is the simplest type of aqueous interface. Considerable progress has been made during the past few years in understanding the equilibrium properties of

ion solvation at the air/water interfaces. The current understanding of ion solvation at the air/water interface is that small nonpolarizable ions are repelled from the interface while bigger ions with greater polarizabilities are attracted to the interface. As a result, the concentration of heavier halides (Br^- and I^-) is greater at the interface than that in the bulk while the inverse is true for lighter halides (F^- and Cl^-). We can summarize these findings in the series with increasing surface propensity $F^- < Cl^- < Br^- < I^-$.

Extensive Molecular Dynamics (MD) simulations have been carried out to study the ion adsorption/transport on the air/water interface [124, 123, 57, 52, 22, 24, 23, 35, 53]. The models employed by these simulations fall into two categories: nonpolarizable potential models (pairwise additive model) and polarizable potential models (non-additive many-body model). The polarizable model differs from the nonpolarizable model in its incorporation of many-body interactions (dipole-dipole, charge-dipole, etc.) into the potential. These many-body interactions are especially critical for the study of interfacial environments, since water molecules behave differently at the interface than in bulk solution, i.e. they show a preferred orientation and consequently induce a difference in electrostatic potential between the liquid and vapor phases. As a result, the resulting electric field strongly polarizes the ions. Larger, softer ions such as I^-, Br^- can then experience a greater increase in their induced dipole moments than smaller ions. When this polarization stabilization suffices to compensate the electrostatic penalty, the ions exhibit a favorable surface adsorption. On the contray, the electron clouds for smaller

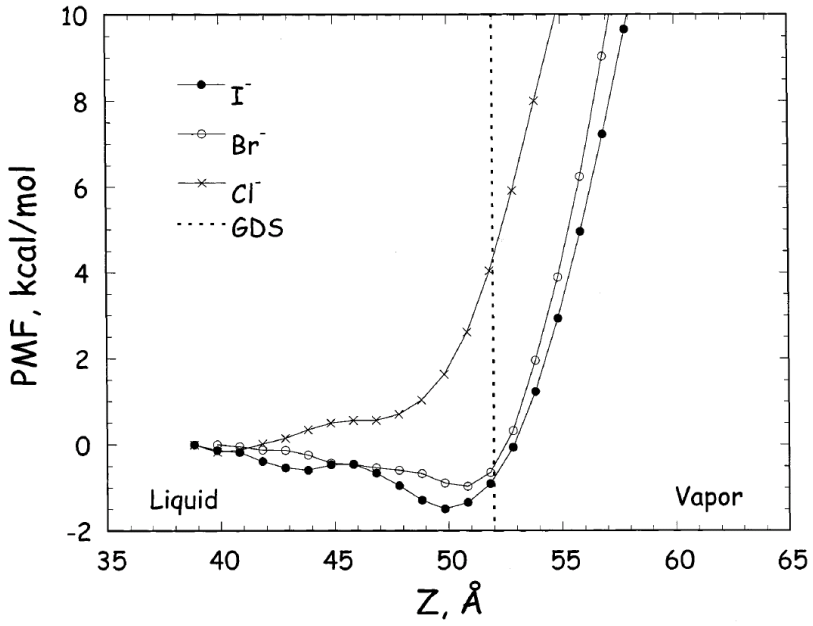


Figure 3.2: Computed free energy profiles for ions binding to the liquid/vapor interface of water at 300 K using polarizable potential models (Reproduced from Ref. [22]).

ions are not as readily to be distorted to react with the interfacial electric field as for larger ions, leading to the repulsion from the interface.

In particular, we present below the model used by Dang [22] to describe the ion solvation at the air/water interface. The total interaction energy of the system is summarized as follows:

$$U_{tot} = U_{pair} + U_{pol} \tag{3.2}$$

and

$$U_{pair} = \sum_i \sum_j (4\epsilon[(\frac{\sigma_{ij}}{r_{ij}})^{12} - (\frac{\sigma_{ij}}{r_{ij}})^6] + \frac{q_i q_j}{r_{ij}}) \tag{3.3}$$

where r_{ij} is the distance between site i and j, q is the charge, and σ and ϵ are the Lennard-Jones parameters, and

$$U_{pol} = -\sum_{i=1}^{N} \mu_i \cdot E_i^0 - \frac{1}{2} \sum_{i=1}^{N} \sum_{j=1, i \neq j}^{N} \mu_i \cdot T_{ij} \cdot \mu_j \tag{3.4}$$

where E_i^0 is the electric field at site i produced by the fixed charges in the system, μ_i is the induced dipole moment at atom site i, and T_{ij} is the dipole tensor. U_{pol} has three components: the first term as the charge-dipole interaction, the second term as the dipole-dipole interaction, and the last term as the energy associated with the generation of the dipole moment μ_i. The optimized interaction parameters are obtained by running MD simulations to match experimental data such as solvation enthalpies and hydration numbers as well as the data reported from accurate electronic structure calculations for the clusters.

Dang [22] calculated the free energy profiles of moving a single halide ion from the aqueous bulk into the vapor phase across the air/water interface. Fig. 3.2 depicts the results which clearly show that the profiles depend critically on the ion types. The larger ions Br^- and I^- show a minimum in the free energy profile near the interface, suggesting their propensity to bind to the interface, while Cl^- shows no such minimum. In another work [52], Jungwirth and Tobias calculated the density profiles of the ions near the interface, shown in Fig. 3.3. Note that both Br^- and I^- density profiles are characterized by a prominent peak close to the interface; this is in good agreement with

their free energy minima obtained by Dang (Fig. 3.2).

Along with the progress made with simulations and theories, novel experimental techniques (e.g. SHG,SFG,X-ray photoelectron spectroscopy) have made it possible to probe ions and molecules at the interface. Many experimental studies support the conclusion that larger ions may be preferentially absorbed at the air/water interface. [68, 92, 39, 89, 88, 37]

Solid/Liquid Interface

The solid/liquid interface, however, is not well understood yet. The difficulty on studying such interfaces stem from the complexity of the interfacial system, where forces of various origins act. There have been attempts to model such systems with a focus on only certain specific contributions to the total energy [9, 75, 74]. In particular, Lund et al. [71, 72, 70, 69] did a series of studies to investigate hydrophobic effects on the interfaces between the solvent and a model macromolecule. We briefly discuss their work below.

Lund et al. [71, 69] first consider a model macromolecule as a large, nonpolar sphere with charges distributed on the surface as shown in Fig. 3.4, left. The sphere is immersed in a surrounding of water molecules, Na^+, I^- and F^-, with the number of I^- equal to that of F^-. For the types of anions, they choose the two extremes from the halide group, fluoride and iodide; the former represents a small, highly solvated species, while the latter exemplifies a large, poorly hydrated ion. The configurational space is then sampled

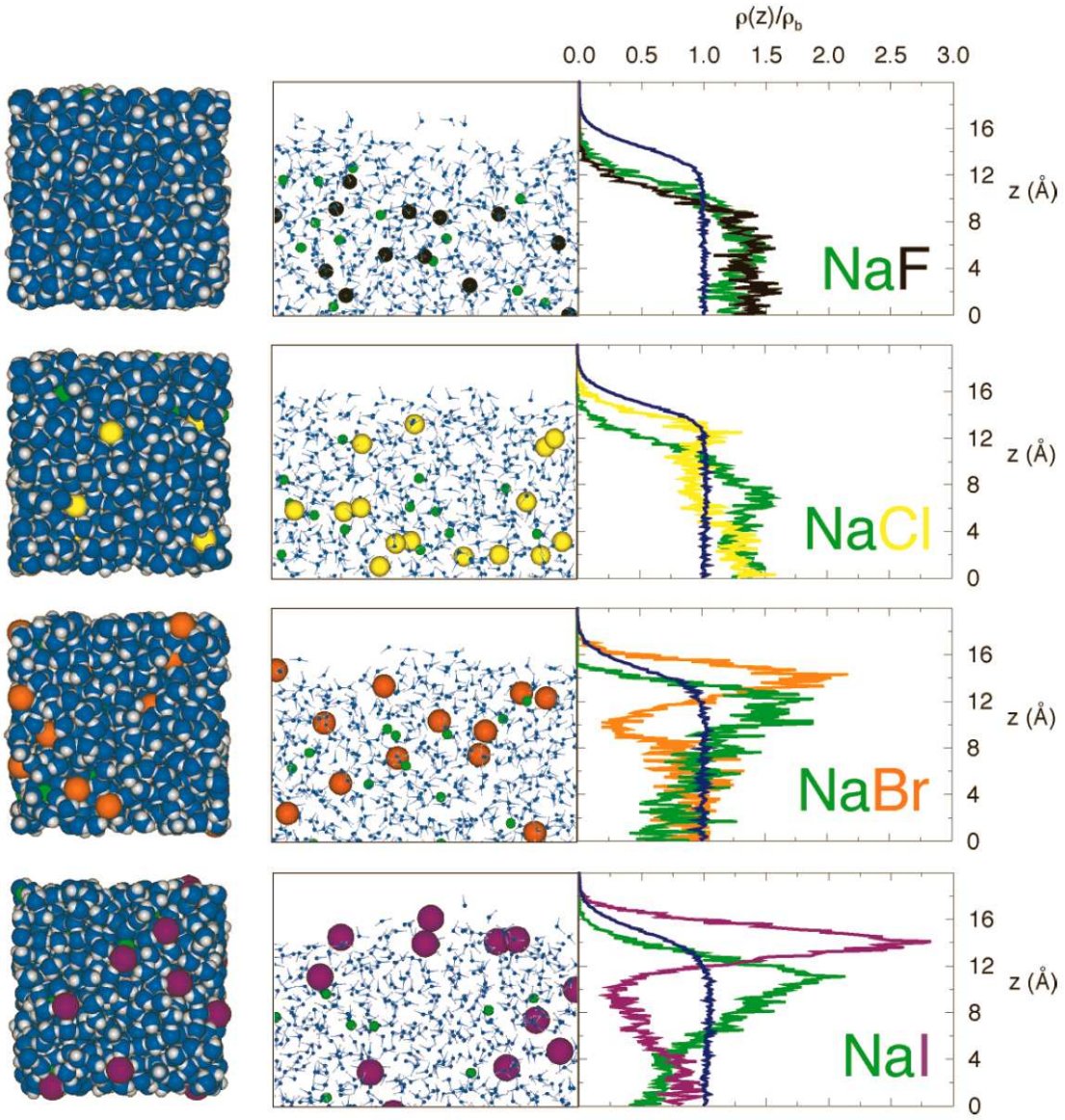


Figure 3.3: Snapshots (left-top view, middle-side view) of the solution/air interfaces of 1.2 M aqueous sodium halides from the molecular dynamics simulations; density profiles (right, number densities) of water oxygen atoms and ions plotted vs distance from the center of the slabs in the direction normal to the interface, normalized by the bulk water density (Reproduced from Ref. [54]).

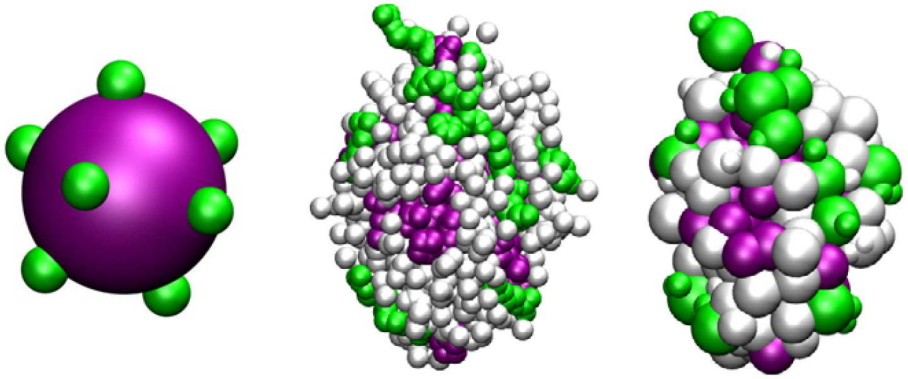


Figure 3.4: Three models for macromolecules with hydrophobic (purple/dark grey) and cationic surface groups (green/light grey). Left: a non-polar sphere with positively charged patches. Middle: the lysozyme in atomistic detail. Right: the lysozyme coarse grained to the amino acid level. (Reproduced from Ref. [69])

in the NPT-ensemble using MD simulations in a cubic box with periodic boundaries. Energies and forces are based on a pair potential function comprised of Coulomb and Lennard-Jones (LJ) interactions. The obtained potential of mean force (PMF) between the nonpolar sphere and iodide or fluoride, is displayed in Fig. 3.5, respectively. The small and well hydrated ion, fluoride, is repelled as expected from classical reaction field continuum arguments. Iodide on the other hand is large, poorly hydrated and is attracted to the non-polar interface. They argue that iodide's affinity to the surface has the character of a hydrophobic attraction, driven mainly by the solvent [71, 69].

In the next step, Lund and Jungwirth [69] proceed to a "real" protein molecule with a complex arrangement of ionic and nonpolar surface groups treated in atomistic detail

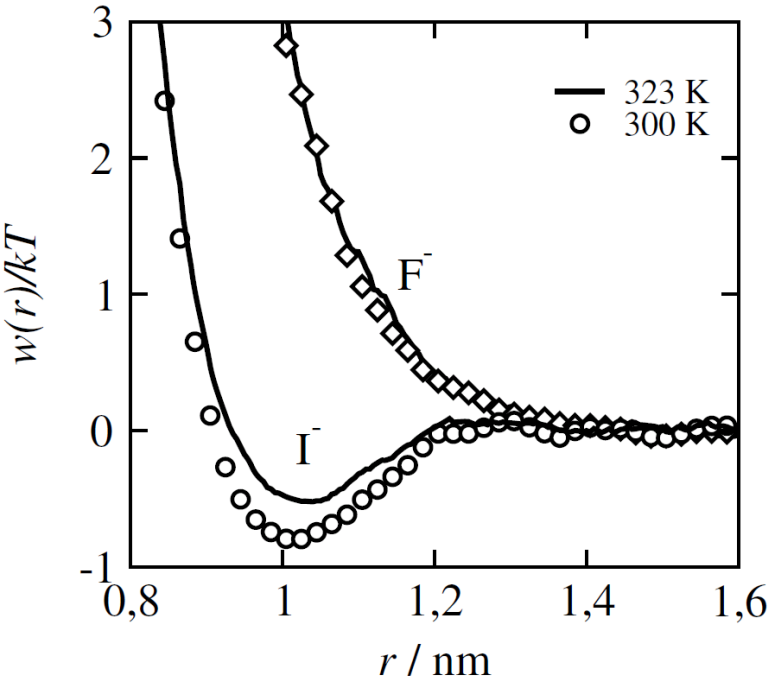


Figure 3.5: Simulated potential of mean force, w(r), for fluoride and iodide with a non-polar, nanosized sphere (Reproduced from Ref. [69]).

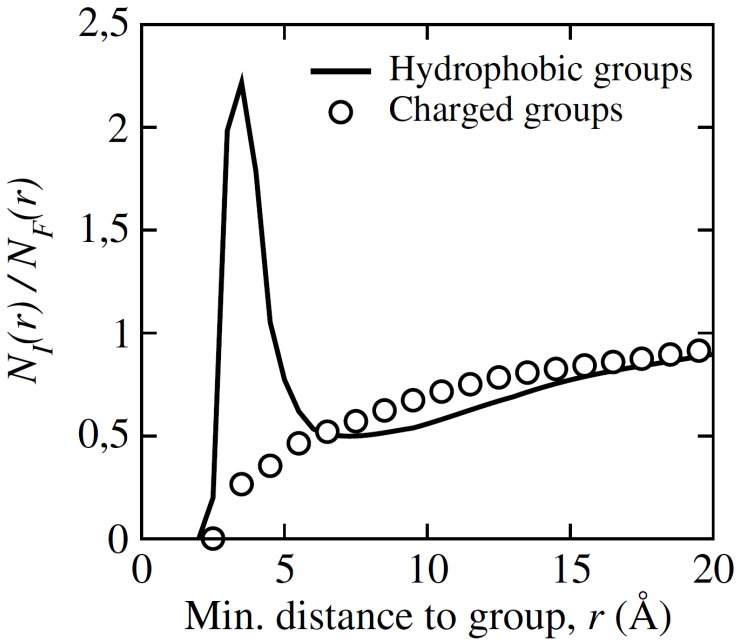


Figure 3.6: Relative cumulative sums, N(r), of fluoride and iodide for charged and non-polar patches in lysozyme, simulated in atomistic detail at pH 4.5, 150 mM salt (Reproduced from Ref. [69]).

(Fig. 3.4, middle). In addition to the Coulomb and LJ interactions, energies associated with polarization are also taken into account. Again a similar ion-binding pattern is observed. Fig. 3.6 plots the relative cumulative sums of I^- vs. F^- around nonpolar and cationic residues on lysozyme: F^- prefers to stay close to the cationic residues, while I^- is the favored ion near hydrophobic groups. The same conclusion is attained as before in the I^- is attracted to the non-polar, hydrophobic surface, while F^- dislikes such surfaces. They argue that F^- interact with protein surfaces mainly via direct attraction of aqueous anions with positively charged amino acid residues (ion-pairing effect), while I^- interact mainly via the hydrophobic surface forces (the ion-pairing effect is also at play, but very weak). The resulting ion-binding pattern is hence governed by the distribution and abundance of charged and nonpolar groups on the surface of a specific protein.

These studies provide some insight into the ion behavior at protein surface, however, they are far from the complete picture. The understanding of ion-specific effects requires all acting forces be considered. No such studies have been conducted until very recently when Dorinek et al. claimed in one study that they accounted for all relevant forces including solvent-mediated effects. We will not discuss their study here, but interested readers can refer to Ref. [46] for more details.

3.2.2 Effects of Ion Adsorption on Protein Aggregation

From the discussion above, it is reasonable to argue that ion adsorption at hydrophobic surfaces influences protein aggregation since the absorbed/unabsorbed ions can ultimately modify the effective interactions between protein molecules. On the experiment side, light scattering experiments and crystallization studies show that the self-association of the positively charged proteins is assisted by large anions such as iodide and thiocyanate [62, 90, 91, 31]. It is thus of great interest to conduct further studies on how surface modified solvation affects protein aggregation.

The most recent application of molecular dynamics simulations has been to provide a step toward including a solvent induced ion-specific surface interaction in an MC study of the interaction between lysozyme molecules in an aqueous salt solution [70]. In this study Lund et al. perform coarse grained Monte Carlo simulations of two lysozyme molecules (3.4, right); the solvent is treated as a dielectric continuum, but solvent structure effects are implicitly included. The authors obtained the potential of mean force between two lysozyme molecules in various solutions of sodium chloride and sodium iodide, respectively. As shown in Fig. 3.7 , the electrostatic repulsion between the proteins is effectively screened and becomes attractive with increasing salt concentrations. We note that in all cases iodide leads to more attractive protein interactions than chloride as is also observed experimentally.

They also calculated the distribution of ions (Fig. 3.8), revealing that the iodide

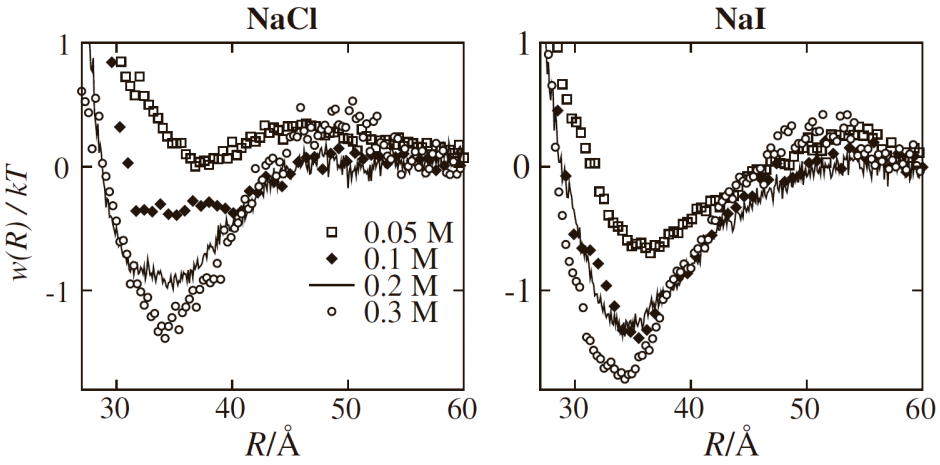


Figure 3.7: Potential of mean force w(R) between two lysozyme molecules in various solutions (0.1M) of sodium chloride and sodium iodide, respectively. R is the protein mass-center separation (Reproduced from Ref. [70]).

density in the midplane between the proteins is roughly twice that of chloride, for a 0.1 M salt solution, in accordance with findings in the previous section. They hence argue that iodide may enhance the attractive protein-protein interaction by bridging nonpolar surface groups on the proteins in addition to neutralizing the charges.

In accordance with the previous discussion, they find that there are at least two effects responsible for the Hofmeister series in this approach. Namely, it is the direct interaction of hydrated anions (ion-pairing) with positively charged amino acid residues as well as the affinity of these anions for hydrophobic patches at protein surfaces. The former interactions are stronger for chloride than for iodide, whereas the opposite is true for the second effect. As mentioned in the previous section, the effective interac-

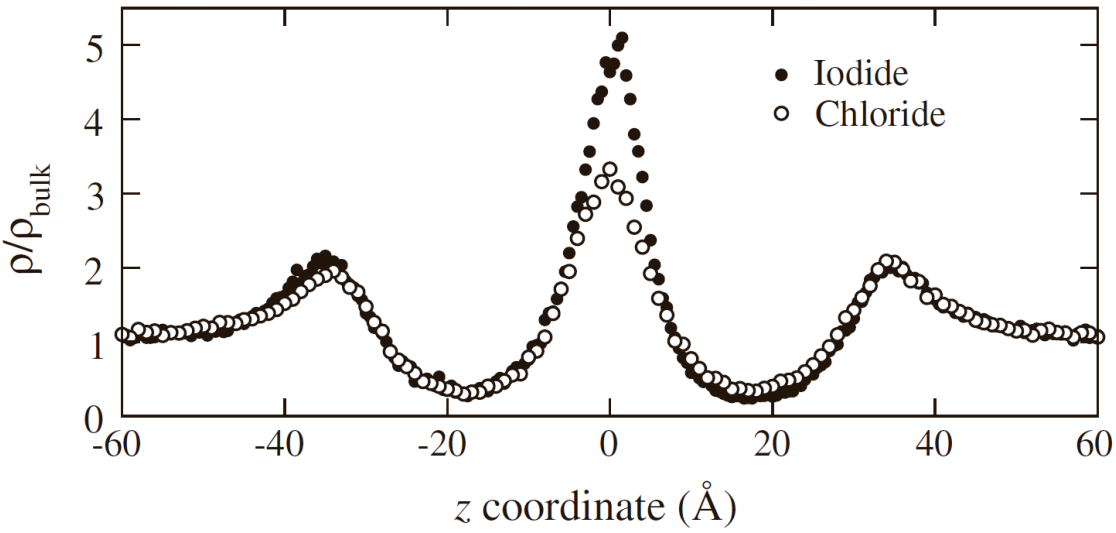


Figure 3.8: Cylindrical average of the anion concentration along the axis z connecting the two (fixed) mass centers of the rotating proteins at a 35 $\mathring{A}$ separation. The cylinder radius is 16 $\mathring{A}$ approximately the size of lysozyme and the salt concentration is 0.1 M. (Reproduced from Ref. [70]).

tion mechanism in a particular salt solution results from a subtle balance between these (and perhaps other) effects. The fact that there is a stronger lysozyme-lysozyme interaction in aqueous NaI than NaCl is due to the hydrophobic effect of iodide surpassing the ion-pairing effect of chloride.

To conclude this chapter, we want to stress that the mechanism of the Hofmeister effect is still not entirely clear and further studies are necessary for a thorough understanding, possibly combining both the hydrophobic effect and the dispersion effect.

Chapter 4

Ion-Dispersion Effect and the Phase Diagram of Aqueous Lysozyme Solution with NaSCN Electrolyte

4.1 Introduction

In Chapter 3, we have briefly described the origin of the Hofmeister effect, together with some recent progress in its understanding. In this chapter, we study how the Hofmeister effect manifests itself in the phase diagrams of globular proteins (lysozyme) in aqueous electrolyte solutions. As discussed in Chapter 1, the phase transitions, self-assembly, and aggregation of proteins in solution are of fundamental and practical importance [41]. Thus it is interesting to determine the Hofmeister effect on the phase diagram and

crystal nucleation rate of aqueous solutions of proteins.

As discussed in Chapter 3, there are quite a few possible causes of the Hofmeister effect, among which is the ion dispersion effect. In 1997 Ninham and Yaminsky [80] proposed that the ionic dispersion potential between the salt ion and solute particle, neglected in the DLVO theory, might provide a partial explanation of the Hofmeister effect. Since then a series of papers have been written applying this idea to a variety of examples of the Hofmeister effect, including the important case of globular proteins in solution [41, 12, 13, 128, 60, 108, 10].

In this chapter we focus on the role of ion specificity on equilibrium properties, i.e. we calculate the phase diagram of lysozyme in an aqueous solution with an added salt NaSCN, using a recent calculation of the lysozyme potential of mean force (PMF) that includes the effect of the ion-dispersion forces for this salt [11]. Their calculation of the PMF also includes a screened Coulomb interaction between the lysozyme molecules. In Ref. [11], Boström et al. have shown that the inclusion of ion-specific dispersion potentials gives rise to ion-specific phase diagrams, as one would expect for systems which exhibit the the Hofmeister effect. Boström et al. examined a model for which they considered the effect of three distinct monovalent salts with different anions on the phase diagram of the solute: NaCl, NaSCN and NaI (all at the same molarity 0.2 M). Their results show that the potentials of mean force between the lysozyme molecules become more attractive from NaCl to NaI to NaSCN, which is consistent with the exper-

imental observation that NaSCN is more effective in precipitating hen-egg-white(HEW) lysozyme. Using their salt based PMF contribution to the total potential, they calculated phase diagrams for the three electrolyte solutions by using a first order Barker-Henderson perturbation theory [5, 44] for the liquid and the solid phases and found that the three phase diagrams were qualitatively different. In particular, they found that the liquid-liquid curve was metastable with respect to the solubility curve for NaSCN.

It is well known that a first order perturbation theory is not quantitatively accurate; thus it is of interest to obtain more accurate phase diagrams for these systems. In this chapter, we address this question using the Boström et al. model [11] for NaSCN, to predict the corresponding phase diagram using systematic Monte Carlo techniques. In particular, we investigate the predicted metastability of the fluid-fluid phase obtained from perturbation theory. Our results show that the metastability gap we obtain for the case of NaSCN is greater than predicted by perturbation theory.

The remainder of the chapter is as follows: in Sec. 4.2 we summarize the model while in Sec. 4.3 we review the relevant simulation techniques necessary to obtain the liquid-liquid and liquid-solid phase diagrams. In Sec. 4.4 and 4.5 we present a discussion of our resulting phase diagrams and a brief conclusion, respectively.

4.2 Model

Using Monte Carlo simulations, Boström et al. [11] calculated the PMF, W_{MC}, between two macroions that mimic lysozyme molecules in an aqueous salt solution, by fixing the distance between the macroions and allowing the small salt ions to move. The calculation included contributions from the ion-ion, ion-macroion and macroion-macroion electrostatic interactions. In addition, they considered contributions from ion-ion and ion-macroion dispersion forces. The macroion-macroion van der Waals dispersion interaction was not included in the Monte Carlo calculation, but added separately. The concentration of the salts was held constant at 0.2 M. At this relatively large salt concentration, the Debye length is such that the electrostatic forces are strongly screened. Consequently, ion dispersion forces dominate the electrostatic forces in this regime. They repeated the simulation for different macroion separations and thus determined the PMFs for the three different salts. The solute particle was chosen to mimic properties of HEW lysozyme, i.e. it has a net charge of 10e and diameter of 3.3nm. The total interaction between two lysozyme molecules in the aqueous solution obtained in reference [11] is the sum of a hard core interaction,W_{HS}, the potential of mean force obtained from a Monte Carlo simulation, W_{MC}, and the protein-protein van der Waals (Hamaker) dispersion interaction, W_{vdW}, i.e.

$$W_{tot} = W_{HS} + W_{MC} + W_{vdW} \tag{4.1}$$

where

$$W_{vdW}(r) = -\frac{H}{12}(\frac{\sigma^2}{r^2-\sigma^2} + \frac{\sigma^2}{r^2} + 2\ln(1-\frac{\sigma^2}{r^2})), r > \sigma + 2\kappa \tag{4.2}$$

and

$$W_{vdW}(r) = W_{vdW}(\sigma + 2\kappa), \sigma < r \leq \sigma + 2\kappa. \tag{4.3}$$

The hard sphere potential is infinite for $r < \sigma$ and zero otherwise. The potential W_{MC} is set to zero for $r > 1.3\sigma$. The lysozyme-lysozyme dispersion interaction assumes a hydration-layer thickness of $\kappa = 1.5\mathring{A}$ and a Hamaker constant of $H = 10kT_0$ where $T_0 = 298K$. In addition, the total potential is assumed to be temperature independent for the range of temperatures that we study [11]. In Fig. 4.1, we have plotted the total potential, W_{tot}. We note that the model of Boström et al. has two discontinuities, as shown in Fig. 4.1. The first originates from the discontinuity intrinsic to W_{vdW} at $r = 1.0909\sigma$. Bostrom et al. refer to reference [20] who argue that since the dispersion potential is based on a continuum approximation for the solvent that is invalid for surface-to-surface separations on the order of a solvent diameter, the hydration layer thickness κ determines the limit of validity of the van der Waals interaction. This is the reason for the cut-off used for W_{vdW}. The reason for introducing the second cutoff in W_{MC} at $r = 1.3\sigma$ is simply that this potential is essentially zero beyond this point. We also note that it is possible that a different model, obtained by a different approximation for W_{vdW} at $r = 1.0909\sigma$ could have an effect on the phase diagram, but this is beyond the scope of our current study.

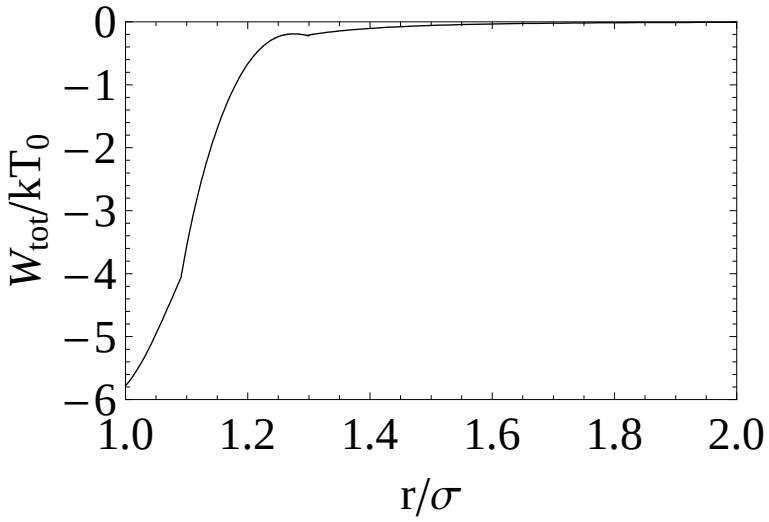


Figure 4.1: Total lysozyme potential with the 0.2 M NaSCN electrolyte.

4.3 Simulation Techniques

All of our Monte Carlo simulations for W_{tot} were conducted for a system of 512 particles in cubic boxes subject to periodic boundary conditions. The same number of Monte Carlo steps were performed for both equilibration and production, although the total number varied depending on the type of simulation. For all simulations, we set σ=1 and so the subsequent equations containing terms in ρ are to be interpreted as the reduced number density i.e. $\tilde{\rho} = \rho\sigma^3$ with σ=1.

4.3.1 Fluid-Fluid Coexistence

We used the Gibbs Ensemble Monte Carlo method [33, 84] to obtain the fluid-fluid coexistence curve. This method avoids problems associated with the formation of an

interface between the dense and dilute fluid phases. For a more detailed description of this method, please refer to 2.

On average, we chose the ratio of particle displacements to volume moves to be 512:1; the frequency of particle transfers was chosen to give reasonable acceptance rates of approximately 1-5$\%$. The equilibrium and production run times were at least one billion Monte Carlo steps (MCS) each, with a MCS being an attempt at one of three possible moves: particle displacement, volume change or particle exchange.

4.3.2 Fluid-Solid Coexistence

Fluid-solid coexistence curves can often be determined via the Gibbs-Duhem method [58, 59]. This method involves integrating the first-order Clausius-Clapeyron equation

$$\frac{dP}{d\beta} = -\frac{\Delta h}{\beta \Delta v} \tag{4.4}$$

where P is the pressure and $\beta = 1/kT$. Δ indicates a difference between the two coexisting phases, i.e. liquid and solid phases in this case. Thus Δh and Δv are the differences in the molar enthalpies and molar volumes, respectively, of the two phases. One caveat to this approach is that it requires the knowledge of an initial coexistence point on the $\beta P - \beta\mu$ plane, see Fig. 4.4 for example. Consequently, we carried out a series of NPT simulations along an isotherm to determine the equation of state for both the fluid and solid phases. We show in Fig. 4.2 our results for the liquid and solid

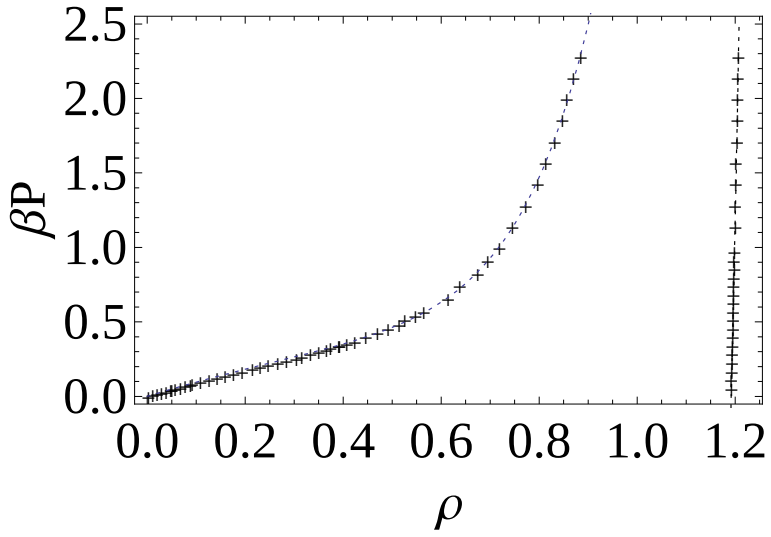


Figure 4.2: Liquid and solid isotherms at $T/T_0 = 3.5$. '+' are the Monte Carlo simulation results and the dotted curves are the fits to the data.

isotherms at a particular temperature. The equilibrium and production times for each NPT simulation were taken to be equal and at least 400 million MCS.

The isotherms were then fitted to the following forms:

$$\beta P = \frac{\rho}{(1-a\rho)} + b(\frac{\rho}{1-a\rho})^2 + c(\frac{\rho}{1-a\rho})^3 \qquad \text{(Liquid)} \tag{4.5}$$

$$\beta P = a\rho^2 + b\rho + c \qquad \text{(Solid)} \tag{4.6}$$

where ρ is the number density. Table 4.1 lists the fitting parameters for the investigate temperature. Equations (4.5) and (4.6) are integrated to yield free energy for the

corresponding state, and since

$$\beta\mu = \beta f + \beta\frac{P}{\rho} \tag{4.7}$$

we can obtain the equations for the chemical potential:

$$\beta\mu_l = \ln(\frac{\rho\Lambda^2}{1-a\rho}) + \frac{b/a - c/a^2 + 1}{1-a\rho} + \frac{c/2a^2 + b\rho}{(1-a\rho)^2} + \frac{c\rho^2}{(1-a\rho)^3} - (b/a - c/2a^2 + 1) \tag{4.8}$$

$$\beta\mu_s = 2a\rho + b(\ln\rho + 1) - (a\rho^* + b\ln\rho^* - c/\rho^*) + \beta f^{ex}(\rho^*) + \ln(\Lambda^2\rho^*) - 1 \tag{4.9}$$

where $\Lambda = \sqrt{h^2/2\pi kT}$ is the thermal de Broglie wavelength. The value of Λ plays no role in the location of phase equilibria for classical systems. Table I shows the parameters that best fit our Monte Carlo data for the liquid and solid isotherms for the two salts.

Table 4.1: Best fit parameters for isotherms at $\frac{T}{T_0} = 3.5$.

Isotherm	a	b	c
Liquid	0.5008	-0.9942	0.8016
Solid	1371.90	-3136.56	1789.48

The ρ^* in equation (4.9) is a result of the integration and denotes a reference state whose free energy must be predetermined from a series of independent simulations. To calculate this, we use the Frenkel-Ladd method [32] to harmonically couple lysozyme

particles to a lattice, i.e. an Einstein crystal. The potential energy of this system is

$$W(\lambda) = W_{tot} + \lambda \sum_{i=1}^{N} (\overrightarrow{r}_i - \overrightarrow{r}_{0,i})^2 \tag{4.10}$$

where $\overrightarrow{r}_{0,i}$ is the position of the lattice site to which particle i is coupled, $\overrightarrow{r}_i$ is the position of the particle, and λ is the coupling parameter. The free energy of the lysozyme system is then

$$F_{Lys} = F_{\lambda_{max}} - \int_0^{\lambda_{max}} d\lambda \langle W(r,\lambda) \rangle_\lambda = F_{\lambda_{max}} - \int_0^{\lambda_{max}} d\lambda \langle \sum_{i=1}^{N} (\overrightarrow{r}_i - \overrightarrow{r}_{0,i})^2 \rangle_\lambda \tag{4.11}$$

At sufficiently high values of λ_{max}, i.e. the coupling is sufficiently strong, the system behaves as a non-interacting Einstein crystal, the free energy of which can be calculated exactly. We can then obtain F_{Lys} via thermodynamic integration along a reversible path. The mean squared displacement of particles relative to their lattice positions is calculated by simulation in a system with a fixed center of mass. In Fig. 4.3 we show the relative mean squared displacement as a function of the coupling parameter. It can be seen that for sufficiently large λ, the system behaves as an Einstein lattice and thus the reversible path has been established.

Once the chemical potentials of both phases are obtained at the same temperature, we obtain the coexistence points by equating the chemical potential and the pressure for the two phases (Fig. 4.4). We denote the coexisting temperature and pressure to be T_1 and P_1, respectively. We then use the Gibbs-Duhem method to generate the entire coexistence curve. A simple predictor-corrector algorithm was used for the integration.

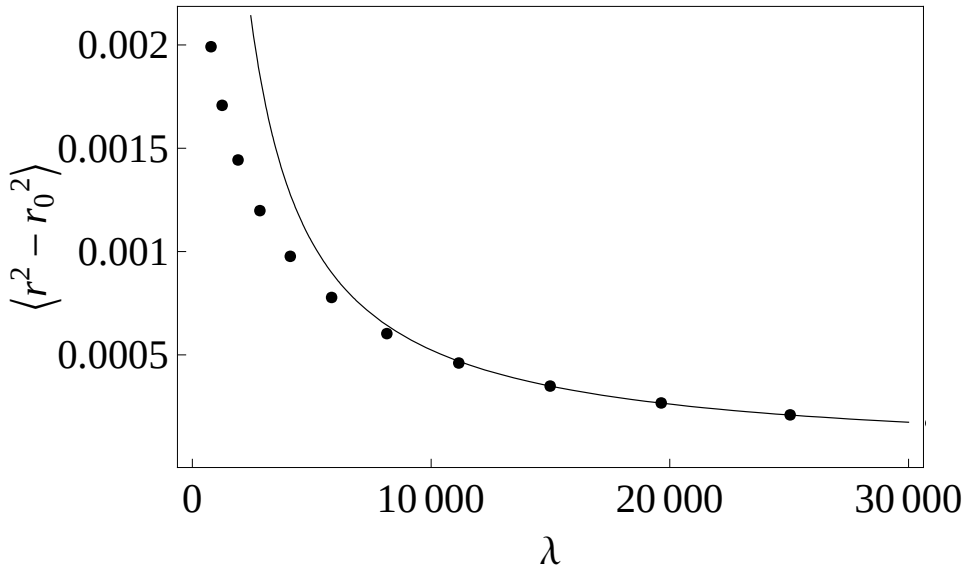


Figure 4.3: Monte Carlo data of the mean squared displacements for the coupled solid (dots) compared with that of an Einstein lattice(solid line). To achieve deviations of less than 1% with the Einstein lattice, a λ_{max} of 30,000 was required.

The basic idea is as follows. Since h and v at (T_1, P_1) can be obtained conveniently from our previous simulations for the coexisting densities, equation (4.4) can then be used to estimate the coexisting pressure $P_{2,est}$ for the next temperature T_2 (prediction). Next, two NPT simulations are executed in parallel at (T_2, $P_{2,est}$) and we obtain another set of h and v values. By taking the average of the two sets of h's and v's, we obtain a more accurate estimate for P_2 (correction). Finally, two new NPT simulations at (T_2, P_2) are carried out to give the coexisting densities at T_2. This process is repeated until the entire fluid-solid coexistence curve is obtained.

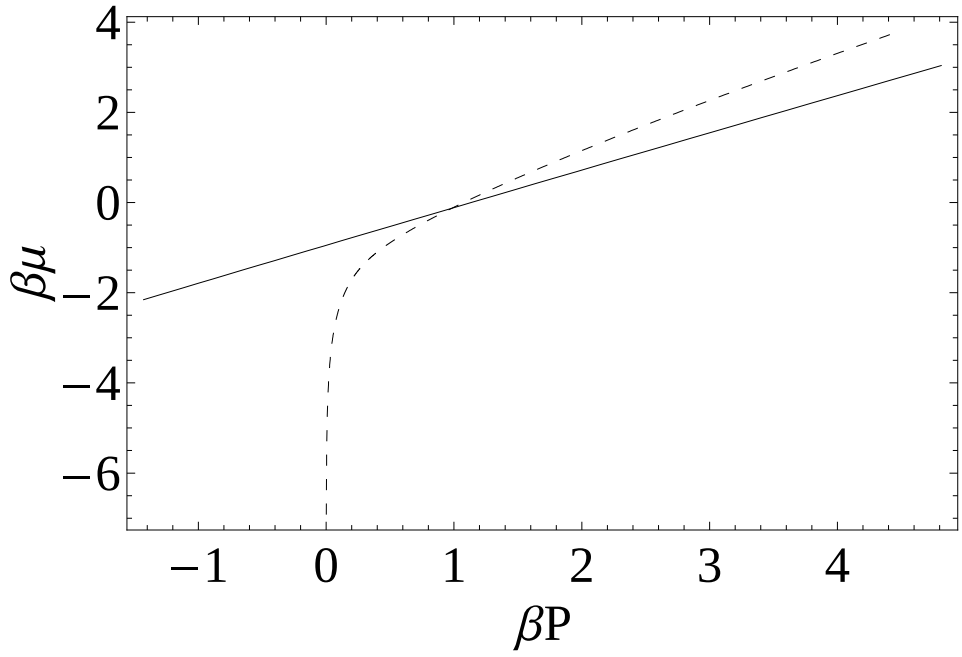


Figure 4.4: $\beta P - \beta\mu$ plot at $\frac{T}{T_0} = 3.5$. Dashed line for liquid; solid line for solid.

4.4 Results

Our Monte Carlo results yield a metastable fluid-fluid phase (Fig. 4.5(a)). This is not surprising since the range of attraction is small with respect to the particle diameter. It is known in the case of square well fluids that the threshold for metastability begins for ranges less than about 1.25σ [83]. Though the potentials we study are quite different than square wells, one can make a comparison following a treatment by Noro and Frenkel [81], in which the effective range of a potential is estimated by equating the reduced second virial coefficients, ${B_2}^*$, of a square well system with the system in question. This yields an effective square well range of approximately 1.13σ, which falls

within the region of metastability for square well fluids [83]. Thus, our Monte Carlo prediction of a metastable fluid-fluid curve is consistent with the estimate of Noro and Frenkel. (In general, this effective range is temperature dependent; however, the variation of $B_2{}^*$ in the region of interest is small.) Another measure of the metastability of the phase separation curve is the so-called metastability gap, defined as $(T_L - T_c)/T_c$. We find that for our model this gap is approximately 18%, which is much bigger than the 5% estimated from perturbation theory (Fig. 4.5(b)).

Estimates of the critical points for our finite system were obtained by fitting the fluid-fluid coexistence data to the following equations

$$\frac{\rho_l + \rho_g}{2} \simeq \rho_c + A|T - T_c| \tag{4.12}$$

$$\rho_l - \rho_g \simeq B|T - T_c|^\beta \tag{4.13}$$

where T_c and ρ_c are the critical temperature and density, respectively, and $\beta \simeq 0.326$ is the 3D-Ising critical exponent. Finite size effects would have to be taken into account to obtain the critical point parameters for the infinite system. Table 4.2 contains a summary of the critical parameters and fitting parameters the our investigated system.

Table 4.2: Critical parameters for the fluid-fluid coexistence curve.

T_c/T_0	ρ_c	A	B	$B_2{}^*$
2.636	0.395	0.48	1.40	-1.40

In addition, we have calculated the reduced second virial coefficients at the critical

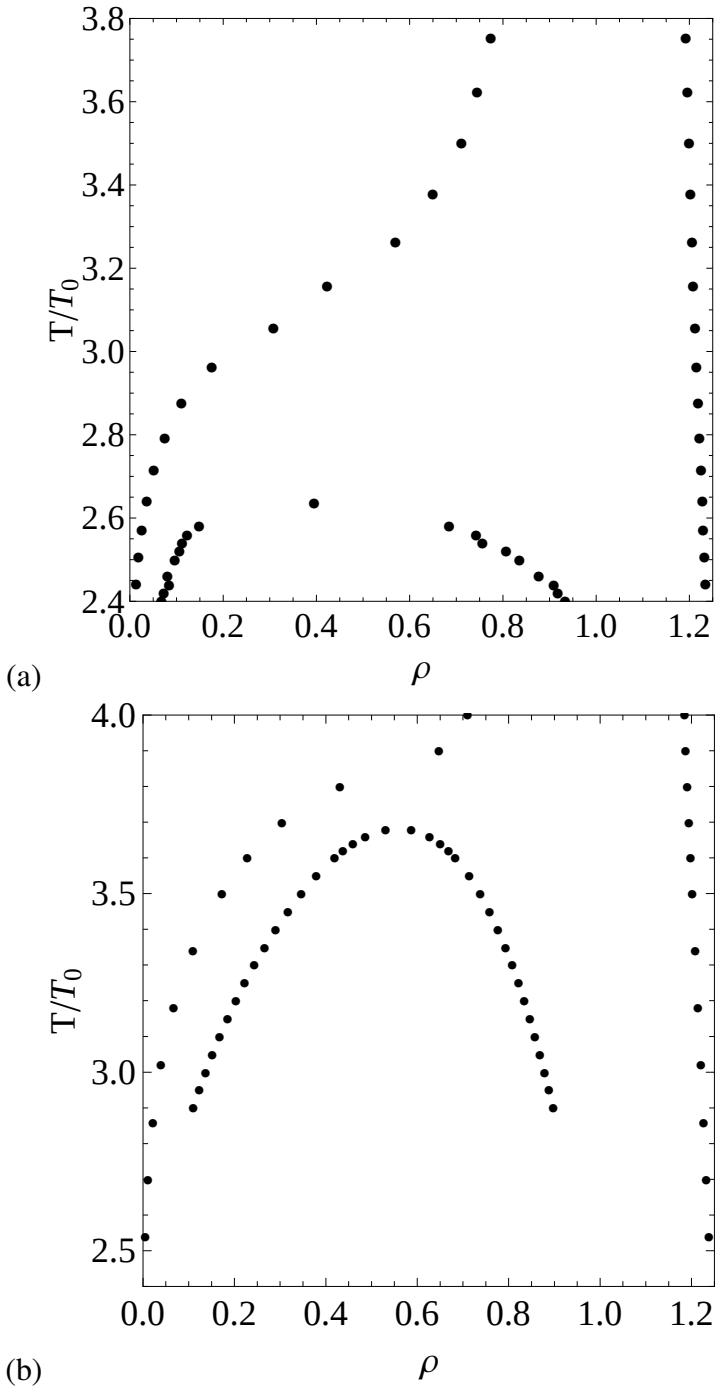


Figure 4.5: Phase diagram curve obtained from (a) Monte Carlo simulations (b)first-order perturbation theory. The metastability gaps $(T_L - T_c)/T_c$ are approximately 12% and 5%, respectively.

temperature,

$$B_2{}^* \equiv B_2/B_{2HS} = 1 + 3\int_1^\infty s^2(1 - e^{-\beta W_{tot}(s)})ds \tag{4.14}$$

where $s \equiv r/\sigma$, for each system. We find that $B_2{}^*$ is small and negative, consistent with experimental observations for systems that undergo metastable fluid-fluid transitions.

4.5 Conclusion

Our predicted phase diagram for NaSCN lysozyme electrolyte solution has been obtained using standard Monte Carlo techniques. It is clear that the model we study is an improvement over earlier models of lysozyme in that it can account at least qualitatively for the Hofmeister effect. We find that our results are rather different than those predicted by Boström et al. as one might expect. In contrast to their predictions using first order perturbation theory, our results show a larger metastability gap than obtained from the perturbation theory; the Monte Carlo results yield a gap of 18%.

It is possible that the potential of mean force calculated in reference [11] needs to be improved. For example, the model for the protein could be improved to take into account a more realistic description of the amino acid charge distribution on the protein surface. Another effect that might need to be investigated is the effect of the buffer on the potential of mean force. The buffer is usually added to obtain the right pH and otherwise is assumed to have no further influence, but it is conceivable that there could be large buffer effects on the potential of mean force [106]. Also, as discussed in

Chapter 3, another recent development on the possible causes of the Hofmeister effect is the hydrophobic surface forces; we will study a model with such an origin in Chapter 5.

Further, it is possible that isotropic models such as these (i.e. models that are independent of macromolecule orientation) cannot account for such quantitative features as the breadth of the coexistence curve and that one must take into account the effects of anisotropy [55, 104, 28] on the interactions that can arise from a variety of sources, including that of water.

Chapter 5

Ion-Specific Effects on Phase Transitions in Protein Electrolytes due to Hydrophobic Surface Forces

5.1 Introduction

Chapter 3 summarizes some of the recent progress in the understanding of hydrophobic surface forces. In this chapter we concentrate on the role of such forces on phase transitions in protein electrolyte solutions, because the phase diagram is an important property for protein solutions (see Chapter 1). It has been shown for a significant number of proteins that optimal crystal nucleation tends to occur when the solution is prepared in the vicinity of a metastable critical point of a protein-poor, protein rich fluid-fluid phase

separation curve[36, 95, 109].

Sec. 3.2.2 describes briefly one of the most recent applications of molecular dynamics simulations by Lund et al. [70], where the authors obtained the PMFs between lysozyme molecules in electrolyte solutions with different types of anions 3.7. It is thus of interest to know the corresponding phase diagrams of these PMFs. In this chapter we present Monte Carlo simulations of the phase diagrams for the $0.2M$ NaI and the $0.3M$ NaCl electrolyte solutions considered in reference [70]. We present in Sec. 5.2 a summary of the model and our simulation details. We give our results in Sec 5.3 and conclude briefly in Sec. 5.4.

5.2 Model and Methods

5.2.1 Model

The model of lysozyme in aqueous salt solution model, as given by Lund et al.[70], consists of the following: each amino acid on the protein is represented as a soft charge-neutral sphere, located at the residue center of mass given by X-ray structure $4LZT$ in the protein data bank. In addition, the protonation sites of all titratable groups are included at their original positions and their corresponding electrostatic charges are set for a pH of 4.7. The rigid protein molecules are allowed to rotate and translate in their MC simulations, while mobile salt and counter ions are explicitly included as soft spheres.

The solvent is treated as a dielectric continuum and solvent structural effects (hydrophobicity) are **implicitly** accounted for. Specifically, the interaction energy between the ions and the nearest hydrophobic residues, $V_{sp}(r_{ij})$, is based on an empirical potential, from results obtained from MD simulations of ions in the presence of an air/water interface [46, 22]. The expression for the total interaction energy, from which the angular averaged potential of mean force (PMF) was calculated, is given as

$$\beta U = \sum \beta V_{sp}(r_{ij}) + \sum \frac{l_B z_i z_j}{r_{ij}} + 4\epsilon_{LJ}[(\frac{\sigma_{ij}}{r_{ij}})^{12} - (\frac{\sigma_{ij}}{r_{ij}})^{6}] \tag{5.1}$$

where $l_B = 7.1\mathring{A}$ is the Bjerrum length, r_{ij} is the distance between particles i and j, z is their charge number and ϵ_{LJ} and σ_{ij} are the Lennard-Jones parameters. From the above expression for βU, Lund et al. used MC simulations to calculate the angular averaged PMF, $W(r)$, between the lysozyme molecules for various aqueous electrolyte solutions. With their PMF data, we fit these potentials for the following systems: $0.3M$ NaCl and $0.2M$ NaI, as shown in Fig. 5.1. It is important to note that the simulations carried out by Lund et al. were conducted at $T = 298K \equiv T_0$. We use these potentials for the range of temperatures considered in this chapter. For each model, we have defined the corresponding value of σ to be the smallest value of r at which the potential crosses $W = 0$. For the two models examined ($0.3M$ NaCl and $0.2M$ NaI), these values are nearly identical and are equal to $28.84\mathring{A}$ and $28.88\mathring{A}$ respectively. Therefore, for the remainder of the chapter, σ is to be interpreted as the σ for the corresponding model being referenced. In addition, the potentials have been set equal to 0 for values of r/σ

greater than 2.06 and 2.02, respectively.

5.2.2 Methods

Using this PMF, we perform MC simulations in order to determine the corresponding phase diagrams and pair correlation functions. Our systems consist of N=500 particles in cubic simulation cells subject to periodic boundary conditions. The same number of MC cycles are performed for both equilibration and production, although the total number varies depending on the type of simulation. A single MC cycle is defined as N=500 MC steps where a step is a random choice from the usual repertoire of MC moves.

Fluid-Fluid coexistence

We use the Gibbs Ensemble MC method [84, 33] to obtain the equilibrium coexisting densities of the protein-poor and protein-rich fluid phases. (See Sec. 2.2 for more details.)

Fluid-Solid coexistence

Fluid-solid coexistence are obtained via the Gibbs-Duhem method. This method involves integrating the first-order Clausius-Clapeyron equation $\frac{dP}{d\beta} = -\frac{\Delta h}{\beta \Delta v}$ where P is the system pressure, $\beta = 1/kT$, Δ indicates a difference between the liquid and solid phases and h and v are the molar enthalpies and volumes respectively. One caveat to this approach is that it requires the knowledge of an initial coexistence point on the $\beta P - \beta \mu$

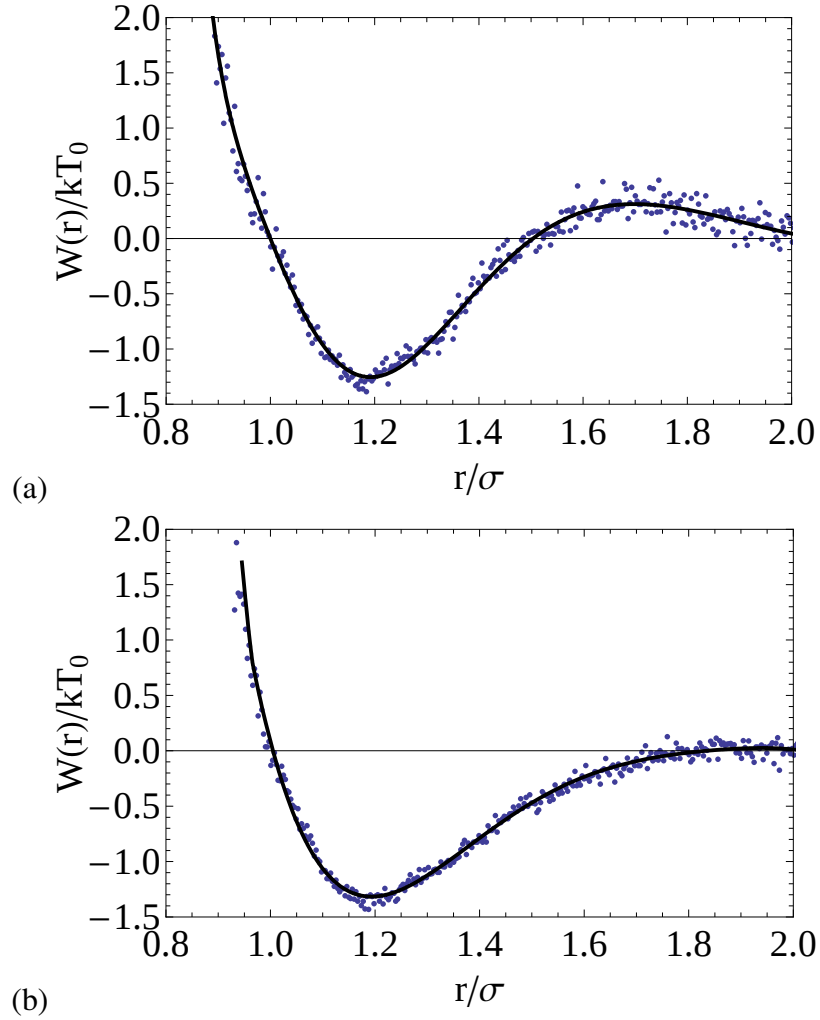


Figure 5.1: Total potentials for the (a) 0.3M NaCl (b) 0.2M NaI electrolyte systems. Solid line is the fitted polynomial and dots are data obtained from MC simulations.

plane. Consequently, we carry out a series of NPT simulations along an isotherm to determine the equation of state for both the fluid and solid phases. The equilibrium and production times for each NPT simulation are taken to be equal and at least $2 * 10^5$ MC cycles. Each isotherm requires a minimum of 50 data points to obtain accurate fits. Once the equations of state are obtained, they are fit to the following form for the liquid $\beta P_{Liq} = \sum_{i=1}^{m} c_i(\frac{\rho}{1-a\rho})^i$ and $\beta P_{Sol} = \sum_{i=0}^{4} c_i\rho^i$ for the solid, where the a, c_i and m are distinct for each isotherm examined and chosen to best fit the data (Whereas in other studies, one typically use m=3, we find it necessary to increase it to 5 or 6 in cases studied here.). Integration of the equations of state will yield the free energies and chemical potentials for the liquid and solid. However, as a result of the integration, one must know the free energy of the solid at a particular reference density along the solid isotherm. To calculate this free energy, we use the Frenkel-Ladd method for soft-core continuous potentials [32] to harmonically couple the particles to lattice sites. With the free energy of the solid at the reference state known, straightforward integration produces the expressions for the corresponding chemical potentials and thus the initial coexistence points are determined via the conditions for mechanical and chemical coexistence in equilibrium, i.e. $P_{Liq}(\rho_{Liq}) = P_{Sol}(\rho_{Sol})$ and $\mu_{Liq}(\rho_{Liq}) = \mu_{Sol}(\rho_{Sol})$ where ρ_{Liq} and ρ_{Sol} are the coexisting liquid and solid densities.

Accurate determination of T_c

It is known that systems with short-range attractive interactions ($< 1.25\sigma$) give rise to liquid-liquid phases separations that are metastable with respect to the solubility curve[83], i.e., freezing preempts fluid-fluid phase separation. Choosing as an initial state a position near a metastable fluid-fluid critical point is desirable for experimentalists trying to grow high quality protein crystals from solutions as nucleation rates reach a maximum in that region [109]. An important observed characteristic of metstable fluids is their small and negative second virial coefficients B_2 first noted by George and Wilson[36]. As will be discussed in more detail in our results, the phase diagram for the 0.3M NaCl system is only very slightly metastable as a consequence of an additional repulsive maximum in the potential. This is important because the system would otherwise exhibit a stable fluid-fluid transition without the addition of the repulsive maximum. Therefore in an effort to substantiate that this system is indeed metastable, an accurate estimate of the critical temperature is determined by the Bruce-Wilding finite-size scaling method [122]. The location of the critical point can be obtained by matching the probability distribution of the ordering operator $M = \frac{\rho - su}{1 - sr}$ with the universal distribution characterizing the Ising class. The number density and energy density are defined by $\rho = L^{-d}N$ and $u = L^{-d}U$, respectively, with U the total energy of the system, d the dimension of the system. To obtain the value of $T_c(L)$ for a given simulation cell length L, we run a series of Grand Canonical Ensemble simulations and "tune" the values of

chemical potential, temperature and s until the probability distribution of the ordering operator $P(M)$ collapses onto the universal $P^*(M)$ for the Ising model. When good estimates of the tuning parameters are obtained, we perform longer runs of $2 * 10^5$ MC cycles to collect accurate statistics followed by a histogram reweighting procedure to obtain accurate values of the tuning parameters at criticality. This procedure is repeated for increasing values of L and then extrapolated to the limit $L = \infty$ to determine the critical temperature of the infinite system. A detailed discussion on this procedure can be found in Li et al. [65] or Chapter 6.

5.3 Results

We have determined the complete phase diagrams for two different aqueous solutions of lysozyme, 0.3 M NaCl and 0.2 M NaI shown in Figs. 5.3 [1] and 5.4 respectively. In the case of 0.3 M NaCl, we find that there is a metastable fluid-fluid coexistence curve, although the metastability gap (defined as $(T_L - T_c)/T_c$, where T_c denotes the critical temperature for the finite system, and T_L denotes the temperature on the solid curve that corresponds to the critical density) is very small. The situation for the 0.3 M NaCl solution is a little tricky, since the solid branch of the solid-liquid coexistence curve almost touches the fluid-fluid curve. In order to determine the critical point for the

[1] The Gibbs Ensemble simulations and NPT simulations were done by my colleague Steven Lettieri; this joint work was published in [64].

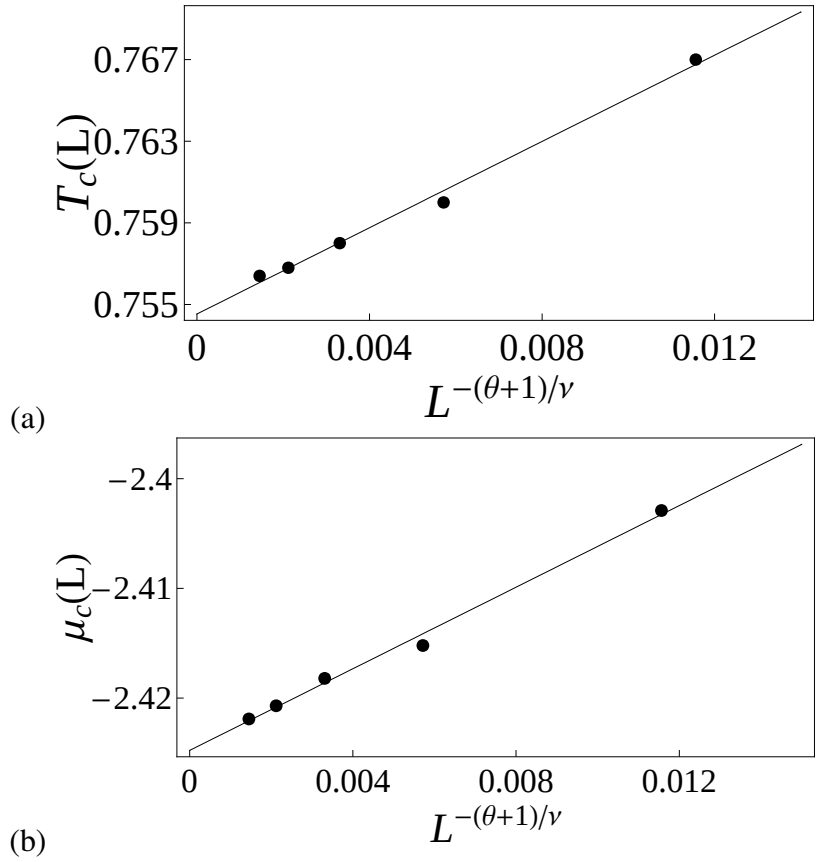


Figure 5.2: FSS results for (a) $T_c(L)$ and (b) $\mu_c(L)$ as a function of $L^{-(\theta+1)/\nu}$ for the 0.3M NaCl electrolyte solution. ν is the critical exponent for the correlation length and θ is the universal correction to scaling exponent. For the 3D Ising universality class, $\nu = 0.629$ and $\beta = 0.326$. By extrapolating to infinite volume ($L \to \infty$), we can obtain an estimate of the true bulk behavior: $T_c(\infty) \simeq 0.755 T_0$. For more details of FSS, see Ref. [65]

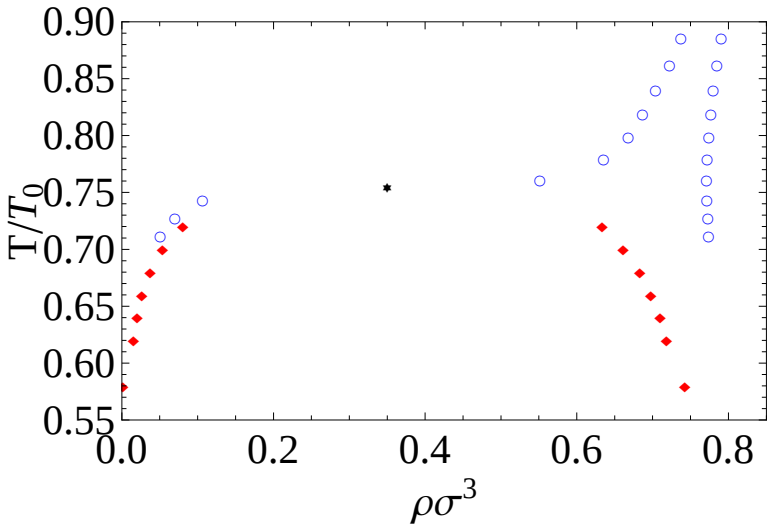


Figure 5.3: Phase diagram curve obtained from Monte Carlo simulations for the aqueous lysozyme solution with NaCl electrolyte at 0.3 M. The fluid-fluid separation curve is metstable. Open circles are the liquid-solid coexistence data and solid diamonds are the fluid-fluid coexistence data. The solid star is our estimate of the critical point for the infinite system as determined from finite size scaling.

infinite system, we employ the method of finite size scaling (FSS), discussed briefly in section 5.2.2 . Our results for $T_c(L)$ are shown in Fig. 5.2.2. (See the figure caption for more details.) The extrapolation $L \to \infty$ gives us a reliable estimate of the critical point, $T_c(\infty)$, for the bulk system. However, the NPT simulations we use to determine the solid-liquid curve are also subject to finite size effects and we are unable to extrapolate these to obtain their bulk limits. Therefore it is difficult to be precise about the magnitude of the metastability gap. Thus it would seem prudent to conclude that fluid-fluid critical point for 0.3 M NaCl is right on the edge of being metastable.

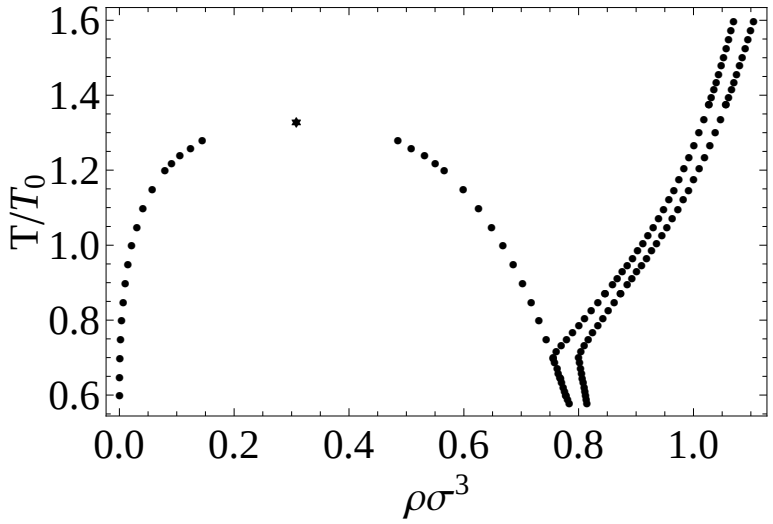


Figure 5.4: Phase diagram curve obtained from Monte Carlo simulations for the aqueous lysozyme solution with NaI electrolyte at 0.2M. The fluid-fluid separation curve is stable. Solid circles are simulation data and star is our estimate of the critical point as determined by a rectilinear diameter fit. Note that the data for liquid line overlaps the data from the dense fluid phase.

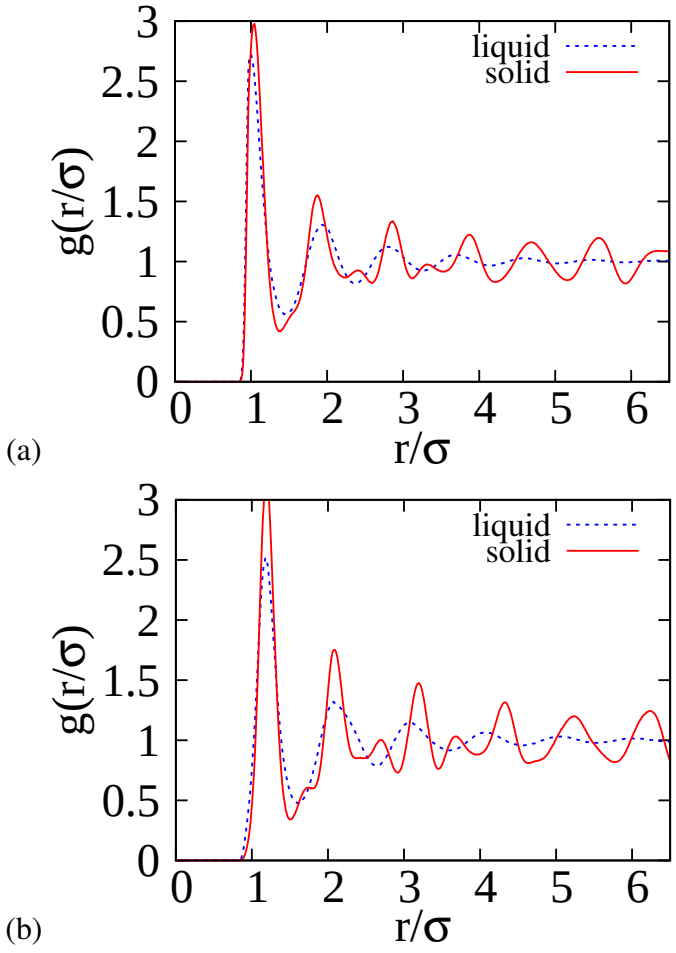


Figure 5.5: Plot of the liquid and solid pair correlation functions corresponding to coexisting liquid and solid states for (a) 0.2M NaI at $T = 1.6T_0, P = 20.409\sigma^3/kT_0, \rho_{Liq}\sigma^3 = 1.069, \rho_{Sol}\sigma^3 = 1.104$ and (b) 0.3M NaCl at $T = 0.91T_0, P = 2.002\sigma^3/kT_0, \rho_{Liq}\sigma^3 = 0.754, \rho_{Sol}\sigma^3 = 0.798$.

For the 0.2M NaI solutions, we obtain estimates of the critical points by fitting the fluid-fluid coexistence data to the following standard rectilinear equations

$$\frac{\rho_l + \rho_g}{2} \simeq \rho_c + A|T - T_c| \tag{5.2}$$

$$\rho_l - \rho_g \simeq B|T - T_c|^\beta \tag{5.3}$$

where T_c and ρ_c are the critical temperature and density, respectively, and $\beta \simeq 0.326$ is the 3D-Ising critical exponent. Finite size effects would have to be taken into account to obtain the critical point parameters for the infinite system. In the case of 0.2M NaI (Fig. 5.4), we estimate the triple point temperature to be around 0.7 T_0. We are not able to make direct comparisons between simulation results and experimental data for either salt, however, since to the best of our knowledge, no experimental data exist for the molarities studied in this chapter.

It is also interesting to note that for the stable phase diagram (Fig. 5.4), there is a metastable continuation of the liquidus curve along the high density branch of the fluid-fluid coexistence curve below the triple point, T_{tp}. Namely, as we continue our simulation of the coexisting liquid phase in the liquidus line below T_{tp}, this becomes the metastable dense liquid phase we have obtained by our gibbs ensemble method.

Figure 5.5 plots the pair correlation functions of the liquid and solid at conditions corresponding to phase coexistence for the 0.2M NaI and 0.3M NaCl lysozyme solutions, respectively. In order to show that the solid does indeed exhibit long range order, we ran simulations of N=4000 particles to probe larger distances. It is clear that both

liquid and solid correlation functions display an oscillatory behavior. The reason that it does so for the liquid phase is due to its high density. Note that in Fig. 5.4 the separation between the liquid and solid coexistence densities is very small. However, the correlation functions for the solid still shows a strong peak at the largest distances, suggesting a crystal structure, while it already decays to 1 for the liquid phase after a few (~ 4.5) σs.

One can see from the phase diagrams of Figs. 5.3 and 5.4 that the details of the corresponding potentials (Figs. 5.1(b) and 5.1(c)) are important in determining the phase diagram. Although the attractive wells of their potentials are similar in both the width [120] and the depth, their phase diagrams are very much different. The 0.3M NaCl solution has a metastable fluid-fluid coexistence curve while the 0.2M NaI solution has a stable phase separation curve. This can be largely attributed to the fact that the potential for the 0.3M NaCl has a repulsive region which reduces the effective range of the attractive interaction. In other words, the critical point of the fluid-fluid coexistence curve is driven to a lower temperature by the additional positive extremum in Fig. 5.1(b). This behavior was also observed by Brandon et al. [14], in their study of models with multiple extrema. They argued that for more complicated potentials than those with a single extremum, the effective range of attraction defined by Noro and Frenkel [81] was more useful in characterizing the phase diagrams than, say, the width of the attractive well. Noro and Frenkel [81] developed an extended law of corresponding states, in

which they introduced an energy scale (the depth of the attractive well), an effective hard core σ_{eff} and a range R. To do this for systems whose potentials are continuous, one divides the potential into attractive and repulsive terms, v_{att} and v_{rep}, respectively, and defines an "equivalent" hard-core diameter for the repulsive part of the potential using an expression suggested by Barker and Henderson[6]:

$$\sigma_{eff} = \int_0^\infty dr[1 - \exp(-v_{rep}/kT)]. \tag{5.4}$$

The reduced second virial coefficient is then defined as $B_2^* = B_2/(\frac{2\pi\sigma_{eff}^3}{3})$. One then defines an effective range R of the attractive interaction by equating B_2^* of a square well system with that of the system in question. (Note that the range of the attractive interaction for a square well system is defined unambiguously, whereas this is not the case for other models.) Although this range is temperature dependent, it provides a useful length scale for models such as those that have been used in colloidal and protein solutions. The value of this reduced second virial coefficient at the critical point has been found to be relatively constant for a wide range of models that are commonly used to describe phase transitions, ranging from extremely narrow attractive wells (Baxter's adhesive hard sphere model) to the van der Waals limit of infinitely long-range attractive wells[81]. These values are in the range $-2.36 \leq B_2^*(T_c) \leq -1.33$. We show the reduced second virial coefficient $B_2^*(T_c)$, the effective hard core diameter σ_{eff} and the range R for both potentials studied here in Table 5.1. All our values for $B_2^*(T_c)$ are in the same range as for the models cited in Ref. [81]. Noro and Frenkel also estimated that

the fluid-fluid transition became metastable with respect to freezing when $R = 0.14$, consistent with a variety of models that had been studied at that time. Subsequently, however, it was shown that for the square well model $R \simeq 0.25$[83]. This latter value has been proposed based on a simple van der Waals model for both the fluid and the solid phase[21] and by a phenomenological argument using a cell model for the solid[3]. If we include the region of repulsive interaction associated with the secondary maximum in our calculation of the effective hard core diameter, we find that the range for the 0.3 M NaCl system that is slightly metastable is $R \simeq 0.20$.

Finally, we note that we have also run preliminary NPT simulations for the 0.3M NaI solution. However, no phase diagram was calculated due to the fact that the difference in density between the liquid and solid isotherms is extremely small even when the pressure is sufficiently high. In addition, at higher pressures, the density on the liquid isotherm has large fluctuations about its average; in fact, it typically transitions from the liquid phase to the solid phase where it remains stuck for the remainder of the simulation. Therefore, since we are unable to distinguish sufficiently accurately between the liquid and solid phases, we are unable to perform an accurate calculation of the 0.3M NaI phase diagram by this method.

Table 5.1: Parameters of interest at T_c.

System	T_c	σ_{eff}	$B_2^*(T = T_c)$	R
0.2M NaI	1.33 T_0	0.961	-2.18	0.423
0.3M NaCl	0.757 T_0	1.069	-2.19	0.205

5.4 Conclusion

We have studied models of two electrolyte solutions of lysozyme and demonstrated the effects of hydrophobic surface forces on the phase diagram of lysozyme. Although the molarities studied are too small to see a significant metastability gap, the 0.3 M NaCl solution does have a slightly metastable fluid-fluid critical point. Interestingly, the small range R associated with this is produced by the effect of a repulsive interaction associated with a secondary extremum. In the absence of that repulsive region the system would have a stable fluid-fluid transition. This is another example of a phenomenon first studied by Brandon et al. [14]. It is not clear what the physical origin of the secondary maximum is for the model of Lund et al. [70], but Brandon et al. [14] attribute their secondary maximum to the effect of water restructuring near the solute particles. It would be interesting to have a better understanding of its origin for the current model.

At this moment we do not know which of the two different models we have studied (ion-dispersion forces in Chapter 4 and hydrophobic surface forces in Chapter 5) is more

accurate, although they give rise to two rather different phase diagrams for the lysozyme solution in NaCl electrolyte, as investigated in Refs. [63] and [64]. The reason is that we are unable to compare the results of these studies with any experimental results for lysozyme since no experimental data exists to our knowledge. It would seem likely that further developments will include both ion-dispersion effects discussed by Boström et al. [11] and the hydrophobic surface forces discussed in this chapter to reach a more complete understanding of the Hofmeister effect.

Chapter 6

Phase Diagram of a Model of Nanoparticles in Electrolyte Solutions Including Ion Dispersion Effects

6.1 Introduction

Controlling interactions between nanoparticles in aqueous electrolyte solutions is important in a wide range of fields, including process design in nanotechnology [56, 76], ceramic processing [43, 94] and crystallization of proteins [41, 114]. Salts have commonly been used as a means to tune these interactions in electrolyte solutions. It is known that not only the salt concentration but also the salt type is important in such cases, particularly at salt concentrations of the order of 0.1M or greater. As aforemen-

tioned, the dependence on salt type is known as the Hofmeister effect, which has been the subject of ongoing theoretical study [12, 41, 60].

Ion-dispersion forces between salt ions and solute particles had been assumed to be weak and consequently neglected in earlier theoretical studies (DLVO theory). However, a recent study by Ninham and Yaminsky [80] demonstrated that such forces can at least provide a partial explanation for the Hofmeister effect. This work has motivated a series of studies showing the important role these forces can play in protein crystallization [41, 13, 11, 63]. Thus, it is important to understand how the ionic dispersion forces affect the phase behavior of nanoparticle solutions, in order to control more precisely the conditions of these solutions.

A recent model described by Deniz et al. [25] provides interesting results on the role of salt in nanoparticle solutions. In their paper a model of aluminum oxide nanoparticles is proposed that includes the ion-dispersion forces between the nanoparticles and salt ions. The authors chose aluminum oxide (Al_2O_3) for study, in part because of its commercial importance. (Aluminium oxide is one of the most versatile ceramic oxides and has been used in a wide range of applications in electrical, engineering and biomedical areas.) It has also been suggested [50] that monovalent salt ions in electrolyte solutions provide a useful method for flocculation in ceramic processing, although this has yet to be realized. To determine the effects of the salt ions on solutions of aluminum oxide particles, the potentials of mean force were obtained using an integral-equation

approach. Namely, Deniz et al. [25] used the Ornstein-Zernike equation with the well known hypernetted chain closure approximation (OZ-HNC) to determine the effective interactions between the nanoparticles in electrolyte solutions. They then determined the phase diagram of aluminum oxide particles in solution using a first-order thermodynamic perturbation theory. Their work appears to be an important step forward in understanding the effect of salt ions on the phase diagram of nanoparticles. However, the perturbation theory provides only a semi-quantitative description of the phase diagram. Because salt plays a crucial part in the phase diagrams of nanoparticles, in this chapter we extend the work of Deniz et al. to obtain accurate fluid-fluid coexistence curves for their model, in the case of 0.1M NaI. In particular, we use a combination of finite-size scaling (FSS) and multicanonical simulations to determine the critical point and subcritical behavior of their model. We supplement this work with Gibbs ensemble (GEMC) simulations of the subcritical coexistence curve. Together with the cases of NaCl and nonpolarizable salt described in [63], we show that, as expected, phase diagrams depend strongly on the types of added salt, i.e., the Hofmeister effect manifests itself in the phase coexistence curves for the different electrolyte solutions, as first shown in Refs. [11, 63, 25]. In addition, this model belongs to the universality class of the Ising model. We also determine the scaling fields and critical point parameters.

The remainder of the chapter is as follows: in Sec. 6.2 we summarize the model and review the relevant simulation techniques necessary to obtain the liquid-liquid phase

diagram. In Sec. 6.3 and 6.4 we present a discussion of our resulting phase diagram and a brief conclusion.

6.2 Model and Simulation Techniques

6.2.1 Model

The model of Al_2O_3 dispersed in an electrolyte solution that Deniz et al. consider consists of three interactions betwen the solute nanoparticles: a hard core interaction, U_{HS}, a potential of mean force, U_{HNC}, obtained using the hypernetted chain closure, and the usual attractive van der Waals interaction, U_{vdW}. We briefly summarize how the authors determine U_{HNC}. The nanoparticles are considered to be spherical particles of diameter σ and charge q. The monovalent salt ions are spherical counter- and co-ions with diameter σ_i and charge $\pm e$, where e is the charge on the electron. The solvent is treated as a continuum with a dielectric constant $\epsilon = 78.5$. For Al_2O_3 particles $\sigma = 2$ nm and $q = +4e$, while $\sigma_i = 0.4$ nm for solutions. The potentials of mean force, U_{HNC}, between the dilute nanoparticles are then calculated using the Ornstein-Zernike equations with the hypernetted chain closure approximation [25]. Spatial correlation functions for the cation-macroion, anion-macroion and macroion-macroion pair interactions are then determined through a solution of multicomponent OZ equations [34] combined with the

HNC closure relation:

$$h_{ij}(r_{ij}) = C_{ij}(r_{ij}) + \sum \rho_k \int C_{ik} h_{jk}(r_{jk}) d^3 r_k \tag{6.1}$$

with

$$C_{ij}(r_{ij}) = \frac{-u_{ij}(r_{ij})}{kT} + h_{ij}(r_{ij}) - lng_{ij}(r_{ij}) \tag{6.2}$$

where $h_{ij}(r_{ij}) = g_{ij}(r_{ij}) - 1$ is the total correlation function, $g_{ij}(r_{ij})$ is the radial distribution function, u_{ij} is the potential energy between species i and j and ρ_k is the average number density of species k. The total potential between the nanoparticles is then given by the result of this calculation, augmented by the standard attractive van der Waals dispersion interaction between two nanoparticles. Thus the interaction potential between the aluminum oxide particles in solution is taken to be

$$U = U_{HS} + U_{vdW} + U_{HNC} \tag{6.3}$$

where

$$U_{vdW}(r) = -\frac{H}{12}\left(\frac{\sigma^2}{r^2 - \sigma^2} + \frac{\sigma^2}{r^2} + 2\ln\left(1 - \frac{\sigma^2}{r^2}\right)\right), r > \sigma + 2\kappa \tag{6.4}$$

and

$$U_{vdW}(r) = U_{vdW}(\sigma + 2\kappa), \sigma < r \leq \sigma + 2\kappa. \tag{6.5}$$

The hard sphere potential is infinite for $r < \sigma$ and zero otherwise. The potential U_{HNC} is set to zero for $r > 2\sigma$. The ion dispersion interaction assumes a hydration-layer thickness of $\kappa = 1.5\mathring{A}$ and a Hamaker constant of $H \approx 13kT_0$ where $T_0 = 298K$. The

total potential is cut off at $r = 2\sigma$ since it is essentially zero beyond this point. The total potential obtained here is assumed to be temperature independent for the range of temperatures that we study, although the dielectric constant has a weak dependence on temperature [11].

6.2.2 Simulation Techniques

Finite-Size Scaling (FSS)

To study the critical region of the phase diagram, we perform grand canonical Monte Carlo (GCMC) simulations [2], and use the Bruce-Wilding finite-size scaling method [122, 15], together with histogram-reweighting techniques [30] for further analysis. The location of the critical point can be obtained by matching the probability distribution function (PDF) of the ordering operator $\mathcal{M}$ with the universal distribution function characterizing the Ising class. The reason we can do so is that systems with short-ranged interactions and a single-component order parameter (such as many fluids and magnets) belong to the Ising universality class [101, 4], i.e., critical exponents are identical to those of the simple Ising model.

For the systems we study, the two relevant extensive variables are the (dimensionless) number density ρ and the energy density u, defined as $\rho = L^{-3}N$ and $u = L^{-3}U$, respectively. Here N is the number of particles, L is the linear dimension of the system (in units of σ), and U is the total energy. The order parameter $\mathcal{M}$ for our systems is a

linear combination of u and ρ, given by

$$\mathcal{M} = \frac{1}{1 - sr}[\rho - su]. \tag{6.6}$$

where r and s are two system specific parameters (see below). Correspondingly, the energy-like parameter u is given by

$$\mathcal{E} = \frac{1}{1 - sr}[u - r\rho]. \tag{6.7}$$

We will show, as is expected, that this system belongs to the Ising universality class. This class is controlled by two relevant scaling fields, with τ as the thermal scaling field and h as the ordering scaling field. For the Ising model itself, we simply have $\tau = T - T_c$ and $h = H$ where T and H are the temperature and magnetic fields, respectively, and T_c is the critical temperature. For fluids, the scaling fields are (asymptotically) linear combinations of the temperature and chemical potential differences [93]:

$$\tau = \omega_c - \omega + s(\mu - \mu_c), \qquad h = \mu - \mu_c + r(\omega_c - \omega) \tag{6.8}$$

where $\omega = T_0/T$ is the dimensionless inverse temperature and μ is the reduced chemical potential (in units of kT); the subscript c denotes the location of the critical point. The parameters r and s control the degree of mixing, and vanish identically when the Ising symmetry is present. In particular, r is identifiable as the limiting critical gradient of the coexistence curve in the space of μ and ω. Conjugate to these two fields are the scaling operators defined in Equations (6.6) and (6.7), which are the variables actually calculated during the simulation.

The FSS ansatz [15] is

$$P_L(\mathcal{M},\mathcal{E}) \simeq \tilde{P}_{\mathcal{M},\mathcal{E}}(\Lambda_{\mathcal{M}}^{\dagger}\delta\mathcal{M}, \Lambda_{\mathcal{E}}^{\dagger}\delta\mathcal{E}) \tag{6.9}$$

where

$$\Lambda_{\mathcal{E}} = a_{\mathcal{E}}L^{1/\nu}, \qquad \Lambda_{\mathcal{M}} = a_{\mathcal{M}}L^{d-\beta\nu}, \qquad \Lambda_{\mathcal{M}}\Lambda_{\mathcal{M}}^{\dagger} = \Lambda_{\mathcal{E}}\Lambda_{\mathcal{E}}^{\dagger} = L^d \tag{6.10}$$

and

$$\delta\mathcal{M} = \mathcal{M} - \langle\mathcal{M}\rangle_c, \qquad \delta\mathcal{E} = \mathcal{E} - \langle\mathcal{E}\rangle_c, \tag{6.11}$$

where the parameters $a_{\mathcal{M}}$ and $a_{\mathcal{E}}$ are nonuniversal scaling factors, β and ν are the critical exponents for the coexistence curve and correlation length, respectively. The subscript c in the above equations denotes that the averages are to be taken at criticality.

$P_L(\mathcal{M},\mathcal{E})$ describes the joint distribution of $\mathcal{M}$ and $\mathcal{E}$ for a given system size L. It is related to the joint distribution of density and energy via

$$P_L(\mathcal{M},\mathcal{E}) = (1 - sr)P_L(\rho, u) \tag{6.12}$$

Integrating out the energy-like dependence from both sides, we have $P_L(\mathcal{M})$ expressed in terms of $P_L(\rho, u)$. Since the Ising universality class exhibits the same critical behavior as the Ising model [87, 77, 101, 126, 127, 79, 15], $P_L(\mathcal{M})$ must match the universal fixed point function

$$\tilde{P}^*_{\mathcal{M}}(x) = \int \tilde{P}^*_{\mathcal{M},\mathcal{E}}(x, y)dy \tag{6.13}$$

where $\tilde{P}^*_{\mathcal{M}}(x)$ is identifiable as the critical magnetization distribution of the Ising model, whose form is known from independent study [110]. The critical point can then be estimated by tuning the temperature T, chemical potential μ and field-mixing parameter s such that $P_L(\mathcal{M})$ collapses onto $\tilde{P}^*_{\mathcal{M}}(x)$. $P_L(\mathcal{M})$ is extremely sensitive to the value of μ, up to the fourth significant number after the decimal point for our case.

Note that a similar situation pertains to the energy operator distribution $P_L(\mathcal{E})$. The limiting fixed point function is

$$\tilde{P}^*_L(x) = \int \tilde{P}^*_{\mathcal{M},\mathcal{E}}(x,y)dx \tag{6.14}$$

which is also known from independent Ising model studies.

To avoid tedious simulations and save computer time, once the joint PDF is obtained via a GCMC simulation for a particular β and μ, histogram reweighting can be used to obtain the PDF at a new β' and μ', so long as β' and μ' are in the neighborhood of β and μ:

$$P_L^{(\beta',\mu')}(\rho,u) = \frac{\exp[(\mu'-\mu)\rho V - (\beta'-\beta)uV]P_L^{\beta,\mu}(\rho,u)}{\sum \exp[(\mu'-\mu)\rho V - (\beta'-\beta)uV]P_L^{\beta,\mu}(\rho,u)} \tag{6.15}$$

where $V = L^3$ is the volume of the system.

To determine the critical parameters of the infinite system for the potentials under consideration, our grand canonical simulations used system sizes of L=6, 8, 10, 12 and 14. These sizes correspond to average particle numbers of approximately 75, 180, 340, 600 and 930, respectively. To ensure proper equilibration in the grand canonical en-

semble simulations, $(L/2)^3$ cycles of 10^7 Monte Carlo steps were used, where a Monte Carlo step is a random attempt of either particle creation or annihilation in the simulation cell. In general, translational moves are not necessary as these are realized through random particle creation.

The subcritical coexistence region

Due to large free energy barriers, conventional GCMC simulation is not suitable to study coexistence in the subcritical region. Approaches for dealing with this problem fall into two broad categories: simulations without interfaces and biased sampling techniques. In this chapter we implement the multicanonical Monte Carlo method from the second category; results using Gibbs ensemble Monte Carlo(GEMC) from the first are also shown for comparison.

The basic idea of the multicanonical ensemble approach [8] is to preweight the sampling of configuration space so as to artificially enhance the frequency of occurrence of states with intrinsically low probability, due to the free energy barrier. This can be achieved by sampling not from a simple Boltzmann distribution with a Hamiltonian $H(\{\mathbf{r}\},\rho)$, but from a modified distribution with an effective Hamiltonian $H'(\{\mathbf{r}\},\rho) = H(\{\mathbf{r}\},\rho) + g(\rho)$, where $g(\rho)$ is a preweighting function such that

$$P'(\rho) = \frac{1}{Z} \prod_{i=1}^{N=\rho V} \{\int_V dr_i\} e^{-\beta H'(\{\mathbf{r}\},\rho)} \tag{6.16}$$

where Z is the partition function. We can choose $g(\rho)$ such that the calculated $P'(\rho)$ is

approximately flat over the entire density range separating the two pure phases.

Once the statistics of $P'(\rho)$ are obtained from GCMC simulations, $P(\rho)$ can be determined by unfolding the effects of the multicanonical preweighting:

$$P(\rho) = P'(\rho)e^{\beta g(\rho)} \tag{6.17}$$

The crucial step in this process is to find a suitable preweighting function $g(\rho)$. If one knows $P(\rho)$ exactly beforehand then the choice of $g(\rho) = \frac{1}{\beta}\ln(P(\rho))$ would result in a constant $P'(\rho)$ throughout the entire configuration space. However, this is the very $P(\rho)$ we are trying to find from the simulation. A good estimate of $P(\rho)$, however, can be readily obtained from histogram reweighting with the knowledge of the PDF at a nearby T and μ. The basic procedure is outlined as follows:

1. Start with a near-critical coexistence density distribution $P_{T_1,\mu_1}(\rho)$, which is easily obtainable since the free energy barrier between the two phases is small near T_c.

2. Choose a subcritical temperature T_2 close to T_1 and perform histogram reweihgting. Then adjust μ until the areas under the two separate peaks are equal. Denote the reweighted PDF as $\tilde{P}_{T_2,\mu_2}(\rho)$. Assign $g_{T_2}(\rho) = \frac{1}{\beta}\ln(\tilde{P}_{T_2,\mu_2}(\rho))$.

3. Perform a GCMC simulation at (T_2, μ_2) using $g_{T_2}(\rho)$ as the the biasing function; create a histogram of the biased density distribution $P'_{T_2,\mu_2}(\rho)$. The biased acceptance probabilities for insertion and deletion are now:

$$p_{acc}(N \to N+1) = \min[1, \frac{V}{N+1}\exp[-\beta(\Delta U - \mu + g(\rho_n) - g(\rho_o))]] \tag{6.18}$$

$$p_{acc}(N \to N-1) = \min[1, \frac{N}{V}\exp[-\beta(\Delta U + \mu + g(\rho_n) - g(\rho_o))]] \tag{6.19}$$

where $\rho_o = N/V$, $\rho_n = (N+1)/V$ or $(N-1)/V$.

4. Unbias P' to obtain the Boltzmann PDF at T_2, μ_2. Denote it as $P_{T_2,\mu_2}(\rho)$.

5. Adjust μ again from the corrected distribution until the areas under the two separate peaks (from histogram reweighting) are equal. Denote this new μ as μ_{coex}. The positions of the peak values in the distribution function yield the coexisting densities. This step improves the estimate for the location of the coexistence densities at T_2, μ_2 from Step 2.

6. Repeat from Step 1. Set $(T_2, \mu_2, P_{T_2,\mu_2}(\rho))$ to be the starting point.

Step 5 can be omitted if the difference between T_1 and T_2 is sufficiently small. In that case, the peak values from Step 2 can be used as coexisting densities. However, to gain more accuracy in μ_{coex}, we suggest that Step 5 be carried out. One thing we want to stress is that, in constructing $\tilde{P}_{T_2,\mu_2}(\rho)$, there will be histogram bins with zero entries at the extrema of small and large ρ; we find it useful to set all these entries to the nearest non-zero entry, in order to avoid possible unphysical values of acceptance ratios during the biased runs.

We have also implemented the Gibbs ensemble method in the subcritical region. The GEMC method [84] was designed to study coexistence in the region where the free energy barrier is sufficiently high to avoid crossing between the two phases. It also avoids problems associated with the formation of an interface between the dense and dilute fluid phases. The details of this method can be found in Ref. [84]; since this

is a standard method in computational physics, we do not discuss it here. Our Gibbs ensemble simulation generally ran $3 * 10^9$ Monte Carlo steps, 20% of which were used for equilibration. A Monte Carlo step in the Gibbs ensemble was a choice of a particle transfer, volume move, or translational move. These simulations consisted of roughly 66% transfer attempts, 33% translational attempts and 1% volume attempts.

6.3 Results

Table 6.1: Summary of the infinite system critical parameters for lysozyme solutions with 0.1M NaI electrolyte.

T_c^*	μ_c^*	ρ_c^*	s	r
0.945(1)	-2.528(5)	0.3515(6)	-0.02	-1.56(6)

We first list the results for the critical parameters of the bulk system obtained from FSS for the three electrolyte solutions studied in Table 6.1. In this section, we use reduced units, i.e.

$$\tilde{L} = L/\sigma, \quad \tilde{T} = T/T_0, \quad \tilde{U} = U/kT_0, \quad \tilde{\mu} = \mu/kT_0, \quad \tilde{\rho} = \rho\sigma^3/L^3 \tag{6.20}$$

For simplicity, the tilde sign is omitted from now on. Note that the asterisk $(*)$ denotes the bulk behavior, i.e., the values are for the limiting case of infinite system size. The values of r were estimated as the limiting critical gradient of the coexistence curve in the space of μ and ω [122], i.e. r was determined as a byproduct from the subcritical

coexistence results, rather than from the FSS method. The distribution for the ordering operator fluctuations $\mathcal{M}$ at the apparent critical point of the NaI electrolyte, for $L = 8$, is shown in Figure 6.1. It can be seen that the agreement for the ordering parameter $\mathcal{M}$ is good [1] for this system size; other system sizes are omitted in this plot for clarity. Note that the distribution is shown as a function of the scaled variable $x \equiv a_{\mathcal{M}}^{-1} L^{\beta/\nu}(\mathcal{M} - \mathcal{M}_c)$. Here ν is the critical exponent for the correlation length and β is the critical exponent of the order parameter. For the 3D Ising universality class, $\nu = 0.629$ and $\beta = 0.326$ [29]. We can obtain from this matching the apparent critical point $T_c(L)$ and $\mu_c(L)$, as well as good estimates of the field-mixing parameter s. The size dependence of the apparent critical parameters is shown in Figure 6.2 (a) and (b).

FSS predicts that

$$T_c^*(\infty) - T_c(L) \sim L^{-(\theta+1)/\nu}, \quad \mu_c^*(\infty) - \mu_c(L) \sim L^{-(\theta+1)/\nu} \tag{6.21}$$

where θ is the universal correction to scaling exponent, whose value has been estimated to be $\theta \approx 0.54$ for the 3D Ising universality class [19, 78]. By extrapolating to infinite volume, we can get an estimate of the true bulk behavior (Table 6.1). Figure 6.2(c) shows the size dependence of $\rho_c^*(L)$, the critical density (evaluated via histogram reweighting for each size), at infinite volume critical point T_c^* and μ_c^*. FSS predicts that:

$$\rho_c^*(\infty) - \rho_c^*(L) \sim L^{-(d-1/\nu)} \tag{6.22}$$

[1] Note that the deviations are to be expected due to corrections from scaling for finite-size systems. See Ref. [122]

Table 6.2: Coexistence parameters in the subcritical region from the multicanonical histogram reweighting method.

T	μ_{coex}	ρ_v	ρ_l
0.91	-2.5838	0.1362	0.5986
0.885	-2.6284	0.1037	0.6384
0.86	-2.6799	0.0742	0.6953
0.836	-2.7327	0.06	0.7276
0.813	-2.7914	0.0454	0.7551
0.8	-2.8248	0.039	0.7793
0.775	-2.90	0.0293	0.7949

where $d = 3$ is the dimension of the system. The corresponding density distributions at T_c^* and μ_c^* are shown in Figure 6.3 for different system sizes.

The multicanonical histogram reweighting method provides a good estimate for the coexistence curve in the subcritical region. In Table 6.2, we display the chemical potential μ_{coex} obtained from histogram reweighting, as well as the corresponding coexisting densities ρ_v and ρ_l; the GEMC results are shown in Table 6.3. Figure 6.4 shows the PDF of density. We show the complete liquid-liquid coexistence curves in the space of ρ and T in Figure 6.5, together with results obtained from GEMC simulations. Note that the results obtained using the two methods coincide with each other. In Figure 6.6, we plot the chemical potential μ_{coex} as a function of T along the coexistence curve (as obtained

Table 6.3: Coexistence densities in the subcritical region from the Gibbs Ensemble Monte Carlo (GEMC) method.

T	ρ_v	ρ_l
0.875	0.0977	0.6633
0.85	0.0702	0.6978
0.825	0.0578	0.7434
0.8	0.0434	0.7748
0.775	0.0328	0.8039

from the multicanonical simulations).

6.4 Conclusion

We conclude this chapter by making a comparison of the phase diagrams among lysozyme solutions with different types of electrolyte. Figure 6.7 shows the complete liquid-liquid coexistence curves in the space of ρ and T for two other solutions with the added salt being 0.1 M NaCl and a non-polarizable salt[1], together with our results for NaI. We have quantitatively demonstrated for the model of aluminum oxide the important effect of salt type on the phase diagrams of nanoparticles in electrolyte solutions. For example, the critical point of the NaI is significantly higher than that of the non-polarizable salt

[1]These two coexistence curves were obtained by my colleagues and were published in [65]

system, due to the ion-dispersion forces.

In addition, we have calculated the critical point parameters and scaling fields for this model and shown as expected, it belongs to the Ising universality class. It is obvious that future progress in this field will depend on more accurate models of the Hofmeister effect. Other proposals have been made to account for the Hofmeister effect, including a recent paper dealing with hydrophobic surface forces [71]. (We have reviewed briefly in Chapter 3 the hydrophobic surface forces and have studied this effect for a model of lysozyme in Chapter 5.) It would be helpful to have an experimental determination of the phase diagram to test the accuracy of the model of Deniz et al [25]. Nevertheless, our results clearly demonstrate as first shown in Ref. [25], the important role of the ion-dispersion effects on the fluid-fluid coexistence curve of nanoparticles in electrolyte solutions.

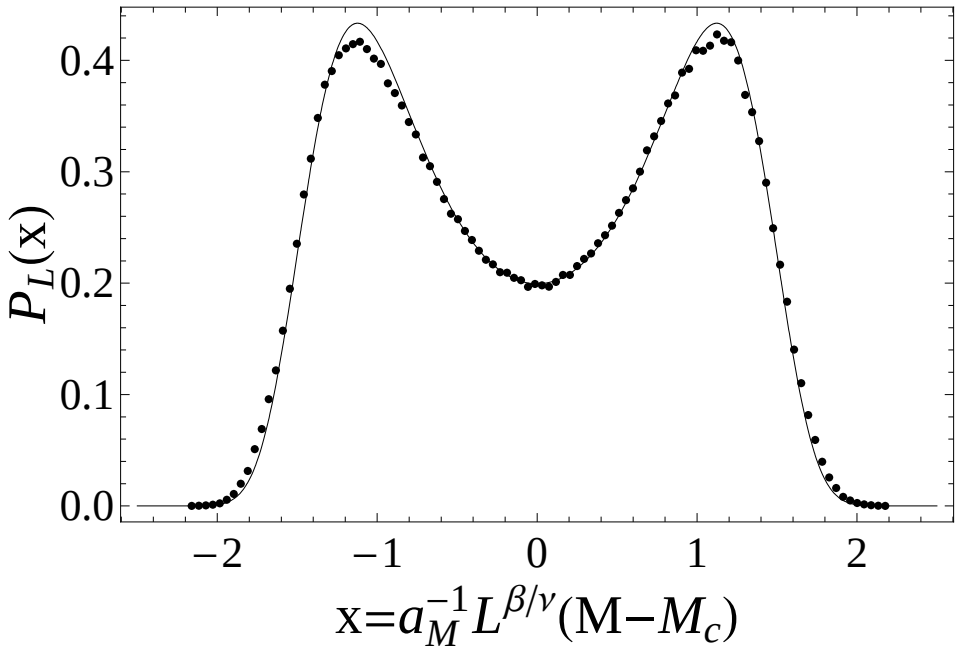


Figure 6.1: The calculated form of the ordering operator distribution $P_L(\mathcal{M})$ for the L=8 system size, at the apparent critical parameters $T_c^* = -0.9433, \mu_c^* = -2.531$. Also shown for comparison is the universal fixed point ordering operator distribution $\tilde{P}_{\mathcal{M}}(x)$. The data have been expressed in terms of the scaling variable $x = a_{\mathcal{M}}^{-1} L^{\beta/\nu}(\mathcal{M} - \mathcal{M}_c)$, with the value of the nonuniversal scale factor $a_{\mathcal{M}}^{-1}$ chosen so that the distribution have unit variance. β and ν are the critical exponents for the coexistence curve and correlation length, respectively.

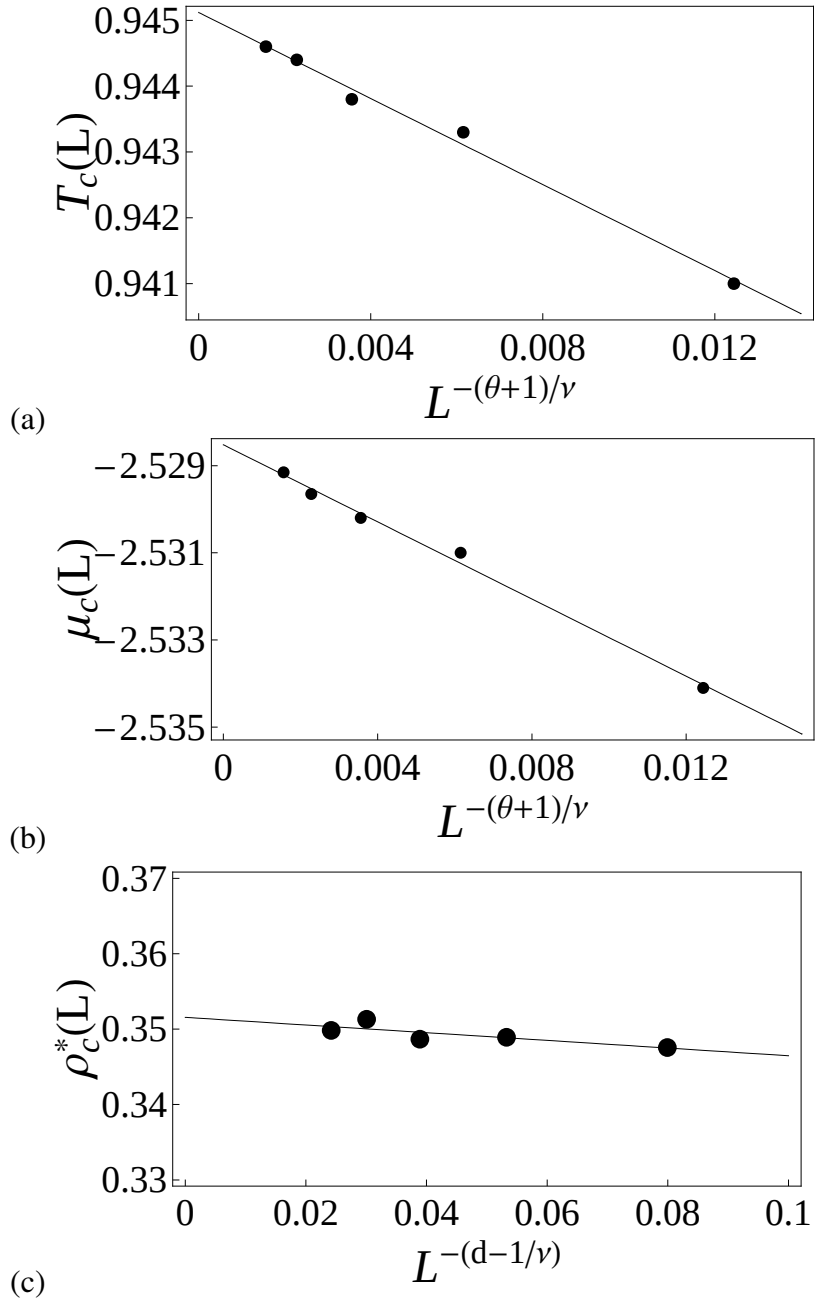


Figure 6.2: FSS results for (a) $T_c(L)$, (b) $\mu_c(L)$ and (c) $\rho_c^*(L)$ (See text for definitions) as a function of $L^{-(\theta+1)/\nu}$ and $L^{-(d+1)/\nu}$ respectively.

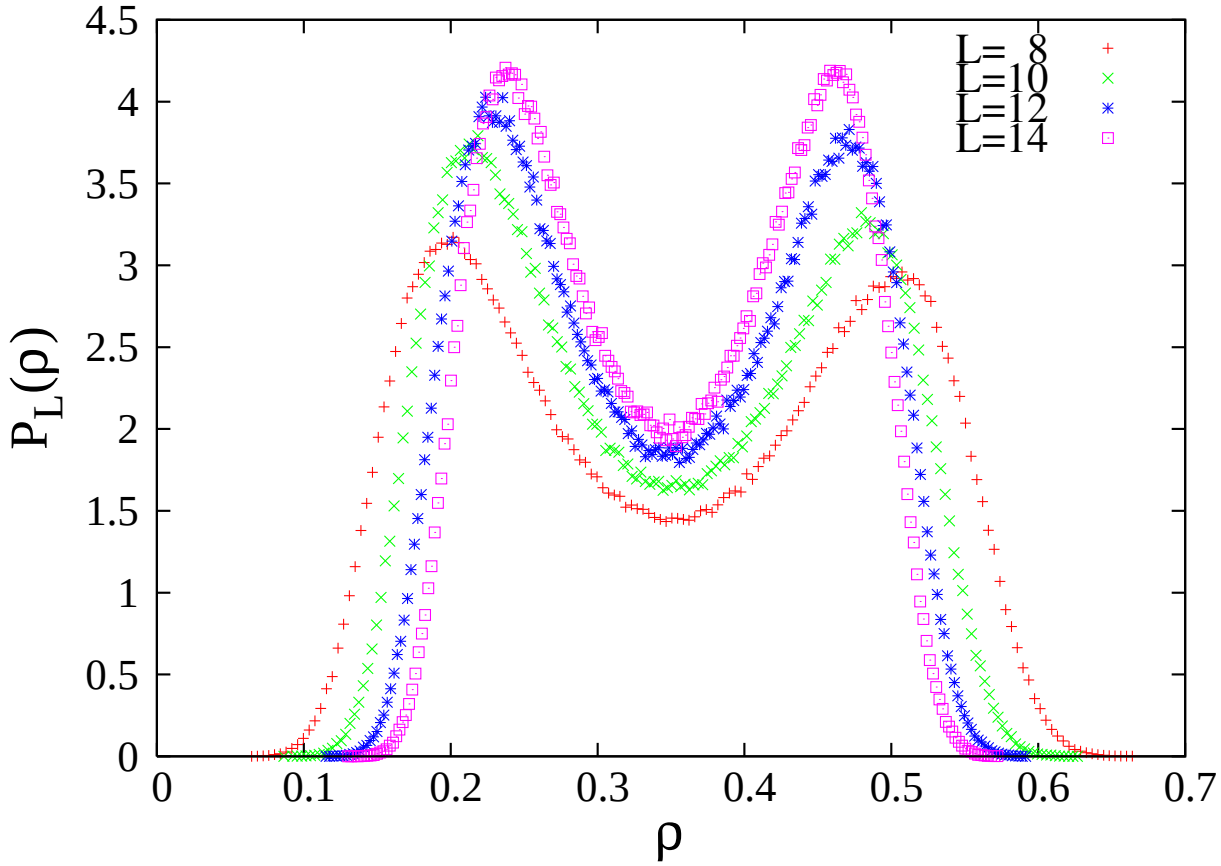


Figure 6.3: Probability distribution function of the density at the critical point T_c^*, μ_c^* for L=8,10,12,14. From outer plot to inner plot: L=8(pluses), L=10(crosses), L=12(asterisks), L=14(squares).

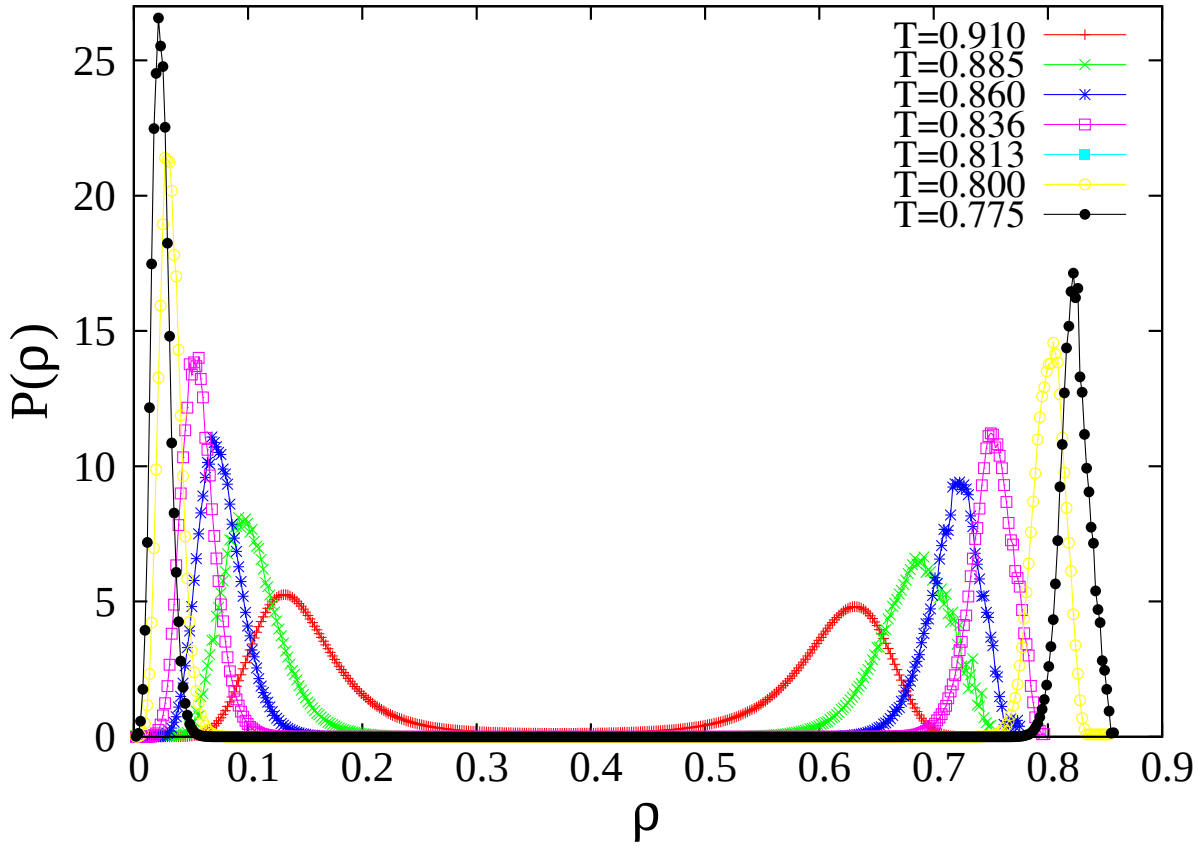


Figure 6.4: A series of calculated $P(\rho)$ obtained from multicanonical histogram reweighting corresponding to phase coexistence at temperatures displayed (L=8).

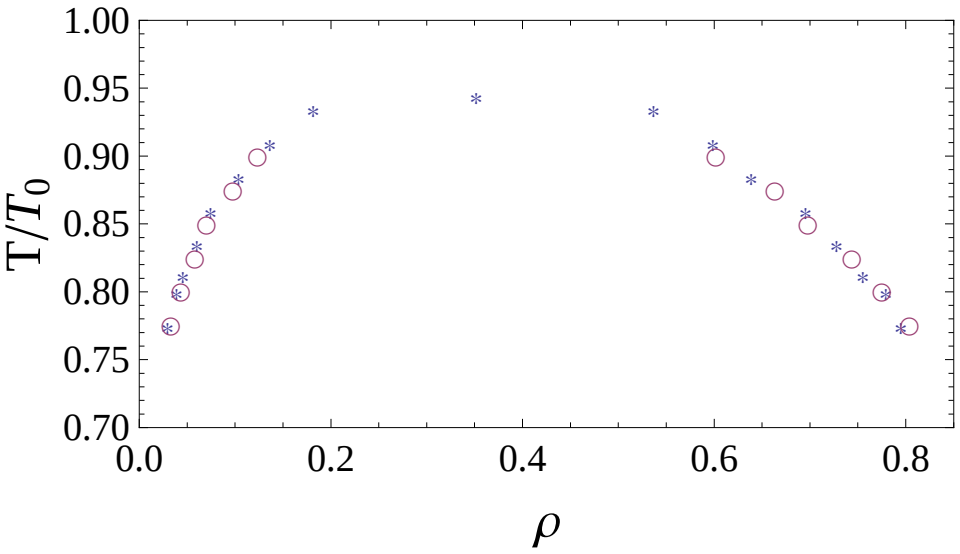


Figure 6.5: Phase diagrams of T vs ρ obtained from FSS/Gibbs/multicanonical histogram reweighting. Squares are the results obtained from the Gibbs ensemble and asterisks are the results of the multicanonical histogram reweighting method; filled circles are estimates of critical point from FSS.

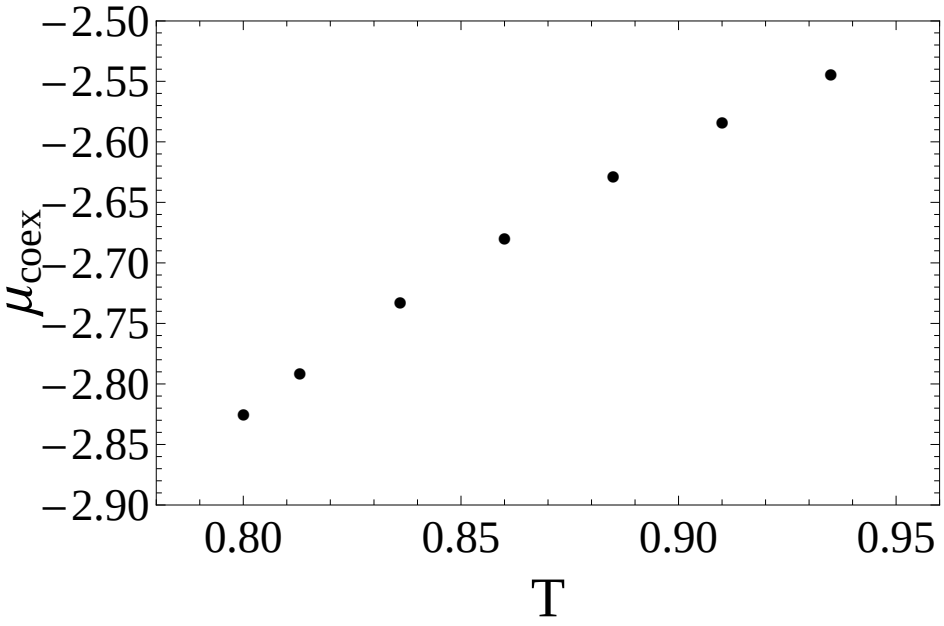


Figure 6.6: Chemical potential μ vs. temperature T along the coexistence curve. By plotting μ vs $1/T$ we can obtain estimates of r (as shown in Table 6.1).

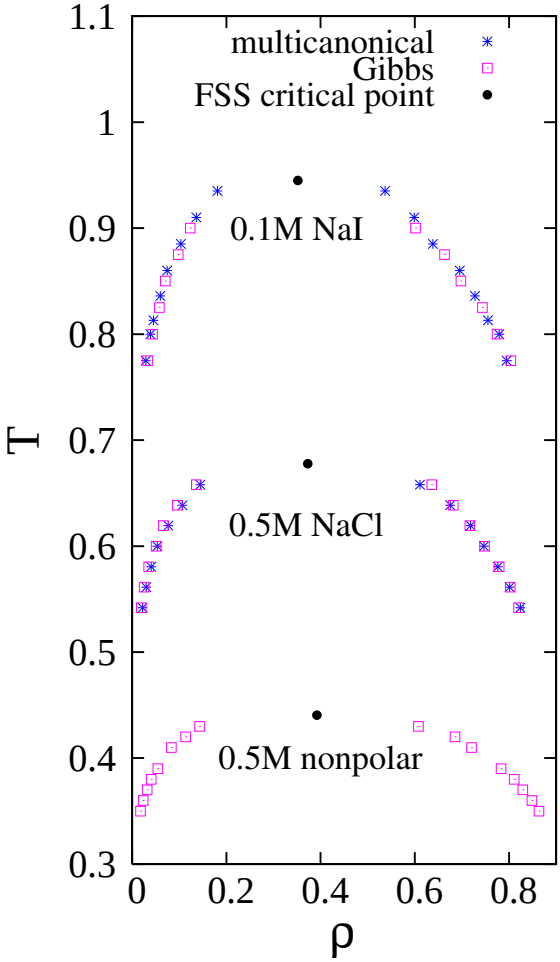


Figure 6.7: Phase diagrams of T vs ρ obtained from FSS/Gibbs/multicanonical histogram reweighting for systems with added salt type being NaI, NaCl, and non-polarizable salt, respectively. Squares are the results obtained from the Gibbs ensemble and asterisks are the results of the multicanonical histogram reweighting method; filled circles are estimates of critical points from FSS.

Chapter 7

A Simple Model of Directional Interactions for Proteins

7.1 Introduction

There has been considerable interest in recent years in understanding the equilibrium and nonequilibrium properties of aqueous solutions of globular proteins. A major reason for this is to determine the optimal conditions necessary for growing high quality protein crystals. These crystals are requisite for X-ray diffraction studies of protein structure; understanding structure is necessary to understand protein function. Another important reason is that several human diseases are caused by undesired protein aggregation from solution, including certain cataracts, sickle cell anemia and Alzheimer's disease. Most of the models studied have considered only isotropic interactions between

spherical protein molecules. These models have provided a semi-quantitative understanding of the protein phase diagrams for lysozyme and gamma-crystallin and have provided a basis for studying crystal nucleation [95, 109, 3, 41]. However, real proteins almost always have anisotropic interactions. The anisotropy may be due to a variety of different mechanisms, including interactions between nonuniformly distributed surface charges, the presence of hydrophilic/hydrophobic regions on the protein surface and the formation of hydrogen bonds. As a consequence, several recent studies have focused on anisotropic models, such as the patch model originally studied by Kern and Frenkel [55] and site-site models introduced by Wertheim [116, 117, 118, 119] and studied by Jackson et al. [49, 18], Sear [100] and others [103]. Kern and Frenkel [55] showed that the presence of anisotropy could broaden the width of the liquid-liquid coexistence curve, to be in better agreement with experiment than isotropic models. They also showed that the critical point of this curve moved to lower temperatures as the interactions become more anisotropic. However, they did not determine the crystal phase nor the liquid-solid coexistence line. The introduction of anisotropy can also induce the stability of multiple solid phases, including orientationally ordered and disordered phases [17].

In addition to the field of globular proteins, another area in which anisotropic interactions have received considerable attention is the development of new materials. In particular, one challenge in the fabrication of colloids and nanoparticles is how to tailor the interactions between particles so that they are able to self-assemble into a given

target structure. One of the most desirable structures is the diamond structure because of its potential as photonic materials [48]. A number of recent theoretical studies have begun to address the question of how patchy interactions can be used to control the crystallization behavior [130, 27] and the self-assembly of finite objects of a given size and symmetry [129, 42, 125, 121].

Patchy models have also been used to model the equilibrium polymerization of polymers. Wertheim developed a thermodynamic perturbation theory for two patch site version of the patch model that has been shown in studies to provide an excellent description of various properties of the model as obtained from Monte Carlo simulation [49, 18, 99]. Most recently Sciortino et al [99] determined numerically a variety of thermodynamic properties of the two patch site model, including the energy per particle, the fraction of particles in the associated state, the average chain length and its distribution function, and other properties and showed that the Wertheim theory agreed remarkably well with the simulation results. However, due to the small patch size used in their study, there is no fluid-fluid coexistence curve. This patch model has also been used by Sear [100] as a model of phase transitions of aqueous solutions of globular proteins, for different numbers of patches. In general he found that there is a metastable fluid-fluid coexistence curve, typical of lysozyme and gamma-crystallin, as well as a liquidus-solid coexistence. Thus the model is an interesting example of a simple, directional interaction model of proteins. For only two patches, however, the model does not have a fluid-fluid phase,

as the patch size is restricted to sizes such that three molecules cannot simultaneously bond (i.e. the model precludes trimers, following the original work of Wertheim). In this chapter we address the issue of how to generalize the two patch model so as to obtain a fluid-fluid coexistence curve, but also preserve the possibility that for certain protein concentrations one might form linear polymer chains (fibers) and possibly also might have a fiber-bundle transition of the type recently studied by Huisman et al [47]. These authors developed a model of polymerization that went one step further beyond linear polymerization; i.e., they presented Monte Carlo simulations of a model that is characterized with weak chain-chain interactions and found a first-order phase transition to bundles. They interpreted this bundling as a sublimation transition from a polymer gas to a solid bundle. Our model consists of two pieces: the two patch directional attraction piece described above, plus a weaker isotropic attractive interaction. This model has a rich parameter space characterized by the choice for the ratio of the two interaction ranges and two well depths. We will show below for particular choices of these ratios, that the addition of this isotropic interaction leads to a complex phase diagram, with a metastable fluid-fluid coexistence curve and competing crystal structures (bcc and fcc) that can also be orientationally ordered or disordered. We plan to explore in a subsequent work whether this model leads to a fiber-bundle phase transition, as one might expect from the existence of the stronger patch-patch interaction (leading to chains) plus a weaker interchain interaction from the isotropic piece. (It is possible, however, that

one might need an even weaker interchain interaction than chosen here.) Our results for the equilibrium phase diagram of our model share some generic features with a recent paper by Noya et al [82] in that there are competing crystal structures. However, their model is a multi-patch model without an isotropic interaction which led to competing simple cubic, bcc and fcc crystal structures. However, they did not find a fluid-fluid phase separation curve for their model.

The remainder of the chapter is as follows: in Sec. 7.2 we summarize the model while in Sec. 7.3 we review the relevant simulation techniques necessary to obtain the liquid-liquid and liquid-solid phase diagrams. In Sec. 7.4 and 7.5 we present a discussion of our resulting phase diagrams and a brief conclusion, respectively.

7.2 Two-Patch Model

Our model consists of hard-spheres with two types of attractive interactions between them: an attractive patch-patch interaction (each sphere has two patches) together with a weaker isotropic interaction. The total potential can be written as a sum of two-body terms that depend not only on the distance between two particles r_{ij}, but also on their relative orientations. The interaction between two particles i and j is described as

$$U_{tot}(i,j) = \begin{cases} \infty & \text{if } r_{ij} < \sigma \\ U_{iso} + U_{patchy} & \text{if } \sigma \leq r_{ij} < k\sigma \\ 0 & \text{otherwise.} \end{cases} \tag{7.1}$$

where σ is the hard core diameter, k is the attraction range (note that both the isotropic and anisotropic pieces have the same range). We use simple square well potentials for both U_{iso} and U_{patchy}:

$$U_{iso} = -\epsilon \tag{7.2}$$

$$U_{patchy} = \begin{cases} -\epsilon_p & \text{if } \hat{e}_{i,\alpha} \cdot \hat{r}_{ij} > cos\delta \text{ and } -\hat{e}_{j,\beta} \cdot \hat{r}_{ij} > cos\delta \\ 0 & \text{otherwise.} \end{cases} \tag{7.3}$$

where $\hat{e}_{i,\alpha}$ (patch vector) denotes the unit vector in the direction from the center of ith particle to the center of its αth patch, and $\hat{r}_{ij}$ denotes the unit vector in the direction from the center of ith particle to the center of jth particle. This patch definition is illustrated in Fig. 7.2. In addition, δ is the half angle of the patches, ϵ and ϵ_p are the well depths of the isotropic and anisotropic interactions, respectively. In this chapter, we choose $\epsilon_p = 2\epsilon$, which means the attraction at the patches is 3 times of the attraction elsewhere. Thus, two particles bind more easily when they face each other at the patch positions. We choose the value of δ such that one particle can interact with no more than one other particle at the patch position, thus at certain temperatures, it is possible that chains form first and go through a bundle transition afterwards. We do not study this possibility here.

We list the value of the parameters below:

$$k = 1.2 \tag{7.4}$$

$$\delta = 0.91 \tag{7.5}$$

$$\epsilon_p = 2\epsilon \tag{7.6}$$

We shall use reduced units throughout, so that

$$U^* = U/\epsilon \tag{7.7}$$

$$P^* = P/(\epsilon/\sigma^3) \tag{7.8}$$

$$T^* = T/(\epsilon/k_B) \tag{7.9}$$

$$\rho^* = \rho\sigma^3 \tag{7.10}$$

We omit the asterisks for simplicity for the rest of this chapter. We note that although choosing the ranges for the patch and isotropic interactions to be equal is arbitrary, it is not unreasonable and leads to an interesting phase diagram. Other choices would lead to different competing crystal structures.

7.2.1 Crystal Structures

For the range of interaction considered in this study ($k = 1.2$), the body-centered-cubic (bcc) structure has a lower ground state energy than the face-centered-cubic (fcc) structure. The reason is that for the fcc structure the particles can only interact with

the nearest neighbors (n.n), while for bcc they can also interact with the next nearest neighbors (n.n.n) for a narrow density range.

More specifically, for bcc, when a particle touches its n.n (the separation is σ), the distance between n.n.n is $\sigma/(\sqrt{3}/2) = 1.1547\sigma < 1.2\sigma$, which is still within the range of attraction of the square-well potentials. As a result, the potential energy of the bcc structure has contributions from interactions with 8 n.n plus 6 n.n.n. for a total of 14 neighbors. The fcc structure, however, can never have interactions between n.n.n, even when the n.n touch each other, since then the distance between n.n.n is $(\sigma/(\sqrt{2}/2) = 1.414\sigma > 1.2\sigma)$, which still exceeds the interaction range $k = 1.2$. Thus, the fcc lattice has a smaller number of interacting neighbors, equal to 12; thereby it has a somewhat higher energy than the bcc structure, As we will see, there is competition between bcc and fcc at different temperatures.

The expression of the Gibbs free energy is $G = U+PV-TS$. At $T = 0$, this reduces to $G = U + PV = H$, and the chemical potential $\mu = G/N = u + Pv = h$. Thus, at constant pressure, it is the enthalpy H that needs to be minimized at zero temperature. For this simple model, we are able to calculate analytically the pressure at which a bcc structure can coexist with an fcc structure by setting $h_{bcc} = h_{fcc}$. Thus,

$$u_{bcc} + Pv_{bcc} = u_{fcc} + Pv_{fcc} \tag{7.11}$$

and

$$
\begin{aligned}
P &= \frac{u_{fcc} - u_{bcc}}{v_{bcc} - v_{fcc}} \\
&= \frac{1}{v_{bcc} - v_{fcc}} \\
&= \frac{1}{\frac{1}{4}P(\frac{1}{\sqrt{2}/2})^3 - \frac{1}{2}P(\frac{1}{\sqrt{3}/2})^3} \\
&\simeq 15.9506
\end{aligned}
$$

where we assume that both crystal structures are at their highest possible densities. We will see later on that the predicted pressure agrees very well with simulation results (Fig. 7.8). Therefore, at zero temperatures, the bcc is only stable up to the pressure 15.9506, beyond which the fcc becomes the stable state.

Note the bcc and fcc discussed above has an orientational order in addition to the translational order (see Fig. 7.1). This orientational order is caused by the anisotropy introduced by the two opposing patches. Each particle can interact at most with two neighbors at the patch position due to the small patch sizes, as a result of the constraint of our model. At sufficiently high temperatures when the entropy effect dominates, a translationally ordered, but orientationally disordered fcc structure will also appear. We refer to this structure as fcc-d. Similarly, we refer to the orientationally ordered structures as fcc-o and bcc-o. We list some of the important features of the two crystal structures in 7.1.

7.3 Simulation techniques

At a given temperature, coexistence between two phases occurs when the pressure and chemical potential are the same for both phases, i.e., $P_1 = P_2$ and $\mu_1 = \mu_2$, with $\mu = G/N = F/N + PV/N = f + P\rho$, where N is the total number of particles, F is the Hemholtz free energy, and f is F/N.

7.3.1 Equation of State

To obtain the coexistence phases at a given temperature, we need to perform Monte Carlo (MC) NPT simulations to obtain the equation of state $P(\rho, T)$ along an isotherm for each phase. Each simulation consists of between 50 000 and 100 000 MC cycles, with the same number of equilibration and production cycles. An MC cycle is defined as N attempts to move (translate + rotate) a particle (particle move) or change the volume of a box (volume move). The ratio of a particle move to a volume move is chosen to be 99:1. The number of particles used in our calculations is 500 for the fluid phase, 500 for the fcc phase and 432 for the bcc phase.

7.3.2 Free Energy Calculations

The free energy of the fluid phase is estimated by integration from an ideal gas:

$$F(\rho) = F_{id} + N \int_0^{\rho} d\rho' \frac{P(\rho') - \rho' kT}{\rho'^2} \tag{7.12}$$

where $F_{id}(\rho) = NkT(\ln(\rho\Lambda^3)-1)$. In what follows we shall write $F_{id}(\rho) = NkT(\ln(\rho)-1)$ and ignore the $3\ln\Lambda/\sigma^3$, as it plays no role in the location of phase equilibria of classical systems.

In order to calculate the absolute value of $F(\rho)$ of a solid phase, we use the well known Einstein crystal [32, 112, 98, 17, 82] as a reference system with the potential. For the orientationally ordered crystals (bcc-o and fcc-o), the equilibrium crystal exhibits an orientational order in addition to the translational order. Thus, when coupling our model particles to the lattice sites, we need both an orientational field and a translational field that tend to keep the particles at the positions and orientations of the perfectly ordered lattice. The potential energy of this system is then:

$$U(\lambda_o, \lambda_t) = U_{tot} + \lambda_o \sum_{i=1}^{N} \sin^2 \Psi_i + \lambda_t \sum_{i=1}^{N} (\overrightarrow{r}_i - \overrightarrow{r}_{0,i})^2 \tag{7.13}$$

where U_{tot} is the potential energy of our model $U_{tot} = \sum_{i<j} U(i,j)$. The second term on the right hand side is the orientational field and Ψ_i is the minimum angle formed by any of the two patch vectors on ith particle with respect to the z axis, where the z axis coincides with the equilibrium orientation of a chosen patch vector in the perfect lattice. Note that the orientational field has been chosen so that it has the same symmetry as the particles. The third term is the regular translational field and $\overrightarrow{r}_{0,i}$ is the lattice position of particle i. λ_o and λ_t are the coupling parameters of the two fields, respectively. (Note they are also in reduced units, i.e., $\lambda_o^* = \lambda_o/\epsilon$ and $\lambda_t^* = \lambda_t/\epsilon\sigma^2$ and we omit the asterisks for simplicity.)

To simplify the integration process, we choose $\lambda_o = \lambda_t = \lambda$, i.e., both fields are switched on simultaneously. The free energy difference between our model (U_{tot}) and the reference Einstein crystal ($U(\lambda_o, \lambda_t)$) is then given by

$$\Delta F_2 = F(\lambda = 0) - F(\lambda_{max}) = \int_{\lambda_{max}}^{0} d\lambda \langle \frac{\partial U(\lambda_o, \lambda_t)}{\partial \lambda} \rangle_\lambda \tag{7.14}$$

Computing the derivative in the integrand gives us

$$\Delta F_2 = N \int_{\lambda_{max}}^{0} d\lambda \langle \sin^2 \Psi + (\overrightarrow{r} - \overrightarrow{r}_0)^2 \rangle_\lambda \tag{7.15}$$

Thus it is really the average value of the mean squared displacements of both fields from their equilibrium positions that we calculate during the simulation. We numerically evaluate this integral using a 20-point Gauss quadrature formula.

To obtain the free energy of an interacting Einstein crystal $F(\lambda_{max})$, we use the noninteracting Einstein crystal as a reference system whose free energy is already known [32]. The difference between these two, ΔF_1, is obtained from the relation

$$\Delta F_1 = -kT \ln \langle \exp[-\frac{1}{kT} U_{tot}] \rangle \tag{7.16}$$

where $U_{tot} = \sum_{i<j} U(i,j)$, and the brackets denote a canonical ensemble average over configurations generated according to the canonical distribution function of the noninteracting Einstein crystal [32, 113]. We choose the maximum of λ so that the interacting crystal almost does not "feel" the interactions among the particles, i.e., the structure is very close to a perfectly ordered solid.

The translational part of the noninteracting Einstein crystal is given by

$$F_{Ein}^{t} = -\frac{3}{2}NkT\ln(\frac{\pi kT}{\lambda_t}) \tag{7.17}$$

while the orientational part is

$$F_{Ein}^{o}(\lambda) = -NkT\ln(\frac{1}{4\pi}\int_0^{\pi} d\theta d\Psi \sin\Psi \int_0^{2\pi} \exp[-\frac{\lambda\sin^2\Psi}{kT}]) + \ln 2 \tag{7.18}$$

We add the $\ln 2$ in the end to account for the two fold symmetry in the orientational field. This integral can be simplified as below:

$$F_{Ein}^{o}(\lambda) = -NkT\int_0^{1} dx \exp[\lambda(x^2-1)/kT] + \ln 2 \tag{7.19}$$

Summarizing everything, we reach the final expression for the free energy of the solid:

$$F_{tot} = F_{Ein}(\lambda_{max}) + \Delta F_1 + \Delta F_2 + \Delta F_3 \tag{7.20}$$

where $F_{Ein}(\lambda_{max}) = F_{Ein}^{t}(\lambda_{max}) + F_{Ein}^{o}(\lambda_{max})$. [1] The term ΔF_3 accounts for the difference between the integral in a regular system and one in which the center of mass of the system is fixed [32].

[1] For orientationally disordered solid, $F_{Ein} = F_{Ein}^{t}$ since no orientational order is present. Accordingly, we should remove the third term from equation 7.13 and keep only the coupling of the translational field.

The above procedure is performed only at one density ρ_s for one temperature T. Since the density is fixed during one calculation, we use NVT MC simulations, where the system is first equilibrated for a range of 50 000 to 100 000 cycles, followed by the same amount of cycles in production. The free energy at other densities along an isotherm can be obtained by integrating the equation of state

$$F(\rho) = F(\rho_s) + N \int_{\rho_s}^{\rho} d\rho' \frac{P(\rho')}{\rho'^2} \tag{7.21}$$

Once an initial pair of coexistence points is located, Gibbs-Duhem integration is performed to trace the whole coexistence curve

7.4 Results

We start by listing in Table 7.2 the free energies of all the solid phases at several thermodynamic states obtained from Einstein crystal simulations and the λ_{max} used for each of the states. Fig. 7.5 shows the convergence of the simulated system (equation 7.13) to the Einstein crystal as $\lambda \rightarrow \lambda_{max}$, for the fcc-o solid, at $T = 0.5$. We choose the λ_{max} such that the difference between the integrands is less than 1%.

Next we show how we locate the first pair of coexistence points at a certain temperature, $T = 0.9$. Fig. 7.4(a) shows isotherm plots for both the liquid and the stable solid (fcc-d). As already explained in Sec. 7.3.1, $\mu(\rho)$ is obtained using equation 7.12 for liquid and equation 7.21 for solid (fcc-d). The reference density we choose for

the fcc-d solid is $\rho_s = 1.09$; we perform Einstein crystal simulations for this density with $\lambda_{max} = 4000$. We show the subsequent plots of the chemical potentials against the pressures for both phases in Fig. 7.4(b); the position where the two lines intersect corresponds to the coexisting point at $T = 0.9$.

This procedure is similar for all temperatures considered. However, at low temperatures, the situation is a little more complicated since there can be a competition between bcc and fcc structures. For example, at $T = 0.1$, bcc-o can coexist with fcc-o at a certain pressure. Fig. 7.5 shows the corresponding isotherm plots and $\beta\mu - \beta P$ plots at this temperature.

Yet more intriguing is a situation found at $T = 0.3$, where there actually are two pressures at which the two solids can be at coexistence. Fig. 7.6 illustrates this case. It is difficult to locate the two intersections accurately, but we have performed similar procedures for several different temperatures nearby and believe that this is indeed the correct behavior. This finding suggests that our model has a reentrant behavior, which we will discuss later.

At a certain value (P,T), the phase with the lowest Gibbs free energy G ($\mu = G/N$) is the most stable state. And the transition that has the lowest coexisting G gives the stable transition; all others are metastable with respect to it. We start with the initial pair of stable coexistence points at a given temperature and trace out the full coexistence curve using Gibbs-Duhem integration. The $T - \rho$ and $P - T$ diagrams are shown in Figs.

7.7 and 7.8, respectively. The dashed lines in the diagrams are our estimates following the trend of the data obtained from the simulations. The dotdashed line shows where the transition occurs between the fcc-d and fcc-o structures. We estimate these points by heating the fcc-o structure and monitoring the internal energy U. U experiences a quite abrupt change when the transition occurs. We choose the transition temperature as the temperature where the internal energy curve shows an inflection point, as done in a recent study of a different model of anisotropy [82].

Clearly the phase diagram shows multiple solid phases. First, at high temperature, where the behavior is dominated by the repulsion between the particles, the fluid freezes into an fcc-d phase (an fcc lattice with translational order but with orientational disorder) (Fig. 7.4 depicts such a transition). Gibbs-Duhem integration extends the coexistence curve down to lower temperatures until fcc-o becomes more stable than fcc-d (dotdashed line in Figs. 7.7 and 7.8). Thus, at intermediate temperatures, the fluid freezes into an fcc-o structure. Finally at low temperatures, it freezes into a bcc-o structure. This coincides with the picture described in Fig. 7.5; the $\beta\mu - \beta P$ plot shows that at relatively low pressures, the bcc-o (dashed) lattice is more stable than the fcc-o (solid) crystal, since the former has a lower μ (The fluid $\beta\mu - \beta P$ curve is trivial, since it can be approximated by the ideal gas expression.). The bcc-o structure remains stable up to higher pressures when the fcc-o structure becomes more stable with a higher density (see Table 7.1 and Fig. 7.8).

At some intermediate temperature range (approximately $T \in (0.24, 0.38)$), the bcc-o - fcc-o coexistence exhibits an interesting behavior. This corresponds to the scenario depicted in Fig. 7.6. As the pressure P increases from 0, fluid first freezes into a low density fcc-o at very low pressures; as P increases further, a bcc-o structure emerges as the more stable state; finally when P becomes sufficiently high, a high-density fcc-o becomes more stable again. This is the so-called the reentrant behavior, in the sense that there are two pressures where the two states can coexist. This behavior has been found by computer simulations for different types of models [112, 97, 82]. It is caused by the fact that fcc-o can be less dense and more dense than bcc-o at different pressures. The two intersections in Fig. 7.6 stand for the two coexistence points for $T = 0.3$ (see Table 7.3 for the values of P). We follow these two points via separate Gibbs-Duhem integrations and obtain the domelike shape in the $T - \rho$ phase diagram (7.7). The coexisting pressures along the two branches are shown in Fig. 7.8. Both branches meet at the top of the dome marked with a filled circle (in both Fig. 7.7 and Fig. 7.8), where dP/dT changes sign. This is typical of the reentrant behavior. We note that for this temperature range, bcc-o is only stable for a very narrow range of densities, due to its small compressibility.

The phase diagram exhibits a triple point marked with a filled square. The position of this triple point is estimated by extending the fcc-o branch of the fluid-fcc-o coexistence curve following its trend. At this point, fluid, fcc-o and bcc-o coexist. Below this point,

the fluid-bcc-o transition becomes the stable transition with respect to the fluid-fcc-o transition. The simulation shows that bcc-o is stable up to a pressure of approximately 16.575 at T=0.1. This is in agreement with the analytical value of 15.9506.

Finally, Fig. 7.7 also displays a metastable fluid-fluid coexistence curve. The rectilinear fit estimates the critical point to be at $T_c \simeq 0.71$ and $\rho_c \simeq 0.40$ (marked with an asterisk). We trace this curve only down to $T \sim 0.6$, since the system becomes increasingly difficult to equilibrate below this point due to the stickiness of the system.

7.5 Conclusion

We have studied a simple two patch model with two types of attractive interactions: a weaker isotropic attraction plus a stronger patch-patch attraction between two opposing patches on the surface. We have determined the fairly complex phase coexistence curves, despite the simplicity of the model, at various temperatures. We find a metastable fluid-fluid coexistence curve with respect to the fluid-solid coexistence. The lowest-energy structure is an orientationally ordered bcc (bcc-o) state; as the pressure increases, the orientationally ordered fcc state becomes most stable. We also observe a reentrant behavior between bcc-o and fcc-o at an intermediate range of temperatures. Finally, on increasing temperature, entropy effects become more important and a fcc-d (an fcc structure with a translational order but no orientational order) becomes most stable.

It is also worth noting the limitations of our choice of parameters in this study. Choosing the ranges of the patch-patch and isotropic interactions to be equal (both given by k=1.2) dictates the particular crystal structures we see. Other choices could lead to different structures. Finally, choosing the patch-patch well depth to be two times the isotropic well depth might also be too small to see an interesting fiber-bundle transition.

Table 7.1: The density range and ground state energy for different crystal structures. "n.n." means only nearest-neighbor interactions exist between particles, while "n.n.n" means next-nearest-neighbor interactions exist as well.

Crystal Structure	ρ_{min}	ρ_{max}	Theoretical U/N
fcc-o (n.n)	0.818411	1.414	-8
fcc-d (n.n)	0.818411	1.414	-6
bcc-o (n.n.n)	1.15741	1.299	-9

Table 7.2: Free energy of the solid phases, as obtained by thermodynamic integration from the Einstein crystal.

Crystal Structure	T	ρ	λ_{max}	$\beta F_{ex}/N$
fcc-d	0.9	1.09	4000	-0.013
fcc-o	0.5	1.09	1000	-5.901
fcc-o	0.25	1.33	10000	-18.228
bcc-o	0.25	1.23	20000	-21.790
fcc-o	0.1	1.38	20000	-63.425
bcc-o	0.1	1.25	20000	-75.140

Table 7.3: Coexistence points obtained using the thermodynamic integration method. The points marked with a † or a § are in the region where fcc-o and bcc-o coexistence exhibits a domelike shape, i.e. a reentrant behavior. † for the left branch, § for the right branch.

Phase 1	Phase 2	T	P	ρ_1	ρ_2
fluid	fcc-d	0.9	0.899	0.722	1.044
† bcc-o	fcc-o	0.3	2.203	1.221	1.118
† bcc-o	fcc-o	0.25	0.0122	1.217	1.068
§ bcc-o	fcc-o	0.3	14.6725	1.239	1.305
§ bcc-o	fcc-o	0.25	15.908	1.245	1.328
bcc-o	fcc-o	0.1	16.575	1.271	1.377

Table 7.4: Some of the coexistence points obtained from the Gibbs-Duhem integration. See Table 7.3 for the meanings of the symbols in front.

Phase 1	Phase 2	T	P	ρ_1	ρ_2
fluid	fcc-d	0.79048	0.168	0.392	1.046
† bcc-o	fcc-o	0.355991	5.124	1.222	1.145
† bcc-o	fcc-o	0.322056	3.256	1.221	1.130
† bcc-o	fcc-o	0.277617	1.097	1.219	1.099
§ bcc-o	fcc-o	0.354937	11.404	1.233	1.258
§ bcc-o	fcc-o	0.32129	13.905	1.236	1.297
§ bcc-o	fcc-o	0.27738	15.340	1.241	1.316
bcc-o	fcc-o	0.152605	16.734	1.258	1.362

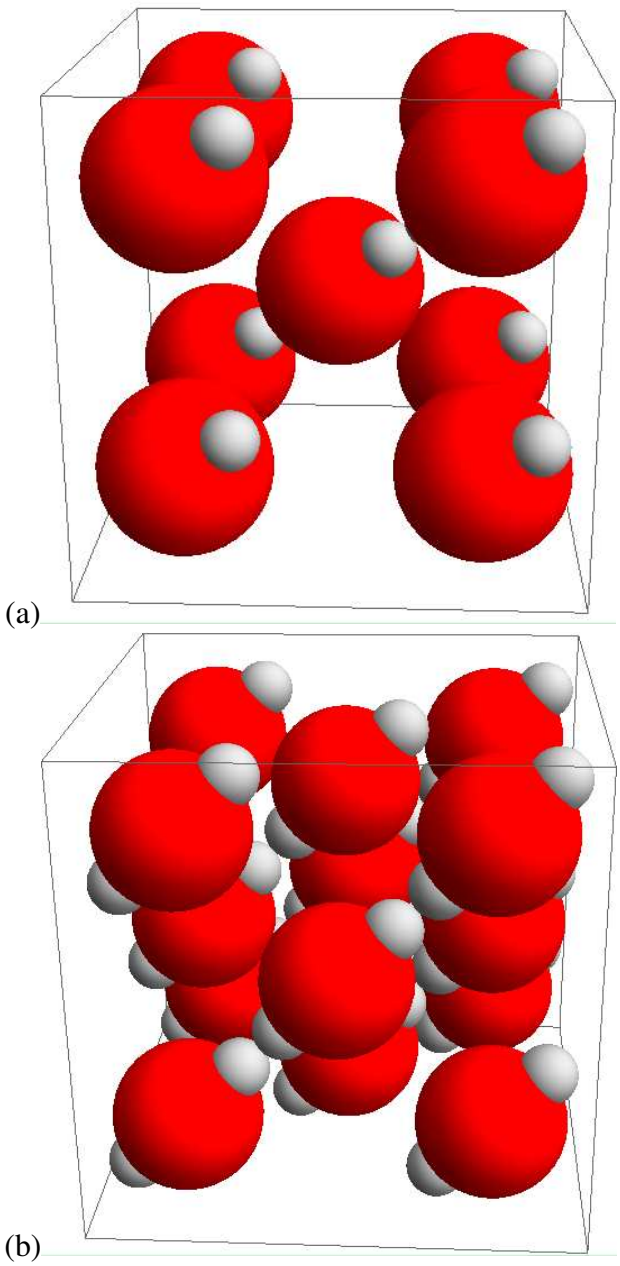


Figure 7.1: Unit cells of the (a) bcc-o and (b) fcc-o structures. In both cases the patches are aligned with the nearest neighbors.

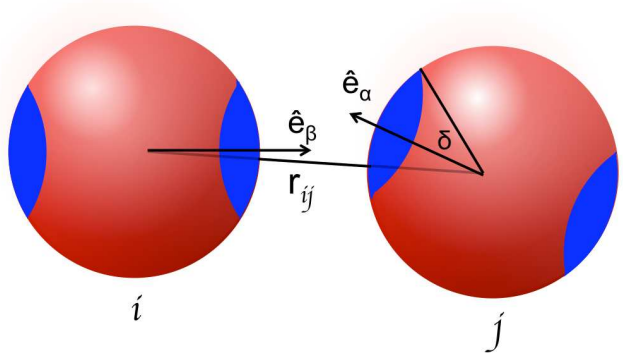


Figure 7.2: Illustration of the patch definition. A patch α is described by a solid angle (half opening angle δ about an axis $\hat{e}_\alpha$ (unit patch vector)). The two particles in the figure attract each other through both the isotropic and anisotropic square well potentials, because their separation vector r_{ij} intersects some patch (not necessarily the same one) on both particles, and the particles are within range ($r_{ij} < k\sigma$).

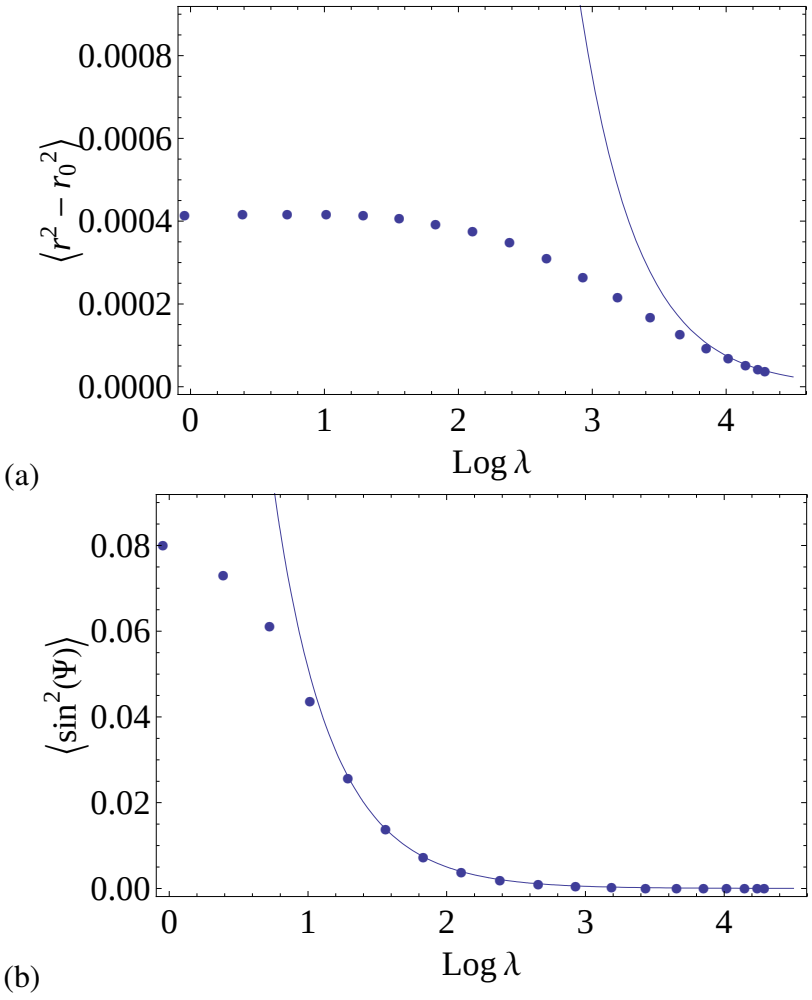
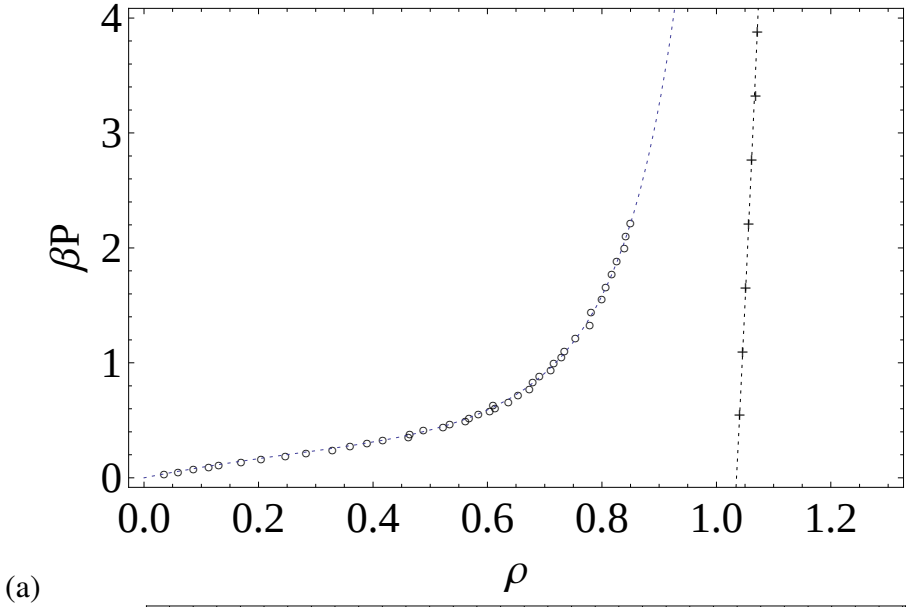
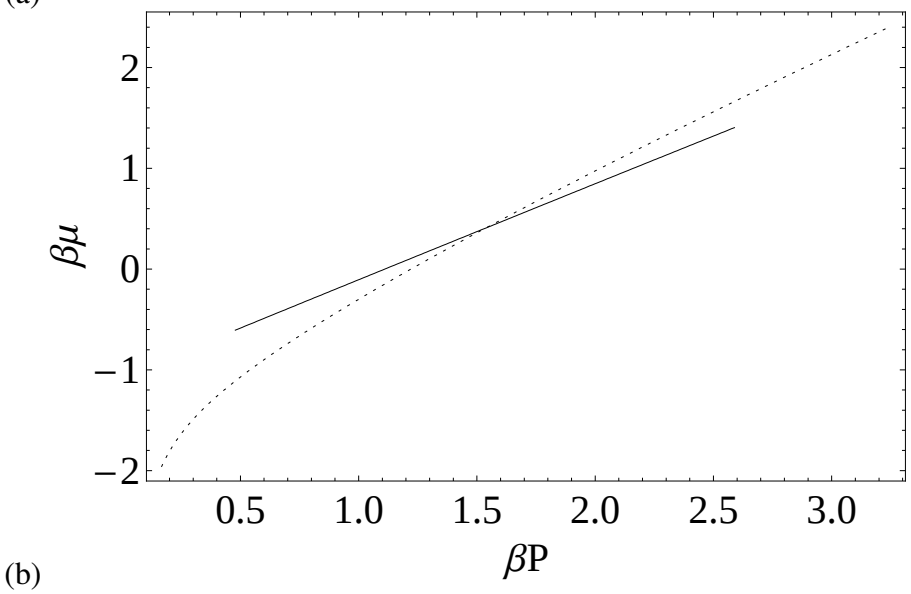


Figure 7.3: Monte Carlo data of the mean squared displacements for the coupled solid (dots) compared with that of an Einstein crystal (solid line) at $T = 0.5$. We can see that $\lambda \to \lambda_{max}$, both $< r^2 - r_0^2 >$ and $< \sin(\Psi)^2 >$ converge to the theoretical value of the Einstein lattice.



(a)



(b)

Figure 7.4: (a) Liquid and fcc-d isotherms at $T = 0.9$. '$\circ$' and '+' are the Monte Carlo simulation results for liquid and fcc-d, respectively. The dotted curves are the fits to the data. The fitting formulas of isotherms are $\beta P_{Liq} = \sum_{i=1}^{m} c_i (\frac{\rho}{1-a\rho})^i$ for liquid and $\beta P_{Sol} = \sum_{i=0}^{4} c_i \rho^i$ for fcc-d. (b) $\beta\mu - \beta P$ plot at $T = 0.9$. Dotted line for liquid; solid line for fcc-d solid.

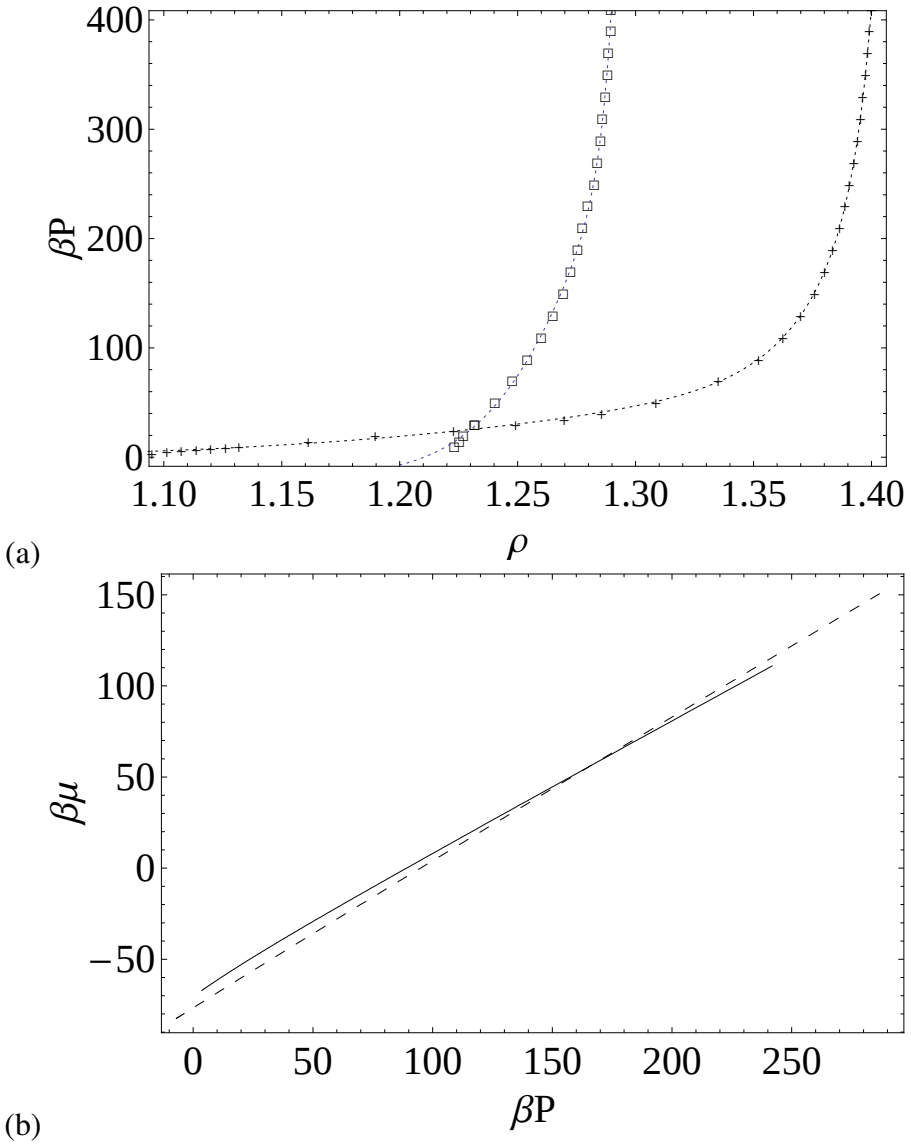
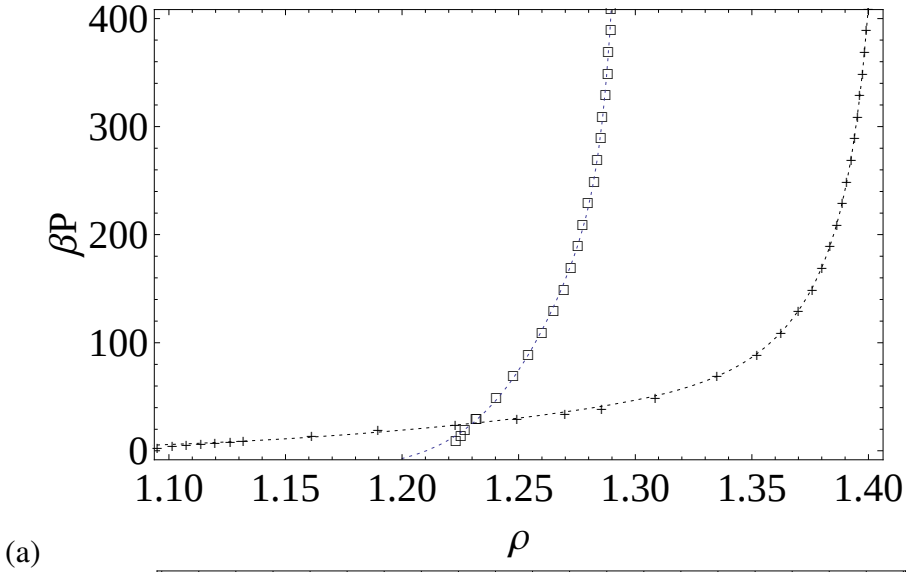
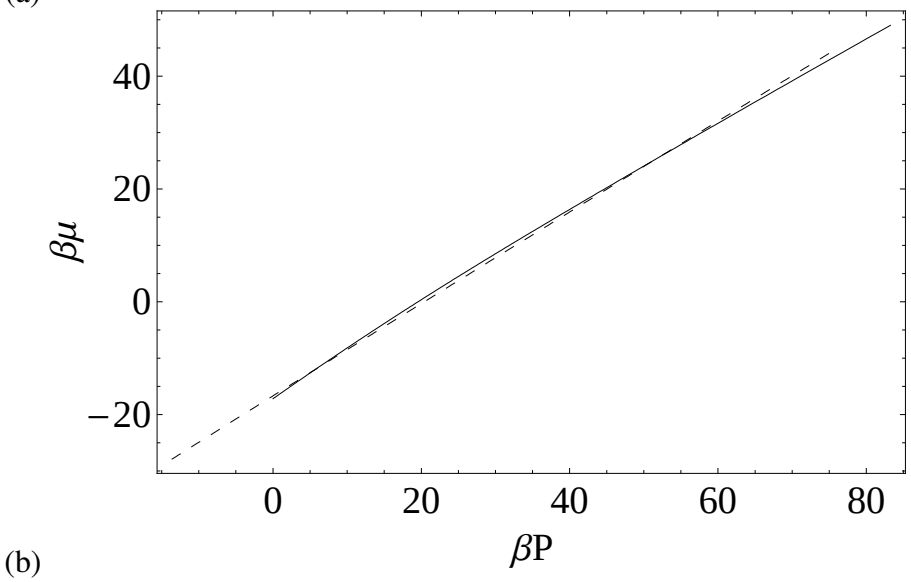


Figure 7.5: (a) bcc-o and fcc-o isotherms at $T = 0.1$. '□' and '+' are the Monte Carlo simulation results for bcc-o and fcc-o, respectively. The dotted curves are the fits to the data. The fitting formulas of isotherms are $\beta P = \sum_{i=1}^{m} c_i (\frac{\rho - d}{1 - a\rho})^i$ for both solids. (b) $\beta\mu - \beta P$ plot at $T = 0.1$. Dashed line for bcc-o; solid line for fcc-o.



(a)



(b)

Figure 7.6: (a) bcc-o and fcc-o isotherms at $T = 0.3$. '□' and '+' are the Monte Carlo simulation results for bcc-o and fcc-o, respectively. The dotted curves are the fits to the data. The fitting formulas of isotherms are $\beta P = \sum_{i=1}^{m} c_i (\frac{\rho - d}{1 - a\rho})^i$ for both solids. (b) $\beta\mu - \beta P$ plot at $T = 0.3$. Dashed line for bcc-o; solid line for fcc-o. Note that there are two pressures at which bcc-o coexists with fcc-o (reentrant behavior).

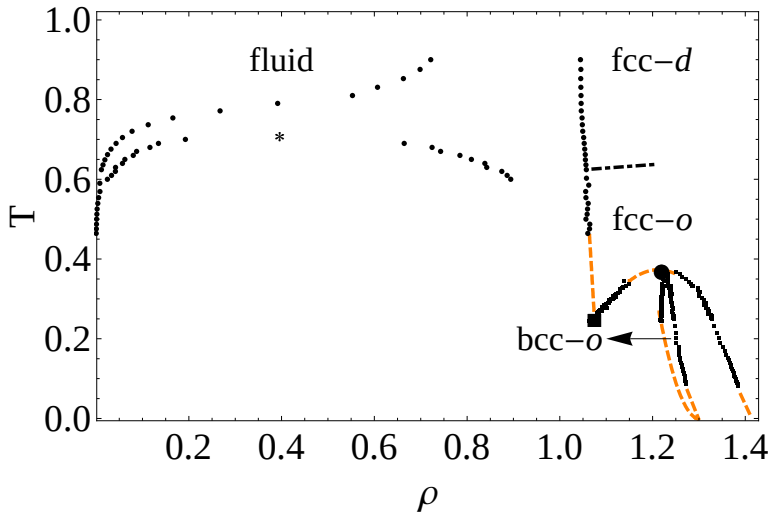


Figure 7.7: $T - \rho$ phase diagram of our model. Dots are Monte Carlo data. Asterisk-critical point, filled square-triple point, filled circle-the position where reentrant behavior occurs. The dashed lines are estimates following the trend of the MC data. The dotdashed line is an estimate of where the fcc-d-fcc-o transition occurs.

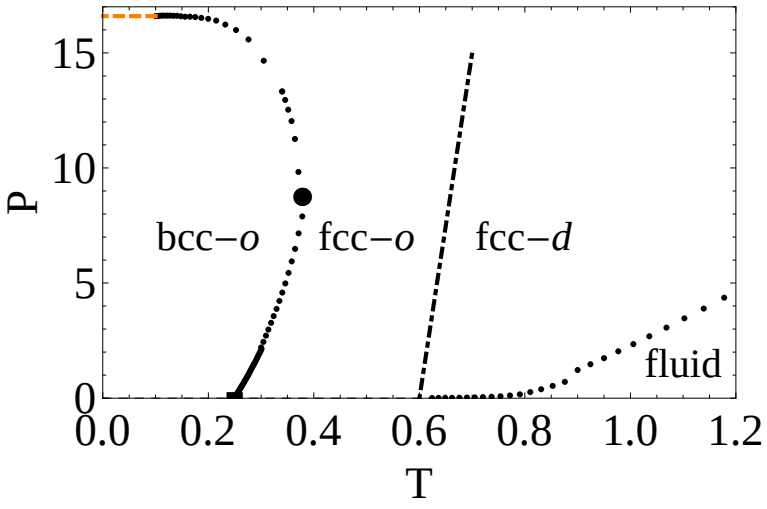


Figure 7.8: $P - T$ phase diagram of our model. Dots are Monte Carlo data. Filled square-triple point, filled circle-the position where reentrant behavior occurs. The dashed lines are estimates following the trend of the MC data. The dotdashed line is an estimate of where the fcc-d-fcc-o transition occurs.

Chapter 8

Conclusion

Protein molecules are very complex systems which interact through a variety of forces, including hydrophobic, hydrophilic, electrostatic, and other non-covalent interactions such as hydrogen bonding. The nucleation of globular proteins is a crucial, bottleneck step leading to the growth of protein crystals or to the subsequent aggregation. The physical conditions of the initial solution sensitively affects the nucleation process. These conditions include temperature, pH, salt concentration, precipitant, and so on. It has been found that a metastable fluid-fluid coexistence curve can enhance the nucleation process in a narrow region above that curve [109]. Therefore, we have determined for several interesting models the corresponding phase diagrams using Monte Carlo (MC) simulations. In particular, we focused on investigating how adding different types of salt influences the properties on phase equilibria of protein solutions in the first few chapters (3-5). We mainly studied two possible causes of this effect (Hofmeister effect):

ion-dispersion forces and hydrophobic surface forces.

In Chapter 4 we predicted the phase diagram for 0.2 M NaSCN lysozyme solution. We adopted the model proposed by Boström et al. [11]. They made an effort to explain the Hofmeister effect mainly by taking into account the ion-dispersion forces. It is clear that the model is an improvement over earlier models of lysozyme in that it can account at least qualitatively for the Hofmeister effect. As expected, our MC results are rather different and more accurate than those predicted by Boström et al. using first order perturbation theory. Our results show a larger metastability gap than obtained from the perturbation theory; the MC results yield a gap of 18%.

In Chapter 5 we have studied models of two electrolyte solutions (0.2 M NaI and 0.3 M NaCl) of lysozyme and demonstrated the effects of hydrophobic surface forces on the phase diagram of lysozyme. These models were obtained by Lund et al. [70]. Although the molarities studied are too small to see a significant metastability gap, the 0.3 M NaCl solution does have a slightly metastable fluid-fluid critical point. In contrast, the 0.2 M NaI shows a stable fluid-fluid coexistence curve, presumably due to a secondary repulsion extremum in the potential of mean force. It is not clear what the physical origin of the secondary maximum is for the model of Lund et al. [70], but Brandon et al. [14] attribute their secondary maximum to the effect of water restructuring near the solute particles. It would be interesting to have a better understanding of its origin for the current model. As we are unable to compare the results of this study with any

experimental results for lysozyme, we cannot determine the accuracy of the model.

As a side project, we also examined in Chapter 6 the ion-dispersion effects on a model of nanoparticles, proposed by Deniz et al. [25]. We have quantitatively demonstrated for the model of aluminum oxide the important effect of salt type on the phase diagrams of nanoparticles in electrolyte solutions. We employed finite-size scaling techniques as well as multicanonical simulations to determine the critical point and subcritical behavior of their model for the NaI electrolyte. We showed that the critical point of the NaI is significantly higher than that of the non-polarizable salt system, due to the ion-dispersion forces.

It would seem likely that further developments will include both the specific ion-dispersion effects and the hydrophobic surface forces to reach a more thorough understanding of the Hofmeister effect. Such developments require more accurate quantum mechanical calculations of the amplitudes of the ion-dispersion forces; these types of calculations are currently being carried out [86, 85]. Another effect that might need to be investigated is the effect of the buffer on the potential of mean force. The buffer is usually added to obtain the right pH and otherwise is assumed to have no further influence, but it is conceivable that there could be large buffer effects on the potential of mean force [106]. Further, it is possible that isotropic models such as these (i.e. models that are independent of macromolecule orientation) cannot account for such quantitative features as the breadth of the coexistence curve and that one must take into account the

effects of anisotropy [55, 104, 28] on the interactions that can arise from a variety of sources, including that of water.

Finally in Chapter 7 we have studied the role of anisotropy since anisotropy is unavoidable in real proteins. The model we have studied is one of the simplest anisotropic models and might also be of use in studying the fiber-bundle transitions inspired by the work of Huisman et al. [47]. Such types of transitions can be relevant to the cause of sickle cell disease. We have determined in this chapter the main features of the phase equilibria for this model. In spite of the relative simplicity of the model, it has a complex phase diagram. We have observed that several different crystal structures compete with one another, in addition to metastable fluid-fluid coexistence. Particularly, we have found an interesting reentrant behavior in a temperature range for the bcc-fcc coexistence. Now that we have an understanding of the equilibrium phase transitions of this model, a next step would be to see whether the model has a nonequilibrium fiber-bundle transition that is more realistic than the original work of Huisman et al[47].

Bibliography

[1] A. W. Adamson and A. P. Gast, *Physical chemistry of surfaces*, Wiley-Interscience, New York, 1997.

[2] M. P. Allen and D. J. Tildesley, *Computer simulation of liquids*, Oxford Univeristy Press, Oxford, 1987.

[3] N. Asherie, A. Lomakin, and G. B. Benedek, *Phase diagram of colloidal solutions*, Phys. Rev. Lett. **77** (1996), 4832–4835.

[4] C. H. Back, Ch. Würsch, A. Vaterlaus, U. Ramsperger, U. Maier, and D. Pescia, *Experimental confirmation of universality for a phase transition in two dimensions*, Nature **378** (1995), 597–600.

[5] J. A. Barker and D. Henderson, *Perturbation theory and equation of state for fluids. II. A successful theory of liquids*, J. Chem. Phys. **47** (1967), 4714–4721.

[6] ———, *What is "liquid"? Understanding the states of matter*, Rev. Mod. Phys. **48** (1976), 587–671.

[7] G. B. Benedek, *Cataract as a protein condensation disease. The proctor lecture*, Ivest. Ophthalmol. Vis. Sci. **38** (1997), 1911–1921.

[8] B. A. Berg and T. Neuhaus, *Multicanonical ensemble: A new approach to simulate first-order phase transitions*, Phys. Rev. Lett. **68** (1992), 9–12.

[9] M. Boström and B. Ninham, Langmuir **20** (2004), 7569.

[10] M. Boström, F. W. Tavares, D. Bratko, and B. W. Ninham, *Specific ion effects ion solutions of globular proteins: Comparison between analytical models and simulations*, J. Phys. Chem. B **109** (2005), 24489–24494.

[11] M. Boström, F. W. Tavares, B. W. Ninham, and J. M. Prausnitz, *Effect of salt identity on the phase diagram for a globular protein in aqueous electrolye solution*, J. Phys. Chem. B **110** (2006), 24757–24760.

[12] M. Boström, D. R. M. Williams, and B. W. Ninham, *Specific ion effects: Why DLVO theory fails for biology and colloid systems*, Phys. Rev. Lett. **87** (2001), 168103.

[13] ———, *Specific ion effects: why the properties of lysozyme in salt solutions follow a Hofmeister series*, Biophys. J. **85** (2003), 686–694.

[14] S. Brandon, P. Katsonis, and P. G. Vekilov, *Multiple extrema in the intermolecular potential and the phase diagram of protein solutions*, Phys. Rev. E **73** (2006), 061917.

[15] A. D. Bruce and N. B. Wilding, *Scaling fields and universality of the liquid-gas critical point*, Phys. Rev. Lett. **68** (1992), 193–196.

[16] J. Cao, D. Liao, R. Mirchev, J. J. M. de Liano, J.-P. Himanen, J. M. Manning, and F. A. Ferrone, *Nucleation and polymerization of sickle hemoglobin with leu β88 substituted by ala*, J. Mol. Biol. **265** (1997), 580–589.

[17] J. Chang, A. M. Lenhoff, and S. I. Sandier, *Determination of fluid-solid transitions in model protein solutions using the histogram reweighting method and expanded ensemble simulations*, J. Chem. Phys. **120** (2004), 3003.

[18] W. G. Chapman, G. Jackson, and K. E. Gubbins, *Phase equilibria of associating fluids: chain molecules with multiple binding sites*, Mol. Phys. **65** (1988), 1057–1079.

[19] J.-H Chen, M. E. Fisher, and B. G. Nickel, *Unbiased estimation of corrections to scaling by partial differential approximants*, Phys. Rev. Lett. **48** (1982), 630–634.

[20] R. A. Curtis, J. Ulrich, A. Montaser, J. M. Prausnitz, and H. W. Blanch, *Protein-protein interactions in concentrated electrolyte solutions: Hofmeister series effect*, Biotechnol. Bioeng. **79** (2002), 367–380.

[21] A. Daanoun, C. F. Tejero, and M. Baus, *van der Waals theory for solids*, Phys. Rev. E **50** (1994), 2913–2924.

[22] L. X. Dang, *Computational study of ion binding to the liquid interface of water*, J. Phys. Chem. B **106** (2002), 10388.

[23] ———, *Solvation of the hydronium ion at the water liquid/vapor interface*, J. Chem. Phys. **119** (2003), 6351–6353.

[24] L. X. Dang and T.-M. J. Chang, *Molecular mechanism of ion binding to the liquid/vapor interface of water*, J. Phys. Chem. B **106** (2002), 235–238.

[25] V. Deniz, M. Boström, D. Bratko, F.W. Tavares, and B.W. Ninham, *Specific ion effects: Interaction between nanoparticles in electrolyte solutions*, Colloids and Surfaces A **319** (2008), 98–102.

[26] B. V. Derjaguin and L. Landau, *Theory of the stability of strongly charged lyophobic sols and the adhesion of strongly charged particles in solutions of electrolytes*, Acta Physicochim. USSR **14** (1941), 633–662.

[27] J. P. K. Doye, A. A. Louis, I.-C. Lin, L. R. Allen, E. G. Noya, A. W. Wilber, H. C. Kok, and R. Lyus, Phys. Chem. Chem. Phys. **9** (2007), 2197.

[28] R. Fantoni, D. Gazzillo, A. Giacometti, M. A. Miller, and G. Pastore, *Patchy sticky hard spheres: Analytical study and monte carlo simulations*, J. Chem. Phys. **127** (2007), 234507.

[29] A. M. Ferrenberg and D. P. Landau, *Critical behavior of the three-dimensional Ising model: A high-resolution Monte Carlo study*, Phys. Rev. B **44** (1991), 5081–5091.

[30] A. M. Ferrenberg and R. H. Swendsen, *New Monte Carlo technique for studying phase transitions*, Phys. Rev. Lett. **61** (1988), 2635–2638.

[31] S. Finet, F. Skouri-Panet, M. Casselyn, F. Bonneté, and A. Tardieu, *The Hofmeister effect as seen by SAXS in protein solutions*, Curr. Opin. Colloid and Interface Sci. **9** (2004), 112–116.

[32] D. Frenkel and A.J.C. Ladd, *New Monte-Carlo method to compute the free energy of arbitrary solids. application to the Fcc and Hcp phases of hard-spheres*, J. Chem. Phys. **81** (1984), 3188–3193.

[33] D. Frenkel and B. Smit, *Understanding molecular simulation. From algorithms to applications. second edition*, Academic Press, Boston, 2002.

[34] H.L. Friedman, *A course in statistical mechanics*, Prentice-Hall, Engle- 377 wood Cliffs, 1985.

[35] B. C. Garrett, *Ions at the air/water interface*, Science **303** (2004), 1146 – 1147.

[36] A. George and W. Wilson, *Predicting protein crystallization from a dilute solution property*, Acta Cryst. **D50** (1994), 361–365.

[37] S. Ghosal, J. C. Hemminger, H. Bluhm, B. S. Mun, E. L. D. Hebenstreit, G. Ketteler, D. F. Ogletree, F. G. Requejo, and M. Salmeron, *Electron spectroscopy of aqueous solution interfaces reveals surface enhancement of halides*, Science **307** (2005), 563.

[38] J. W. Gibbs, *The collected works of j. willard gibbs*, Longmans, New York, 1928.

[39] S. Gopalakrishnan, P. Jungwirth, D. J. Tobias, and H. C. Allen, J. Phys. Chem. B **109** (2005), 8861.

[40] S. A. Gravina, L. B. Ho, C. B. Eckman, K. E. Long, L. Otvos Jr., L. H. Younkin, N. Suzuki, and S. G. Younkin, *Amyloid β-protein Aβ in Alzheimer's disease brain*, J. Biol. Chem. **270** (1995), 7013–7016.

[41] J. D. Gunton, A. Shiryayev, and D. L. Pagan, *Protein condensation: Kinetic pathways to crystallization and disease*, Cambridge University Press, 2007.

[42] M. F. Hagan and D. Chandler, Biophys. J. **91** (2006), 42.

[43] L. D. Hart and E. Lense, *Alumina chemicals*, Wiley-American Ceramic Society, 1990.

[44] D. Henderson and J. A. Barker, *Perturbation theory of fluids at high temperatures*, Phys. Rev. A **1** (1970), 1266–1267.

[45] F. Hofmeister, *Zur lehre von der wirkung der salze. Zweite mittheilung.*, Arch. Exp. Pathol. Pharmakol. **24** (1888), 247–260.

[46] D. Horinek and R. R. Netz, *Specific ion adsorption at hydrophobic solid surfaces*, Phys. Rev. Lett. **99** (2007), 226104–1.

[47] B. A. H. Huisman, P. G. Bolhuis, and A. Fasolino, *Phase transition to bundles of flexible supramolecular polymers*, Phys. Rev. Lett. **100** (2008), 188301.

[48] A.-P. Hynninen, J. H. J. Thijssen, E. C. M. Vermolen, M. Dijkstra, and A. van Blaaderen, Nat. Mater. **6** (2007), 202.

[49] G. Jackson, W. G. Chapman, and K. E. Gubbins, *Phase equilibria of associating fluids. Spherical molecules with multiple bonding sites*, Mol. Phys. **65** (1988), 1–31.

[50] S. B. Johnson, G. V. Franks, P. J. Scales, and T. W. Healy, *The binding of monovalent electrolyte ions on r-alumina. II. the shear yield stress of concentrated suspensions*, Langmuir **15** (1999), 2844–2853.

[51] C. W. Jones, J. C. Wang, F. A. Ferrone, R. W. Briehl, and M. S. Turner, *Interactions between sickle hemoglobin fibers*, Faraday Discuss. **123** (2003), 221–236.

[52] P. Jungwirth and D. J.Tobias, *Molecular structure of salt solutions: a new view of the interface with implications for heterogeneous atmospheric chemistry*, J. Phys. Chem. B **105** (2001), 10468–10472.

[53] P. Jungwirth and D. J. Tobias, *Surface effects on aqueous ionic solvation: A molecular dynamics simulation study of nacl at the air/water interface from infinite dilution to saturation*, J. Phys. Chem. B **104** (2000), 7702–7706.

[54] _____, J. Phys. Chem. B **105** (2001), 10648.

[55] N. Kern and D. Frenkel, *Fluid-fluid coexistence in colloidal systems with short-ranged strongly directional attraction*, J. Chem. Phys. **118** (2003), 9882–9889.

[56] T. Kim, K. Lee, M. Gong, and S. Joo, *Control of gold nanoparticle aggregates by manipulation of interparticle interaction*, Langmuir **21** (2005), 9524–9528.

[57] E. M. Knipping, M. J. Lakin, K. L. Foster, P. Jungwirth, D. J. Tobias, R. B. Gerber, D. Dabdub, and B. J. Finlayson-Pitts, *Experiments and simulations of ion-enhanced interfacial chemistry on aqueous NaCl aerosols*, Science **288** (2000), 301–306.

[58] D. A. Kofke, *Direct evaluation of phase coexistence by molecular simulation via integration along the saturation line*, J. Chem. Phys. **98** (1993), 4149–4162.

[59] ———, *Gibbs-Duhem integration: a new method for direct evaluation of phase coexistence by molecular simulation*, Mol. Phys. **78** (1993), 1331–1336.

[60] W. Kunz, P. Lo Nostro, and B. W. Ninham, *The present state of affairs with Hofmeister effects*, Curr. Opin. Colloid Interface Sci. **9** (2004), 1–18.

[61] Y.-M. Kuo, M. R. Emmerling, C. Vigo-Pelfrey, T. C. Kasunic, J. B. Kirkpatrick, G. H. Murdoch, M. J. Ball, and A. E. Roher, *Water-soluble Aβ (N-40, N-42) oligomers in normal and Alzheimer disease brains*, J. Biol. Chem. **271** (1996), 4077–4081.

[62] S. Lafont, S. Veesler, J. P. Astier, and R. Boistelle, *Comparison of solubilities and molecular interactions of BPTI molecules giving different polymorphs*, J. Cryst. Growth **173** (1997), 132–140.

[63] S. Lettieri, X. Li, and J. D. Gunton, *Hofmeister effect and the phase diagram of lysozyme*, Phys. Rev. E **78** (2008), 011921–1.

[64] ———, *Ion specific effects on phase transitions in protein solutions*, Phys. Rev. E **79** (2009), 031904.

[65] X. Li, S. Lettieri, N. Wentzel, and J. D. Gunton, *Phase diagram of a model of nanoparticles in electrolyte solutions*, J. Chem. Phys. **129** (2008), 164113.

[66] E. R. A. Lima, D. Horinek, R. R. Netz, Jr. E. C. Biscaia, F. W. Tavares, W. Kunz, and M. Boström, *Specific ion adsorption and surface forces in colloid science*, J. Phys. Chem. B **112** (2008), 1580–1585.

[67] E. R. A. Lima, E. C. Biscaia Jr., M. Boström, F. W. Tavares, and J. M. Prausnitz, *Osmotic second virial coefficients and phase diagrams for aqueous proteins from a much-improved Poisson-Boltzmann equation*, J. Phys. Chem. C **111** (2007), 16055.

[68] D. Liu, G. Ma, L. Levering, and H. C. Allen, J. Phys. Chem. B **108** (2004), 2252.

[69] M. Lund and P. Jungwirth, *Patchy proteins, anions and the hofmeister series*, J. Phys.: Condens. Matter **20** (2008), 494218.

[70] M. Lund, P. Jungwirth, and C. E. Woodward, *Ion specific protein assembly and hydrophobic surface forces*, Phys. Rev. Lett. **100** (2008), 258105–1–258105–4.

[71] M. Lund, R. Vácha, and P. Jungwirth, *Specific ion binding to macromolecules: effects of hydrophobicity*, Langmuir **24** (2008), 3387–3391.

[72] M. Lund, L. Vrbka, and P. Jungwirth, *Specific ion binding to nonpolar surface patches of proteins*, J. Am. Chem. Soc. **130** (2008), 11582–11583.

[73] J. F. Lutsko and G. Nicolis, *Theoretical evidence for a dense fluid precursor to crystallization*, Phys. Rev. Lett. **96** (2006), 046102.

[74] M. Manciu and E. Ruckenstein, AdV. Colloid Interface Sci. **105** (2003), 63.

[75] V. S. Markin and A. G. Volkov, J. Phys. Chem. B **106** (2002), 11810.

[76] Y. Min, M. Akbulut, K. Kristiansen, Y. Golan, and J. Israelachvili, *The role of interparticle and external forces in nanoparticle assembly*, Nature Materials **7** (2008), 527 – 538.

[77] U. Närger and D. A. Balzarini, *Coexistence-curve diameter and critical density of xenon*, Phys. Rev. B **42** (1990), 6651–6657.

[78] B. G. Nickel and J. J. Rehr, *High-temperature series for scalar-field lattice models: Generation and analysis*, J. Stat. Phys. **61** (1990), 1–50.

[79] J. F. Nicoll, *Critical phenomena of fluids: Asymmetric Landau-Ginzburg-Wilson model*, Phys. Rev. A **24** (1981), 2203–2220.

[80] B. W. Ninham and V. Yaminsky, *Ion binding and ion specificity: the Hofmeister effect and Onsager and Lifshitz theories*, Langmuir **13** (1997), 2097–2108.

[81] M. G. Noro and D. Frenkel, *Extended corresponding-states behavior for particles with variable range attractions*, J. Chem. Phys. **113** (2000), 2941–2944.

[82] E.G. Noya and C. Vega, *Phase diagram of model anisotropic particles with octahedral symmetry*, J. Chem. Phys. **127** (2007), 054501.

[83] D. L. Pagan and J. D. Gunton, *Phase behavior of short-range square-well model*, J. Chem. Phys. **122** (2005), 184515.

[84] A. Z. Panagiotopoulos, *Direct determination of phase coexistence properties of fluids by Monte Carlo simulation in a new ensemble*, Mol. Phys. **61** (1987), 813–826.

[85] D. F. Parsons, V. Deniz, and B. W. Ninham, *Nonelectrostatic interactions between ions with anisotropic ab initio dynamic polarisabilities*, preprint (2008).

[86] D. F. Parsons and B. W. Ninham, *The importance of accurate dynamic polarisabilities in specific ion effects*, preprint (2008).

[87] M. W. Pestak and M. H. W. Chan, *Equation of state of N_2 and Ne near their critical points. scaling, corrections to scaling, and amplitude ratios*, Phys. Rev. B **30** (1984), 274–288.

[88] P. B. Petersen and R. J. Saykally, Chem. Phys. Lett. **397** (2004), 51.

[89] ———, J. Phys. Chem. B **109** (2005), 7976.

[90] R. Piazza, Curr. Opin. Colloid Interface Sci. **8** (2004), 515–522.

[91] R. Piazza and M. Pierno, *Protein interactions near crystallization: a microscopic approach to the hofmeister series*, J. Phys.: Condens. Matter **12** (2000), A443–A449.

[92] E. A. Raymond and G. L. Richmond, J. Phys. Chem. B **108** (2004), 5051.

[93] J. J. Rehr and N. D. Mermin, *Revised scaling equation of state at the liquid-vapor critical point*, Phys. Rev. A **3** (1973), 472–480.

[94] D. W. Richerson, *The magic of ceramics*, Wiley-American Ceramic Society, 2000.

[95] D. Rosenbaum, P. C. Zamora, and C. F. Zukoski, *Phase behavior of small attractive colloidal particles*, Phys. Rev. Lett. **76** (1996), 150–153.

[96] D. F. Rosenbaum and C. F. Zukoski, *Protein interactions and crystallization*, J. Cryst. Growth **169** (1996), 752–758.

[97] E. Sanz, C. Vega, J. L. F. Abascal, and L.G. MacDowell, *Phase diagram of water from computer simulation*, Phys. Rev. Lett. **92** (2004), 255701.

[98] J. W. Schroer and P. A. Monson, *Phase behavior of a hard sphere interaction site model of benzene*, J. Chem. Phys. **112** (2000), 8950.

[99] F. Sciortino, E. Bianchi, J. F. Douglas, and P. Tartaglia, *Self-assembly of patchy particles into polymer chains: a parameter-free comparison between Wertheim theory and Monte Carlo simulation*, J. Chem. Phys. **126** (2007), 194903.

[100] R. P. Sear, *Phase behavior of a simple model of globular proteins*, J. Chem. Phys. **111** (1999), 4800–4806.

[101] J. V. Sengers and J. M. H. Levelt Sengers, *Thermodynamic behavior of fluids near the critical point*, Annu. Rev. Phys. Chem. **37** (1986), 189–222.

[102] A. Shiryayev and J. D. Gunton, *Crystal nucleation for a model of globular proteins*, J. Chem. Phys. **120** (2004), 8318–8326.

[103] A. Shiryayev, X. Li, and J. D. Gunton, *Model of sickle hemogloblin*, J. Chem. Phys. **125** (2006), 024902.

[104] X. Song, *Role of anisotropic interactions in protein crystallization*, Phys. Rev. E. **66** (2002), 011909.

[105] A. Stradner, G. Foffi, N. Dorsaz, G. Thurston, and P. Schurtenberger, *New insight into cataract formation: enhanced stability through mutual attraction*, Phys. Rev. Lett. **99** (2007), 198103–1.

[106] A. Striolo, F. W. Tavares, D. Bratko, H. W. Blanch, and J. M. Prausnitz, *Analytic calculation of phase diagrams for charged dipolar colloids with orientation-averaged pair potentials*, Phys. Chem. Chem. Phys. **5** (2003), 4851.

[107] V. Talanquer and D. W. Oxtoby, *Crystal nucleation in the presence of a metastable critical point*, J. Chem. Phys. **109** (1998), 223–227.

[108] F. W. Tavares, D. Bratko, H. W. Blanch, and J. M. Prausnitz, *Ion-specific effects in the colloid-colloid or protein-protein potential of mean force: role of salt-macroion van der Waals interactions*, J. Phys. Chem. B **108** (2004), 9228–9235.

[109] P. R. ten Wolde and D. Frenkel, *Enhancement of protein crystal nucleation by critical density fluctuations*, Science **277** (1997), 1975–1978.

[110] M. M. Tsypin and H. W. J. Blöte, *Probability distribution of the order parameter for the three-dimensional Ising-model universality class: A high-precision Monte Carlo study*, Phys. Rev. Lett. **62** (2000), 73–76.

[111] M. S. Turner, R. W. Briehl, F. A. Ferrone, and R. Josephs, *Twisted protein aggregates and disease: the stability of sickle hemoglobin fibers*, Phys. Rev. Lett. **90** (2003), 128103.

[112] C. Vega and P. A. Monson, *Solid-fluid equilibrium for a model with short ranged directional forces*, J. Chem. Phys. **109** (1998), 9938–9949.

[113] C. Vega and P.A. Monson, J. Chem. Phys. **102** (1995), 1361.

[114] P. G. Vekilov and A. A. Chernov, *The physics of protein crystallization*, Solid State Physics **57** (2002), 1–147.

[115] E. J. W. Verwey and J. Th. G. Overbeek, *Theory of stability of lyophobic colloids*, Elsevier, Amsterdam, 1948.

[116] M. S. Wertheim, *Fluids with highly directional attractive forces. I. Statistical thermodynamics*, J. Stat. Phys. **35** (1984), 19–34.

[117] ———, *Fluids with highly directional attractive forces. II. Thermodynamic perturbation theory and integral equations*, J. Stat. Phys. **35** (1984), 35–47.

[118] ———, *Fluids with highly directional attractive forces. III. Multiple attraction sites*, J. Stat. Phys. **42** (1986), 459–476.

[119] ———, *Fluids with highly directional attractive forces. IV. Equilibrium polymerization*, J. Stat. Phys. **42** (1986), 477–492.

[120] The width can be defined as the difference between the distances at which the potential equals half the attraction depth.

[121] A. W. Wilber, J. P. K. Doye, A. A. Louis, E. G. Noya, M. A. Miller, and P. Wong, J. Chem. Phys. **127** (2007), 085106.

[122] N. B. Wilding, *Critical-point and coexistence-curve properties of the Lennard-Jones fluid: a finite-size scaling study*, Phys. Rev. E **52** (1995), 602–611.

[123] M. Wilson and A. Pohorille, *Interaction of monovalent ions with the liquid-vapor interface of water: a molecular dynamics study*, J. Chem. Phys. **95** (1991), 6005–6013.

[124] M. A. Wilson, A. Pohorille, and L. R. Pratt, *Interaction of a sodium ion with the water liquid-vapor interface*, Chem. Phys. **129** (1989), 209–212.

[125] K. Van Workum and J. F. Douglas, Phys. Rev. E. **73** (2006), 031502.

[126] Q. Zhang and J. P. Badiali, *Calculation of the critical exponents by a renormalization of the Ornstein-Zernike equation*, Phys. Rev. Lett. **67** (1991), 1598–1601.

[127] ———, *Critical phenomena in liquid phases: Renormalization from the Ornstein-Zernike equation*, Phys. Rev. A **45** (1992), 8666–8682.

[128] Y. Zhang and P.S. Cremer, *Interactions between macromolecules and ions: The Hofmeister series.*, Curr. Opin. Chem. Biol **10** (2006), 658–663.

[129] Z. Zhang and S. C. Glotzer, *Self-assembly of patchy particles*, Nano Letters **4** (2004), 1407–1413.

[130] Z. Zhang, A. S. Keys, T. Chen, and S. C. Glotzer, Langmuir **21** (2005), 11547.

Vita

Xiaofei Li was born in August 21st, 1983. She earned her Bachelor of Science degree from Fudan University, China, in July 2004. She entered graduate school in August in the Department of Physics at Lehigh University in August 2004.